Models and Materials for Studying Synthetic Bone Grafts and the Biomechanics of Fracture Repair

By

Gregory Brian Lowen

Dissertation

Submitted to the Faculty of the

Graduate School of Vanderbilt University

in partial fulfillment of the requirements

for the degree of

DOCTOR OF PHILOSOPHY

in

Chemical and Biomolecular Engineering

May 13, 2022

Nashville, Tennessee

Approved:

Dr. Scott A. Guelcher, Ph.D.

Dr. Ethan S. Lippmann, Ph.D.

Dr. Jeffry S. Nyman, Ph.D.

Dr. Marjan Rafat, Ph.D.

ACKNOWLEDGMENTS

TABLE OF CONTENTS

LIST OF TABLES

The percent of distal bone nodes, surrounding the SS IMNs, exposed to equivalent stresses greater than the defined safety threshold of bone (65 MPa), generally decreased with increasing nail-bone clearances investigated. More distal bone nodes were exposed to high levels of equivalent stress in the 7 mm interlocking screw spacing simulations than in the 3.5 mm interlocking screw spacing simulations………40

stresses in the nHA-PEUR-CG composite than in the Norian CPC (median ± interquartile range) (c) A heat map of equivalent stress within the Norian CPC, under 2000 N load, revealed higher stresses concentrated below the loaded condyles. (d) The simulations predicted that the equivalent stress in the host bone will be minimally impacted by the cement chosen to fill the defect (median ± interquartile range)………………..98

7.5. 31P-NMR was used to quantify the average chain lengths of the fractionated Na-polyP samples. (a) The external phosphate (integral of peaks below left bracket) to internal phosphate (integral of peak below right bracket) ratio increased with increasing acetone addition (A to G). (b) These spectra were analyzed to reveal that Na-polyP samples with average chain lengths ranging from 10.1 to 146.4 residues can be fabricated in a furnace and isolated by acetone fractionation…………………………………………………99

7.6. wt% nHA in the bone-like scaffolds affected hBM-MSC osteogenesis while compressive strain impacted osteogenesis and chondrogenesis. (a) Alizarin Red S staining was significantly higher in the 21% nHA group than in the 0% nHA group, and compressive loading non-significantly increased staining (mean ± standard deviation). (b) The wt% nHA did not affect Alcian Blue staining, and compressive loading non-significantly increased staining (mean ± standard deviation). (c) A representative heat map of the equivalent strains along the scaffold surface shows pockets of high and low strains throughout the scaffolds (10% global strain). (d) The equivalent strain along the surface of the scaffold is less than the global strain applied to scaffold (median ± interquartile range)… …………………………………………………………………..102

NOMENCLATURE

BV/TV	bone volume fraction	PEUR	poly(ester urethane)
CG	ceramic granules (85% β-TCP/15% nHA)	polyP	polyphosphate
CPC	calcium phosphate cement	PTKUR	poly(thioketal urethane)
ECM	extracellular matrix	SEM	scanning electron microscopy
E_s	Young's modulus	SS	stainless steel
ε_{vm}	equivalent strain/von Mises strain	$\tilde{s}$	median displacement
FE/FEA	finite element/finite element analysis	Tb.Th	trabecular thickness
FeAA	iron acetylacetonate	Tb.Sp	trabecular spacing
FH-TEBC	femoral head-tissue engineered bone construct	TK	thioketal
FTIR	Fourier-transform infrared spectroscopy	β-TCP	β-tricalcium phosphate
HA/nHA	hydroxyapatite/nanocrystalline hydroxyapatite	μ	coefficient of friction
hBM-MSCs	human bone marrow mesenchymal stem cells	μCT	micro-computed tomography
ICBG	iliac crest bone graft	ν	Poisson's ratio
IFM/IFS	interfragmentary movement/strain	WSS	wall shear stress
IM/IMN	intramedullary/intramedullary nail	XRD	x-ray diffraction
LDI/LTI	lysine diisocyanate/triisocyanate		
NMR	nuclear magnetic resonance		
OSS/γ_{oct}	octahedral shear strain		
PBMC	peripheral blood mononuclear cell		
PEEK	polyether ether ketone		

CHAPTER 1 - INTRODUCTION

More than 50% of adults in the United States are afflicted with musculoskeletal disease or injury, and bone fractures are the most common musculoskeletal condition requiring medical resources [1]. While fractures are often caused by high-energy trauma, including motor vehicle accidents and falls from heights, age and disease can reduce bone strength and increase the likelihood of fragility fractures [2–5]. Of these fractures, more than 7 million required fixation, and this number is expected to increase as the country's population ages. While fracture repair is often uneventful, fracture nonunion remains a significant clinical and socioeconomic burden, and patients with impaired fracture healing require additional revision surgeries, leading to longer hospitalization stays, rehabilitation periods, increased medical expenses, and, importantly, decreased quality of life [6–8].

Nonunion, defined as the cessation of fracture repair, often occurs as a result of biological or mechanical failure, and many factors, including high body mass index, older age, concomitant disease, and smoking status can increase the risk of nonunion by altering a patient's biological potential for regenerating tissue [9–11]. Bone grafting can be implemented to promote fracture repair in patients with poor biological healing potential [12–14], but autologous bone graft (autograft), the current gold standard, is limited by the amount available and donor site morbidity [15]. Synthetic bone grafts are not hindered by the lack of biological supply, but many proposed materials do not exhibit the osteoinductivity, osteoconductivity, or mechanical properties required to support fracture repair [16,17]. Similar to biological failure, improper mechanical stability, at any stage of the bone healing process, has the potential to delay fracture repair or lead to nonunion [18–20]. Movement across a fracture is controlled clinically by the fixation strategy chosen [21–23] and the weight-bearing [24,25] or dynamization [26,27] protocols prescribed , but, while some interfragmentary movement is believed to be beneficial [28–30], the ideal amount, mode (compression, tension or shear), and timing (early or late) of this motion is currently unknown [31]. Therefore, the primary goal of this work is to develop models and materials for studying novel bone grafts and the biomechanics of fracture repair, so that therapeutic strategies can be developed to reduce the incidence of nonunion.

Chapter 1

Specific Aims

This goal was achieved through the following aims:

Aim I: Determine the relative effects of intramedullary nailing patterns on interfragmentary strain, in a mouse femur fracture, using finite element analysis.

Aim II: Investigate the prospect of using synthetic calcium polyphosphate nanoparticles as an alternative to iliac crest bone graft for posterior lumbar fusion procedures in mice.

Aim III: Develop a humanized perfusion bioreactor model of tumor-induced bone disease. While this research is not directly related to the primary goal of this thesis, lessons from this work can be applied towards future mechanotransduction studies.

Approach

Chapter 1 of this work provides a brief introduction and outlines the justification behind this dissertation. **Chapter 2** provides background knowledge on bone, fractures, and the mechanobiology of fracture repair. This chapter also summarizes current therapeutic strategies and a discusses their limitations.

Chapter 3 discusses the development of a novel finite element model for studying the impact of different intramedullary nail design parameters on the mechanical environment of a mid-diaphyseal osteotomy in a mouse femur. The model geometry was created from a micro-computed tomography scan of a mouse femur, and the dimensions of a commercially available intramedullary nail were used as a guide for designing the digital nail. The model was used to study how nail material, distance between interlocking screws, and clearance between the nail and endosteal surface affect interfragmentary strain. This chapter has recently been accepted in the Journal of Biomechanical Engineering [32].

Chapter 4 presents a study on the osteochondral effects induced by calcium polyphosphate nanoparticles. Calcium phosphate nanoparticles were synthesized by cation exchange, and a detailed characterization of the nanoparticles is presented. The biological response to the nanoparticles was

evaluated using a posterior lumbar fusion model in mice, and fusion, bone volume, and bone quality were quantified by micro-computed tomography. This research is being finalized for publication.

Chapter 5 introduces a novel humanized model of tumor-induced bone disease, in which bone cells and metastatic cancer cells were co-cultured atop resorbable scaffolds within a perfusion bioreactor. Cell seeding and ingrowth were visualized by SEM, confocal microscopy, and micro-computed tomography, and scaffold resorption was quantified gravimetrically. This work has recently been accepted by Current Protocols [33].

Finally, **Chapter 6** summarizes the main findings in this dissertation, and **Chapter 7** provides suggestions for future studies based on the work contained herein. As a whole, this dissertation presents advancements in the development of models and materials for studying novel bone graft materials and the biomechanics of fracture repair.

References:

1.	Watkins-Castillo, S. & Andersson, G. *United States Bone and Joint Initiative: The Burden of Musculoskeletal Diseases in the United States (BMUS). The Burden of Musculoskeletal diseases int he United States* (2014).
2.	Briot, K., Geusens, P., Em Bultink, I., Lems, W. F. & Roux, C. Inflammatory diseases and bone fragility. *Osteoporos. Int.* **28**, 3301–3314 (2017).
3.	Casimiro, S., Guise, T. A. & Chirgwin, J. The critical role of the bone microenvironment in cancer metastases. *Mol. Cell. Endocrinol.* **310**, 71–81 (2009).
4.	Diab, T., Condon, K. W., Burr, D. B. & Vashishth, D. Age-related change in the damage morphology of human cortical bone and its role in bone fragility. *Bone* **38**, 427–431 (2006).
5.	McCormick, R. K. Osteoporosis: Integrating biomarkers and other diagnostic correlates into the management of bone fragility. *Altern. Med. Rev.* **12**, 113–145 (2007).
6.	Hak, D. J. *et al.* Delayed union and nonunions: Epidemiology, clinical issues, and financial aspects. *Injury* **45**, S3–S7 (2014).
7.	Mills, L. A., Aitken, S. A. & Simpson, A. H. R. W. The risk of non-union per fracture: current myths and revised figures from a population of over 4 million adults. *Acta Orthopaedica* **88**, 434–439 (2017).
8.	Zura, R. *et al.* Epidemiology of fracture nonunion in 18 human bones. *JAMA Surg.* **151**, 1–12 (2016).
9.	Claes, L., Recknagel, S. & Ignatius, A. Fracture healing under healthy and inflammatory conditions. *Nat. Rev. Rheumatol.* **8**, 133–143 (2012).
10.	Gaston, M. S. & Simpson, A. H. R. W. Inhibition of fracture healing. *J. Bone Jt. Surg. - Ser. B* **89**, 1553–1560 (2007).
11.	Haffner-Luntzer, M., Liedert, A. & Ignatius, A. Mechanobiology of bone remodeling and fracture healing in the aged organism. *Innov. Surg. Sci.* **1**, 57–63 (2016).

12.   Kostenuik, P. & Mirza, F. M. Fracture healing physiology and the quest for therapies for delayed healing and nonunion. *J. Orthop. Res.* **35**, 213–223 (2017).

13.   Thompson, E. M., Matsiko, A., Kelly, D. J., Gleeson, J. P. & O'Brien, F. J. An Endochondral Ossification-Based Approach to Bone Repair: Chondrogenically Primed Mesenchymal Stem Cell-Laden Scaffolds Support Greater Repair of Critical-Sized Cranial Defects Than Osteogenically Stimulated Constructs In Vivo. *Tissue Eng. Part A* **22**, 556–567 (2016).

14.   Wang, W. & Yeung, K. W. K. Bone grafts and biomaterials substitutes for bone defect repair: A review. *Bioact. Mater.* **2**, 224–247 (2017).

15.   Mcgough, M. A. P. *et al.* Poly(Thioketal Urethane) Autograft Extenders in an Intertransverse Process Model of Bone Formation. *Tissue Eng. - Part A* **25**, 949–963 (2019).

16.   Bohner, M. Design of ceramic-based cements and putties for bone graft substitution. *Eur. Cells Mater.* **20**, 1–12 (2010).

17.   Bohner, M. Resorbable biomaterials as bone graft substitutes. *Mater. Today* **13**, 24–30 (2010).

18.   Bhandari, M. *et al.* Predictors of reoperation following operative management of fractures of the tibial shaft. *J. Orthop. Trauma* **17**, 353–361 (2003).

19.   Elliott, D. S. *et al.* A unified theory of bone healing and nonunion. *Bone Jt. J.* **98B**, 884–891 (2016).

20.   Perren, S. M., Fernandez, A. & Regazzoni, P. Understanding fracture healing biomechanics based on the "strain" concept and its clinical applications. *Acta Chir. Orthop. Traumatol. Cech.* (2015).

21.   Beltran, M. J., Collinge, C. A. & Gardner, M. J. Stress Modulation of Fracture Fixation Implants. *J. Am. Acad. Orthop. Surg.* **24**, 711–719 (2016).

22.   Betts, D. C. & Müller, R. Mechanical regulation of bone regeneration: Theories, models, and experiments. *Front. Endocrinol. (Lausanne).* **5**, 1–14 (2014).

23.   Rüedi, T. P. & Murphy, W. M. AO Principles of Fracture Management. in *AO Principles of Fracture Management* (eds. Colton, C. L., Dell'Oca, A. F., Holz, U., Kellam, J. F. & Ochsner, P. E.) 864 (AO Publishing, 2000). doi:10.1055/b-0038-160811

24.   Dehghan, N. *et al.* Early weightbearing and range of motion versus non-weightbearing and immobilization after open reduction and internal fixation of unstable ankle fractures: A randomized controlled trial. *J. Orthop. Trauma* **30**, 345–352 (2016).

25.   Houben, I. B., Raaben, M., Van Basten Batenburg, M. & Blokhuis, T. J. Delay in weight bearing in surgically treated tibial shaft fractures is associated with impaired healing: a cohort analysis of 166 tibial fractures. *Eur. J. Orthop. Surg. Traumatol.* **28**, 1429–1436 (2018).

26.   Papakostidis, C., Psyllakis, I., Vardakas, D., Grestas, A. & Giannoudis, P. V. Femoral-shaft fractures and nonunions treated with intramedullary nails: The role of dynamisation. *Injury* **42**, 1353–1361 (2011).

27.   Vaughn, J. *et al.* Nail Dynamization for Delayed Union and Nonunion in Femur and Tibia Fractures. *Orthopedics* **39**, e1117–e1123 (2016).

28.   Epari, D. R., Wehner, T., Ignatius, A., Schuetz, M. A. & Claes, L. E. A case for optimising fracture healing through inverse dynamization. *Med. Hypotheses* **81**, 225–227 (2013).

29.   Ferreira, N., Marais, L. C. & Aldous, C. Mechanobiology in the management of mobile atrophic and oligotrophic tibial nonunions. *J. Orthop.* **12**, S182–S187 (2015).

30.   Glatt, V., Evans, C. H. & Tetsworth, K. A concert between biology and biomechanics: The influence of the mechanical environment on bone healing. *Front. Physiol.* **7**, 1–18 (2017).

31.   Baker, C. E. *et al.* Bone Fracture Acute Phase Response—A Unifying Theory of Fracture Repair: Clinical and Scientific Implications. *Clin. Rev. Bone Miner. Metab.* **16**, 142–158 (2018).

32.   Lowen, G. *et al.* Effect of Intramedullary Nailing Patterns On Interfragmentary Strain in a Mouse Femur Fracture: a Parametric Finite Element Analysis. *J. Biomech. Eng.* (2021). doi:10.1115/1.4053085

33.   Lowen, G. B. *et al.* A Perfusion Bioreactor Model of Tumor-Induced Bone Disease Using Human Cells. *Curr. Protoc.* **2**, 1–21 (2022).

CHAPTER 2 - BACKGROUND

2.1   The mechanical properties and biology of bone

Bone, composed of 50-70% mineral, 20-40% organic matrix, and 5-10% water, by weight [1], plays a number of roles in the body, but its main functions are protecting internal organs, providing mechanical support, acting as a reservoir for calcium and phosphate, and supporting the hematopoietic bone marrow environment [2]. The mineral phase, primarily made up of hydroxyapatite (HA), provides rigidity and strength, while the organic matrix, consisting of approximately 90% collagen type I, and water, present in the vascular-lacunar-canalicular cavities and bound to the extracellular matrix (ECM), provide flexibility and toughness [3,4]. However, the overall strength of bone is a function of bone mass, mineral density, the geometry and microstructure of the bone, and the direction of the applied forces [5].

In an effort to optimize strength and function, the body forms a mixed network of compact and porous bone. Compact cortical bone, making up 80 % of the bone in the body, is found primarily along long bone shafts (diaphyses) and along flat bone surfaces, while porous trabecular bone, making up the remaining 20 % of bone in the body, is found primarily inside the ends of long bones (metaphysis) and between flat bone surfaces [6]. Cortical bone, with a porosity of 5-25% [7], a compressive modulus of 11.5-17 GPa, and a compressive strength of 130-200 MPa [8], contributes most to bone strength. In contrast, trabecular bone, with a porosity of 40-95%, has a lower compressive modulus (0.12-1.1 GPa) and compressive strength (0.1-16 MPa). While trabecular bone is weaker than cortical bone, it plays an important role in distributing mechanical loads.

Bone is constantly being replaced and reshaped through a process called bone remodeling [9,10]. Remodeling, which involves the removal or old or damaged bone followed by the deposition of new bone, takes place to repair microdamage or meet everchanging mechanical needs. Remodeling is always occurring, because different regions of bone are constantly exposed to mechanical loads of various amplitudes and frequencies during movement and posture maintenance. Mechanical loading from physical activity or vibration therapy can result in new bone formation, but repetitive or excessive loading can result

in microcracks that require repair. In contrast, disuse or inactivity from bedrest can result in poor nutrient transfer and waste disposal and, eventually, bone loss. However, even when baseline activity is maintained, mature bone is being replaced with new bone at a rate of 10% per year [9,10].

Bone growth, remodeling, and repair are performed and coordinated primarily by four types of cells and their precursors: osteocytes, osteoblasts, osteoclasts, and bone lining cells [11]. Osteocytes, which make up 90 % of bone cells, are terminally differentiated osteoblasts that have become embedded within mineralized bone. These cells reside in segregated cavities, called lacunae, and are connected to each other and to the bone surface by a fluid filled network of channels, called canaliculi. When bone is damaged, nearby osteocytes release a variety of signaling factors that prompt osteoblasts on the bone surface to recruit osteoclast precursor cells from the bone marrow to the damaged bone site [12]. Osteoblasts are the cells responsible for synthesizing new bone, but they also induce hematopoietic stem cell differentiation into multinucleated osteoclasts through RANK/RANKL signaling. In contrast to osteoblasts, osteoclasts resorb old or damaged bone using a combination of protons, to create an acidic environment and dissolve bone mineral, and proteases, to degrade the collagen type I [13]. Once the osteoclasts remove the old or damaged bone, osteoblasts synthesize new bone in its place and either undergo apoptosis, become imbedded in bony matrix and become osteocytes, or transform into bone-lining cells.

While microdamage can be repaired through bone remodeling, fractures, from trauma, disease, or overuse, cause significantly more damage to the bone and surrounding tissues and require a different set of biological processes to contain and repair the injury and recover bone strength, shape, and function.

2.2   The general principles of fracture repair

With over 7 million fractures being treated annually, bone fractures are the most common musculoskeletal condition that requires medical resources in the United States [14]. Fractures cause structural damage to the bone and surrounding tissues, bleeding, high levels of mechanical strain, and hypoxia, and the formation of new bone is a spatially and temporally complex process that involves a wide variety of cells and growth factors [15–17]. After stemming the bleeding and protecting against infection, the

physiological response shifts towards reducing interfragmentary strain (IFS). IFS is defined as the movement within a fracture gap relative to the initial distance between bone fragments, and, along with biological healing potential and hypoxia, it is one of the preeminent variables that control fracture repair. If there is minimal space between the bone fragments and very little IFS, healing will progress through primary fracture repair. This process is similar to bone remodeling, in that bone forming osteoblasts attempt to directly synthesize bone between the two cortices [18]. However, because it is difficult to maintain low IFS (less than 2%) and close contact between bone fragments, most fractures heal through secondary fracture repair, which is a combination of intramembranous and endochondral bone formation. Unlike primary fracture repair, secondary fracture repair often progresses from the fracture hematoma, through a soft callus intermediary, to a hard boney callus. Early on in this process, the fibrin clots are replaced by granulation tissue, which, in turn, is replaced by a cartilaginous callus that provides temporary stability to the fracture site. Where the soft tissue callus is exposed to less mechanical strain, chondrocytes undergo hypertrophy and excrete angiogenic factors that promote vascular ingrowth and, therefore, increase oxygen tension. Bone-forming osteoblasts can then infiltrate these oxygenated regions of the callus and produce mineralized matrix, which is stiffer than the calcified cartilage previously stabilizing the fracture. This healing process continues until IFS is sufficiently low enough to allow the hard tissue callus to undergo bone remodeling [19]. Eventually, the bone will be fully healed, and strain within the bone will return to pre-fracture levels.

However, if the fracture is not exposed to proper IFS or if a patient's biological healing capacity is inadequate, delayed fracture repair or nonunion can occur. A number of patient-dependent risk factors, including age, medical comorbidities, smoking status, non-steroidal anti-inflammatory use, and nutritional deficiencies, and patient independent risk factors, including the type and location of the fracture, severity of soft tissue injury, presence of infection, and quality of surgical treatment, impact the prospect for delayed fracture repair or nonunion. Delayed fracture healing is defined as slower than normal healing while nonunion is defined as the cessation of fracture repair. Most delayed unions eventually heal, but fixation failure is possible if the device is unable to withstand mechanical loading for an extended period of time. Other cases of delayed union can become nonunions in the absence of surgical intervention [20]. Nonunion

can be diagnosed radiographically by persistent fracture lines, the absence of bony bridging, or the lack of progressive healing on serial radiographs [21]. Nonunion can also be identified by persistent pain, deformity near the fracture, or broken implants.

Nonunion can further be classified as being hypertrophic or atrophic. Hypertrophic nonunion, typically identified by the presence of a large callus or the formation of an "elephant foot false joint", reflects sufficient vascularization but inadequate immobilization [22–25]. For this type of nonunion, improving the mechanical stability at the fracture without disrupting the blood supply usually results in successful fracture repair [26–28]. In contrast, atrophic nonunion, typically identified by the presence of a small callus or a false joint with rounded cortical bone ends, is often the result of poor vascularization or inadequate biological healing potential. Atrophic nonunion usually requires the resection of fibrous tissue and non-viable bone, from the fracture site, and the implantation of autologous bone graft (autograft) to support the biological healing process [29–31], but some atrophic nonunions are well vascularized [32–34] and can be treated with improved mechanical stability [35]. Autograft alternatives can be utilized in some cases, and these growth factors and bone graft materials will be discussed in **Section 2.6**.

2.3   Current fixation strategies for fracture repair

Despite bone's remarkable capacity to repair damage, fractures that involve bone breaking into three or more pieces (i.e. comminuted fracture) or bone puncturing the skin often require surgical intervention for proper healing to occur. To improve the healing outcomes of these complex long bone fractures, patients are surgically fitted with fixation devices that help maintain the positions of the bone fragments and control the amount of movement within the fracture. However, weight-bearing fractures, which are subjected to repetitive, dynamic loading from daily activities, can be particularly challenging to treat, because patients often exceed prescribed weight-bearing limits [36]. Premature loading also increases the risk of fixation failure [37,38], but there are a number of physiologic and socioeconomic benefits to early weight-bearing, including improved healing [26], reduced incidence of venous thrombosis,[39] less energy expenditure,[40] and faster return to work and leisure [41,42].

Depending on the severity of the fracture, a number of fixation strategies can be considered. Casting or bracing can be used for stable closed fractures, while external fixation, bridge plating, and intramedullary (IM) nailing are typically used for unstable fractures with higher amounts of interfragmentary strain [16]. IM nailing has become the standard of care for diaphyseal fractures of the tibia and femur [43–45], because periosteal tissue and vascularity can be preserved and early weight-bearing can be possible. Furthermore IM nails (IMNs) are load-sharing fixation devices that can be designed to control IFS and influence healing [46]. Increased IFS can be achieved by using nails fabricated from more flexible materials, by using hollow nails, or by using smaller diameter nails. In contrast, coupling endosteal reaming with larger diameter IMNs increases the contact between the nail and the endosteal surface and provides greater fixation stability [47,48]. While IM nailing strategies can be tailored to better control the mechanical environment within the fracture, gaps in knowledge, regarding how to balance the amount, duration, and timing of IFS during fracture repair against a patient's biological healing capacity, make it challenging to optimize care [15,20,46].

2.4   The mechanobiology of fracture repair

While it is well known that interfragmentary strain affects the fracture healing response [15,49], the ideal amount, mode (compressive, tensile or shear), and timing (early or late) of this applied strain has not been elucidated. In humans, less than 2% strain is thought to promote intramembranous ossification while fractures subjected to strains between 2 - 10% are thought to heal primarily through endochondral ossification [43]. However, IFS exceeding 10% has the potential to hinder fracture repair by disrupting angiogenesis and causing fibrosis [50]. The magnitude of strain can somewhat be controlled by selecting the fixator type and stiffness or by prescribing a specific weight-bearing regimen [51], but the amount of strain will vary throughout the healing process as a callus forms and is replaced by bone [52].

In addition to magnitude, the mode of IFS affects fracture repair. Axial strain, resulting from compression or tension, is generally thought to be beneficial as long as the magnitude and timing of the strain is appropriate [49,53,54]. Shear strain, brought about by translational or rotational motion, is more controversial, with some studies suggesting that it is detrimental to fracture healing [55–58] while others argue

that it is neutral [59] or beneficial [60]. However, the mode of IFS is difficult to control, because most fixation devices engender a variety of movements at the fracture site [61]. For example, the bending of IMNs generates compressive strain along one side of the fracture and tensile strain on the other, and, if the nail doesn't fit tightly within the medullary canal, there will be nail-bone toggling that generates shear strain.

Finally, the timing of IFS, which can be controlled by prescribing a specific weight-bearing regimen or by changing fixation device stiffness at a given time-point (dynamization or reverse dynamization), can determine how quickly a fracture heals. If too much IFS is applied early in the healing process, fracture repair can be prolonged [62], but some IFS early in the healing process is thought to be beneficial, especially when IFS is reduced once the callus has formed [63–65]. Similarly, some IFS later in the healing process has been shown to expedite healing [66,67]. Further research is required to conclude whether it is better to increase or decrease IFS at a given time-point and to determine when that change in IFS should be made.

2.5   *In vitro* and *in silico* models of fracture repair

Many pre-clinical fracture repair studies utilize *in vivo* models, because they allow researchers to observe all the relevant biological processes and their interactions, investigate the impacts of various disease states, and trial potential fixation strategies. However, animal models do not fully recapitulate healing patterns in humans [68], and there is a constant push to replace, reduce, and refine animal models whenever possible [69]. *In vitro* and *in silico* models are important pre-clinical tools that can help researchers better understand and predict fracture repair and can guide future *in vivo* studies; thus, reducing costs, time, and waste.

2.5.1 *In vitro* models of fracture repair

In contrast to *in vivo* models, which study a body's entire response to a stimulus or disease state, i*n vitro* models are typically used to study how mechanical forces, growth factors, or drug therapies affect the behavior of one or more cell types [70,71]. These models can also be used to probe specific cell signaling pathways without the presence of confounding factors from other cell types or environmental conditions.

In vitro models often rely on culturing bone cells, that have been isolated from patient tissues or purchased as immortal cell lines, on tissue culture plastic or within a scaffold and exposing these cells to a variety of experimental conditions, such as novel pharmaceuticals, scaffold materials or architectures, oxygen tension levels, or growth factors. Commonly used assays analyze cell shape, size, differentiation, migration, proliferation, and apoptosis, cytoplasmic, membrane-bound, and secreted proteins, gene expression, and ECM composition [72].

Historically, two-dimensional (2D) scaffolds have been used to investigate bone growth and remodeling *in vitro*, but recent studies have shown that cells grown on three-dimensional (3D) scaffolds behave more like their *in vivo* counterparts [73]. Similarly, static culture has historically been used to narrow down potential drug treatment candidates or cell signaling pathways of interest, but mechanical stimuli should be added, when possible, to more effectively recapitulate physiologic conditions [74,75]. Dynamic culture can promote sustained cell viability, improved cell infiltration, and the formation of larger tissue engineered constructs, by facilitating the constant exchange of nutrients and waste products [76]. Dynamic culture can also be used to apply constant or cyclic mechanical stimuli, and some of the parameters often investigated include the magnitude and frequency of the stimulus, the number of cycles, and the dwell time between cycles [77,78]. To apply fluid flow and its associated wall shear stress (WSS), researchers use a variety of bioreactors including spinner flasks, parallel plate flow chambers, perfusion columns, and microfluidic chambers [79]. Compression or tension can also be applied to cells in 2D and 3D culture using lab-built or commercial systems [80,81].

While *in vitro* models can help researchers develop a deeper understanding of cell behaviors under specific experimental conditions, they are incapable of including all relevant growth factors, cell populations, changes in vascularization, and pharmacokinetics [82,83]. For these reasons, many results observed *in vitro* do not translate *in vivo* [84].

2.5.2 *In silico* models of fracture repair.

In silico models often use finite element analysis (FEA) simulations to predict how various mechanical or biological factors affect fracture repair. Some simulations focus solely on IFS and the

predicted stresses on the bone and fixator [85] while others include algorithms for cell migration and differentiation, growth factor diffusion, or oxygen tension to predict healing patterns [86]. *In silico* models are often designed to initially match histological tissue distributions from a previous *in vivo* study or stress-strain data from a previous *ex vivo* study before being used to predict how different experimental conditions will change these distributions and the mechanical environment in and around the fracture during the fracture repair process. These results can be used to plan future *in vivo* studies and reduce the number of experimental conditions and animals required.

Many simulations are based on the mechanobiological theories that have been proposed to predict how different mechanical stimuli affect callus size and composition throughout the fracture healing process [53,87]. The theories proposed by Carter, D.R., et al. and Claes, L.E. & Heigele, C.A. predict that high hydrostatic stresses will support cartilage formation within the callus, that a combination of high hydrostatic stress and mechanical strain will promote fibrous tissue, and that low hydrostatic stress and mechanical strain will result in direct bone formation [88,89]. In contrast, the theory proposed by Lacroix, D. & Prendergast, P.J. asserts that the octahedral shear strain within the ECM and the velocity of the fluid through the ECM are the primary stimuli that drive cell differentiation. Following this theory, low, medium, and high levels of octahedral shear strain or fluid velocity are associated with the production of bone, cartilage, and fibrous tissue, respectively [90,91].

While *in silico* models provide valuable insight into the mechanobiology of fracture repair and allow researchers to quickly and humanely investigate a variety of experimental parameters, these simulations rely on stimulus thresholds that vary between large and small animals and often do not account for disease, age, or comorbidities [92,93]. Furthermore, *in silico* models require *in vivo* or *ex vivo* validation to confirm their accuracy [94,95], so the use of animals can't be completely eliminated.

2.6   Current bone grafting strategies for fracture repair

More than two million bone grafting procedures are performed annually worldwide [96], and, as it pertains to fracture repair, bone grafting is required when a fracture is unable to spontaneously heal on its

own [97,98]. This lack of healing can occur when too much bone is damaged or when a patient exhibits poor biological healing potential. Autograft, defined as morselized bone harvested from another bone in the patient's own body, has long been considered the gold standard for bone grafts, because of its osteoconductive, osteoinductive, and osteogenic properties, but its use is hampered by donor site morbidity and limited supply. For these reasons, allograft, defined as morselized bone harvested from another patient or a cadaver, is also frequently used in bone grafting procedures [99]. However, unlike autograft, allograft exhibits limited bioactivity and has the potential to trigger an immune response. There remains a need for an abundantly available bone graft alternative that can be used to support fracture repair without causing adverse side effects, and synthetic bone grafts, biological agents, or cell-based therapies can potentially fill this clinical demand.

<u>2.6.1 Synthetic bone grafts</u>

Synthetic bone grafts, defined here as materials that are artificially produced or isolated from non-human natural sources, provide value in that the materials are not hindered by the lack of biological supply. Ceramics are biocompatible and osteoconductive [100], but ceramics alone are inherently brittle, weak under repetitive loading, and slow to resorb [101]. Calcium-based ceramics, including calcium sulphate, HA, β-tricalcium phosphate (β-TCP), and biphasic calcium phosphate, are the most common ceramics used in synthetic bone grafts [101,102]. Calcium sulphate is osteoconductive and resorbable, but it rapidly dissolves by chemical dissolution and is mechanically weak relative to calcium phosphate-based ceramics. In contrast, HA and β-TCP degrade slowly by way of a cell-mediated resorption mechanism. β-TCP resorbs more quickly than HA, but, due to its increased porosity, is mechanically weaker. To create a calcium phosphate-based ceramic with more tailored mechanical and resorptive properties, the two ceramics have been combined, in various HA:β-TCP ratios, to form biphasic calcium phosphate [103]. However, biphasic calcium phosphate does not solve the problems that ceramics have with brittleness and low fatigue strength.

Polymeric bone grafts tend to be more compliant and elastic than ceramics, but many polymers aren't osteoconductive, resorb too quickly, or don't resorb at all [102]. Natural polymers, including collagen, silk fibroin, chitosan, alginate, cellulose, and hyaluronic acid, can be isolated from animal or plant tissues

and used in variety of sponges, electrospun scaffolds, and gels [104,105]. These polymers are biodegradable and favor cell adhesion, but some lack the mechanical or degradation properties for certain applications. Synthetic polymers, including poly(methyl methacrylate), poly (ϵ-caprolactone), polylactide, poly (lactide-co-glycolide), and poly(ester urethane), can be fabricated into scaffolds or cements with a wide range of mechanical properties and degradations rates, but some degradation products can damage surrounding tissues [106]. These synthetic polymers are typically less osteoconductive than natural polymers, but recent studies have shown that augmenting these polymers with ceramic particles improves their osteoconductivity [107–110]. Additional research is required to determine how well these composite materials will function clinically.

2.6.2 Biological agents and cell-based therapies

While many of the synthetic bone grafts discussed in previous section are osteoconductive, they do not provide autograft's osteoinductive benefits. Because of this, interest in using exogenous growth factors, including bone morphogenic proteins, fibroblast growth factors, vascular endothelial growth factor, platelet-derived growth factor, and transforming growth factor-β, to bolster osteoblast recruitment, bone deposition, and revascularization has grown [98,111,112]. However, direct injections of these growth factors into a fracture often requires a higher concentration of material being delivered in a short window of time and introduces a higher risk of off-target effects. Integrating these growth factors into a synthetic bone graft can engender a more controlled release and provide an osteoconductive template for new bone to grow into, but more investigation and optimization is needed.

Another strategy, for replacing the osteoinductive properties of autograft, focuses on using cells to promote fracture healing [113,114]. The vast majority of studies use mesenchymal stem cells (MSCs), that are either harvested from patients and expanded or derived from embryonic or induced pluripotent stem cells, to create implantable cell-containing bone grafts. These constructs must contain MSCs throughout their entire structures, meaning that the cell-laden bone grafts must be cultured and maintained in a bioreactor until the MSCs can proliferate and migrate deep into the bone graft's core. Furthermore, the MSCs must survive implantation and the poorly vascularized initial stages of fracture repair. Recent studies have

explored whether this can be achieved by pre-conditioning MSCs in a hypoxic, pro-inflammatory, fracture-like environment [115] or by differentiating MSCs towards a hypertrophic chondrocyte state [116], but, while these cell-based strategies have shown promise in preclinical trials, their potential is currently limited by insufficient cell harvesting and expansion practices.

References:

1. Black, J. D. & Tadros, B. J. Bone structure: from cortical to calcium. *Orthop. Trauma* **34**, 113–119 (2020).
2. Ralston, S. H. Bone structure and metabolism. *Med. (United Kingdom)* **41**, 581–585 (2013).
3. Lin, X., Patil, S., Gao, Y. G. & Qian, A. The Bone Extracellular Matrix in Bone Formation and Regeneration. *Front. Pharmacol.* **11**, 1–15 (2020).
4. Nyman, J. S. *et al.* The influence of water removal on the strength and toughness of cortical bone. *J. Biomech.* **39**, (2006).
5. Clarke, B. Normal bone anatomy and physiology. *Clin. J. Am. Soc. Nephrol.* **3 Suppl 3**, 131–139 (2008).
6. Ott, S. M. Cortical or Trabecular Bone: What's the Difference? *Am. J. Nephrol.* **47**, 373–375 (2018).
7. Morgan, E. F., Unnikrisnan, G. U. & Hussein, A. I. Bone Mechanical Properties in Healthy and Diseased States. *Annu. Rev. Biomed. Eng.* **20**, 119–143 (2018).
8. Gerhardt, L. C. & Boccaccini, A. R. Bioactive glass and glass-ceramic scaffolds for bone tissue engineering. *Materials (Basel).* **3**, 3867–3910 (2010).
9. Pivonka, P., Park, A. & Forwood, M. R. Multiscale Mechanobiology of Bone Remodeling and Adaptation. in (ed. Pivonka, P.) 1–60 (Springer International Publishing, 2018). doi:10.1007/978-3-319-58845-2
10. Bergmann, P. *et al.* Loading and Skeletal Development and Maintenance. *J. Osteoporos.* **2011**, 1–15 (2011).
11. Bilgiç, E., Boyacıoğlu, Ö., Gizer, M., Korkusuz, P. & Korkusuz, F. Architecture of bone tissue and its adaptation to pathological conditions. *Comp. Kinesiol. Hum. Body* 71–90 (2020). doi:10.1016/b978-0-12-812162-7.00006-0
12. Raggatt, L. J. & Partridge, N. C. Cellular and molecular mechanisms of bone remodeling. *J. Biol. Chem.* **285**, 25103–25108 (2010).
13. Sørensen, M. G. *et al.* Characterization of osteoclasts derived from CD14+ monocytes isolated from peripheral blood. *J. Bone Miner. Metab.* **25**, 36–45 (2006).
14. Watkins-Castillo, S. & Andersson, G. *United States Bone and Joint Initiative: The Burden of Musculoskeletal Diseases in the United States (BMUS). The Burden of Musculoskeletal diseases int he United States* (2014).
15. Baker, C. E. *et al.* Bone Fracture Acute Phase Response—A Unifying Theory of Fracture Repair: Clinical and Scientific Implications. *Clin. Rev. Bone Miner. Metab.* **16**, 142–158 (2018).
16. Claes, L., Recknagel, S. & Ignatius, A. Fracture healing under healthy and inflammatory conditions. *Nat. Rev. Rheumatol.* **8**, 133–143 (2012).
17. McKibbin, B. The biology of fracture healing in long bones. *J. Bone Joint Surg. Br.* **60-B**, 150–62 (1978).
18. Giannoudis, P. V., Einhorn, T. A. & Marsh, D. Fracture healing: The diamond concept. *Injury* **38**, S3–S6 (2007).
19. Schindeler, A., McDonald, M. M., Bokko, P. & Little, D. G. Bone remodeling during fracture

repair: The cellular picture. *Semin. Cell Dev. Biol.* **19**, 459–466 (2008).

20. Kostenuik, P. & Mirza, F. M. Fracture healing physiology and the quest for therapies for delayed healing and nonunion. *J. Orthop. Res.* **35**, 213–223 (2017).

21. Hak, D. J. *et al.* Delayed union and nonunions: Epidemiology, clinical issues, and financial aspects. *Injury* **45**, S3–S7 (2014).

22. Babhulkar, S. S., Pande, K. & Babhulkar, S. Nonunion of the diaphysis of long bones. *Clin. Orthop. Relat. Res.* 50–56 (2005). doi:10.1097/01.blo.0000152369.99312.c5

23. Gaston, M. S. & Simpson, A. H. R. W. Inhibition of fracture healing. *J. Bone Jt. Surg. - Ser. B* **89**, 1553–1560 (2007).

24. Panagiotis, M. Classification of non-union. *Injury* **36**, 30–37 (2005).

25. SK, S. Fracture Non-Union: A Review of Clinical Challenges and Future Research Needs. *Malaysian Orthop. J.* **13**, 1–10 (2019).

26. Elliott, D. S. *et al.* A unified theory of bone healing and nonunion. *Bone Jt. J.* **98B**, 884–891 (2016).

27. Rüedi, T. P. & Murphy, W. M. AO Principles of Fracture Management. in *AO Principles of Fracture Management* (eds. Colton, C. L., Dell'Oca, A. F., Holz, U., Kellam, J. F. & Ochsner, P. E.) 864 (AO Publishing, 2000). doi:10.1055/b-0038-160811

28. Vaughn, J. *et al.* Nail Dynamization for Delayed Union and Nonunion in Femur and Tibia Fractures. *Orthopedics* **39**, e1117–e1123 (2016).

29. Blokhuis, T. J., Calori, G. M. & Schmidmaier, G. Autograft versus BMPs for the treatment of non-unions: What is the evidence? *Injury* **44**, S40–S42 (2013).

30. Giannoudis, P. V. *et al.* The synergistic effect of autograft and BMP-7 in the treatment of atrophic nonunions. *Clin. Orthop. Relat. Res.* **467**, 3239–3248 (2009).

31. Nauth, A. *et al.* Principles of Nonunion Management: State of the Art. *J. Orthop. Trauma* **32**, S52–S57 (2018).

32. Brownlow, H. C., Reed, A. & Simpson, A. H. R. W. The vascularity of atrophic non-unions. *Injury* **33**, 145–150 (2002).

33. Reed, A. A. C., Joyner, C. J., Brownlow, H. C. & Simpson, A. H. R. W. Human atrophic fracture non-unions are not avascular. *J. Orthop. Res.* **20**, 593–599 (2002).

34. Reed, A. A. C., Joyner, C. J., Isefuku, S., Brownlow, H. C. & Simpson, A. H. R. W. Vascularity in a new model of atrophic nonunion. *J. Bone Jt. Surg. - Ser. B* **85**, 604–610 (2003).

35. Ferreira, N., Marais, L. C. & Aldous, C. Mechanobiology in the management of mobile atrophic and oligotrophic tibial nonunions. *J. Orthop.* **12**, S182–S187 (2015).

36. Thewlis, D. *et al.* Postoperative weight bearing and patient reported outcomes at one year following tibial plateau fractures. *Injury* **48**, 1650–1656 (2017).

37. Ali, A. M., El-Shafie, M. & Willett, K. M. Failure of fixation of tibial plateau fractures. *J. Orthop. Trauma* **16**, 323–329 (2002).

38. Williamson, M., Iliopoulos, E., Jain, A., Ebied, W. & Trompeter, A. Immediate weight bearing after plate fixation of fractures of the tibial plateau. *Injury* **49**, 1886–1890 (2018).

39. Riou, B. *et al.* Incidence and risk factors for venous thromboembolism in patients with nonsurgical isolated lower limb injuries. *Am. J. Emerg. Med.* **25**, 502–508 (2007).

40. Westerman, R. W., Hull, P., Hendry, R. G. & Cooper, J. The physiological cost of restricted weight bearing. *Injury* **39**, 725–727 (2008).

41. Simanski, C. J. P. *et al.* Functional treatment and early weightbearing after an ankle fracture: A prospective study. *J. Orthop. Trauma* **20**, 108–114 (2006).

42. Kraus, T. M. *et al.* Return to sports activity after tibial plateau fractures: 89 cases with minimum 24-month follow-up. *Am. J. Sports Med.* **40**, 2845–2852 (2012).

43. Beltran, M. J., Collinge, C. A. & Gardner, M. J. Stress Modulation of Fracture Fixation Implants. *J. Am. Acad. Orthop. Surg.* **24**, 711–719 (2016).

44. Kubiak, E. N., Beebe, M. J., North, K., Hitchcock, R. & Potter, M. Q. Early Weight Bearing After Lower Extremity Fractures in Adults. *J. Am. Acad. Orthop. Surg.* **21**, 727–738 (2013).

45.   Wood, G. W. Intramedullary nailing of femoral and tibial shaft fractures. in *Journal of Orthopaedic Science* (2006). doi:10.1007/s00776-006-1061-6

46.   Rosa, N. *et al.* Intramedullary nailing biomechanics: Evolution and challenges. *Proc. Inst. Mech. Eng. Part H J. Eng. Med.* **233**, 295–308 (2019).

47.   Bhandari, M. *et al.* Randomized trial of reamed and unreamed intramedullary nailing of tibial shaft fractures. *J. Bone Jt. Surg. - Ser. A* **90**, 2567–2578 (2008).

48.   Larsen, L. B., Madsen, J. E., Høiness, P. R. & Øvre, S. Should insertion of intramedullary nails for tibial fractures be with or without reaming? A prospective, randomized study with 3.8 years' follow-up. *J. Orthop. Trauma* **18**, 144–149 (2004).

49.   Carter, D. R., Beaupré, G. S., Giori, N. J. & Helms, J. A. Mechanobiology of skeletal regeneration. *Clin. Orthop. Relat. Res.* S41-55 (1998).

50.   Claes, L., Eckert-Hübner, K. & Augat, P. The effect of mechanical stability on local vascularization and tissue differentiation in callus healing. *J. Orthop. Res.* **20**, 1099–1105 (2002).

51.   Augat, P., Hollensteiner, M. & von Rüden, C. The role of mechanical stimulation in the enhancement of bone healing. *Injury* **52**, S78–S83 (2021).

52.   Claes, L. *et al.* Effects of mechanical factors on the fracture healing process. *Clin Orthop Relat Res* **355**, 132–147 (1998).

53.   Betts, D. C. & Müller, R. Mechanical regulation of bone regeneration: Theories, models, and experiments. *Front. Endocrinol. (Lausanne).* **5**, 1–14 (2014).

54.   Smith-Adaline, E. A. *et al.* Mechanical environment alters tissue formation patterns during fracture repair. *J. Orthop. Res.* **22**, 1079–1085 (2004).

55.   Augat, P. *et al.* Interfragmentary movement in diaphyseal tibia fractures fixed with locked intramedullary nails. *J. Orthop. Trauma* **22**, 30–36 (2008).

56.   Claes, L. *et al.* The mode of interfragmentary movement affects bone formation and revascularization after callus distraction. *PLoS One* **13**, 1–12 (2018).

57.   Schell, H. *et al.* The course of bone healing is influenced by the initial shear fixation stability. *J. Orthop. Res.* **23**, 1022–1028 (2005).

58.   Steiner, M. *et al.* Prediction of fracture healing under axial loading, shear loading and bending is possible using distortional and dilatational strains as determining mechanical stimuli. *J. R. Soc. Interface* **10**, (2013).

59.   Bishop, N. E. *et al.* Shear Does Not Necessarily Inhibit Bone Healing. *Clin. Orthop. Relat. Res.* **443**, 307–314 (2006).

60.   Park, S. H., O'Connor, K., Mckellop, H. & Sarmiento, A. The influence of active shear or compressive motion on fracture-healing. *J. Bone Jt. Surg. - Ser. A* **80**, 868–878 (1998).

61.   Meyers, N. *et al.* Characterization of interfragmentary motion associated with common osteosynthesis devices for rat fracture healing studies. *PLoS One* **12**, (2017).

62.   Epari, D. R., Schell, H., Bail, H. J. & Duda, G. N. Instability prolongs the chondral phase during bone healing in sheep. *Bone* **38**, 864–870 (2006).

63.   Bartnikowski, N. *et al.* Modulation of fixation stiffness from flexible to stiff in a rat model of bone healing. *Acta Orthop.* **88**, 217–222 (2017).

64.   Glatt, V. *et al.* Improved healing of large segmental defects in the rat femur by reverse dynamization in the presence of bone morphogenetic protein-2. *J. Bone Jt. Surg. - Ser. A* **94**, 2063–2073 (2012).

65.   Glatt, V., Tepic, S. & Evans, C. Reverse Dynamization. *J. Am. Acad. Orthop. Surg.* **24**, e60–e61 (2016).

66.   Claes, L. *et al.* Late Dynamization by Reduced Fixation Stiffness Enhances Fracture Healing in a Rat Femoral Osteotomy Model. *J. Orthop. Trauma* **25**, 169–174 (2011).

67.   Vicenti, G. *et al.* The ideal timing for nail dynamization in femoral shaft delayed union and non-union. *Int. Orthop.* **43**, 217–222 (2019).

68.   Nunamaker, D. M. Experimental Models of Fracture Repair. *Clin. Orthop. Relat. Res.* **355S**, S56–S65 (1998).

69. Hubrecht & Carter. The 3Rs and Humane Experimental Technique: Implementing Change. *Animals* **9**, 754 (2019).
70. Caddeo, S., Boffito, M. & Sartori, S. Tissue Engineering Approaches in the Design of Healthy and Pathological In Vitro Tissue Models. *Front. Bioeng. Biotechnol.* **5**, 1–22 (2017).
71. Owen, R. & Reilly, G. C. In vitro models of bone remodelling and associated disorders. *Front. Bioeng. Biotechnol.* **6**, 1–22 (2018).
72. *Bone Research Protocols. Methods in Molecular Biology* **816**, (Humana Press, 2012).
73. Vanderburgh, J., Sterling, J. A. & Guelcher, S. A. 3D Printing of Tissue Engineered Constructs for In Vitro Modeling of Disease Progression and Drug Screening. *Ann. Biomed. Eng.* **45**, 164–179 (2017).
74. Hao, Z. *et al.* Biophysical Stimuli as the Fourth Pillar of Bone Tissue Engineering. *Front. Cell Dev. Biol.* **9**, 1–22 (2021).
75. Wittkowske, C., Reilly, G. C., Lacroix, D. & Perrault, C. M. In Vitro Bone Cell Models: Impact of Fluid Shear Stress on Bone Formation. *Front. Bioeng. Biotechnol.* **4**, (2016).
76. Guller, A. E., Grebenyuk, P. N., Shekhter, A. B., Zvyagin, A. V. & Deyev, S. M. Bioreactor-based tumor tissue engineering. *Acta Naturae* (2016).
77. Robling, A. G., Castillo, A. B. & Turner, C. H. Biomechanical and Molecular Regulation of Bone Remodeling. *Annu. Rev. Biomed. Eng.* **8**, 455–498 (2006).
78. Skerry, T. M. One mechanostat or many? Modifications of the site-specific response of bone to mechanical loading by nature and nurture. *J. Musculoskelet. Neuronal Interact.* **6**, 122–127 (2006).
79. Gaspar, D. A., Gomide, V. & Monteiro, F. J. The role of perfusion bioreactors in bone tissue engineering. *Biomatter* (2012). doi:10.4161/biom.22170
80. Rauh, J., Milan, F., Günther, K. P. & Stiehler, M. Bioreactor systems for bone tissue engineering. *Tissue Eng. - Part B Rev.* **17**, 263–280 (2011).
81. Ravichandran, A., Liu, Y. & Teoh, S. H. Review: bioreactor design towards generation of relevant engineered tissues: focus on clinical translation. *J. Tissue Eng. Regen. Med.* **12**, e7–e22 (2018).
82. Brown, G. N., Sattler, R. L. & Guo, X. E. Experimental studies of bone mechanoadaptation: Bridging in vitro and in vivo studies with multiscale systems. *Interface Focus* **6**, (2016).
83. Fini, M. & Giardino, R. In vitro and in vivo tests for the biological evaluation of candidate orthopedic materials: Benefits and limits. *J. Appl. Biomater. Biomech.* **1**, 155–63 (2003).
84. Seyhan, A. A. Lost in translation: the valley of death across preclinical and clinical divide – identification of problems and overcoming obstacles. *Transl. Med. Commun.* **4**, 1–19 (2019).
85. Lewis, G. S., Mischler, D., Wee, H., Reid, J. S. & Varga, P. Finite Element Analysis of Fracture Fixation. *Curr. Osteoporos. Rep.* **19**, 403–416 (2021).
86. Boccaccio, A. *et al.* Finite element method (FEM), mechanobiology and biomimetic scaffolds in bone tissue engineering. *Int. J. Biol. Sci.* **7**, 112–32 (2011).
87. Anderson, D. D. *et al.* Computational techniques for the assessment of fracture repair. *Injury* **45**, S23–S31 (2014).
88. Carter, D. R., Blenman, P. R. & Beaupré, G. S. Correlations between mechanical stress history and tissue differentiation in initial fracture healing. *J. Orthop. Res.* **6**, 736–748 (1988).
89. Claes, L. E. & Heigele, C. A. Magnitudes of local stress and strain along bony surfaces predict the course and type of fracture healing. *J. Biomech.* **32**, 255–266 (1999).
90. Lacroix, D. & Prendergast, P. J. A mechano-regulation model for tissue differentiation during fracture healing: Analysis of gap size and loading. *J. Biomech.* **35**, 1163–1171 (2002).
91. Prendergast, P. J., Huiskes, R. & Søballe, K. Biophysical stimuli on cells during tissue differentiation at implant interfaces. *J. Biomech.* (1997). doi:10.1016/S0021-9290(96)00140-6
92. Razi, H. *et al.* Skeletal maturity leads to a reduction in the strain magnitudes induced within the bone: A murine tibia study. *Acta Biomater.* **13**, 301–310 (2015).
93. Wehner, T., Steiner, M., Ignatius, A., Claes, L. & Aegerter, C. M. Prediction of the time course of callus stiffness as a function of mechanical parameters in experimental rat fracture healing studies

- A numerical study. *PLoS One* **9**, 1–16 (2014).

94. Anderson, A. E., Ellis, B. J. & Weiss, J. A. Verification, validation and sensitivity studies in computational biomechanics. *Comput. Methods Biomech. Biomed. Engin.* **10**, 171–84 (2007).

95. Burkhart, T. A., Andrews, D. M. & Dunning, C. E. Finite element modeling mesh quality, energy balance and validation methods: A review with recommendations associated with the modeling of bone tissue. *J. Biomech.* **46**, 1477–1488 (2013).

96. Campana, V. *et al.* Bone substitutes in orthopaedic surgery: from basic science to clinical practice. *J. Mater. Sci. Mater. Med.* **25**, 2445–2461 (2014).

97. Sen, M. K. & Miclau, T. Autologous iliac crest bone graft: Should it still be the gold standard for treating nonunions? *Injury* **38**, 2–7 (2007).

98. Wang, W. & Yeung, K. W. K. Bone grafts and biomaterials substitutes for bone defect repair: A review. *Bioact. Mater.* **2**, 224–247 (2017).

99. Baldwin, P. *et al.* Autograft, Allograft, and Bone Graft Substitutes: Clinical Evidence and Indications for Use in the Setting of Orthopaedic Trauma Surgery. *J. Orthop. Trauma* **33**, 203–213 (2019).

100. Moore, W. R., Graves, S. E. & Bain, G. I. Synthetic bone graft substitutes. *ANZ J. Surg.* **71**, 354–361 (2001).

101. Bohner, M. Resorbable biomaterials as bone graft substitutes. *Mater. Today* **13**, 24–30 (2010).

102. Bohner, M. Design of ceramic-based cements and putties for bone graft substitution. *Eur. Cells Mater.* **20**, 1–12 (2010).

103. Bouler, J. M., Pilet, P., Gauthier, O. & Verron, E. Biphasic calcium phosphate ceramics for bone reconstruction: A review of biological response. *Acta Biomater.* **53**, 1–12 (2017).

104. Guo, L. *et al.* The role of natural polymers in bone tissue engineering. *J. Control. Release* **338**, 571–582 (2021).

105. Shi, C., Yuan, Z., Han, F., Zhu, C. & Li, B. Polymeric biomaterials for bone regeneration. *Ann. Jt.* **1**, 27–27 (2016).

106. Wei, S., Ma, J. X., Xu, L., Gu, X. S. & Ma, X. L. Biodegradable materials for bone defect repair. *Mil. Med. Res.* **7**, 1–25 (2020).

107. Ramakrishna, S., Mayer, J., Wintermantel, E. & Leong, K. W. Biomedical applications of polymer-composite materials: A review. *Compos. Sci. Technol.* (2001). doi:10.1016/S0266-3538(00)00241-4

108. Hajiali, F., Tajbakhsh, S. & Shojaei, A. Fabrication and Properties of Polycaprolactone Composites Containing Calcium Phosphate-Based Ceramics and Bioactive Glasses in Bone Tissue Engineering: A Review. *Polym. Rev.* **58**, 164–207 (2018).

109. Sultan, M. Hydroxyapatite/polyurethane composites as promising biomaterials. *Chem. Pap.* **72**, 2375–2395 (2018).

110. Zhao, D. *et al.* Poly(lactic-co-glycolic acid)-based composite bone-substitute materials. *Bioact. Mater.* **6**, 346–360 (2021).

111. Kuroda, Y., Kawai, T., Goto, K. & Matsuda, S. Clinical application of injectable growth factor for bone regeneration: A systematic review. *Inflamm. Regen.* **39**, 1–10 (2019).

112. Toosi, S. & Behravan, J. Osteogenesis and bone remodeling: A focus on growth factors and bioactive peptides. *BioFactors* 1–15 (2019). doi:10.1002/biof.1598

113. Gómez-Barrena, E. *et al.* Bone fracture healing: Cell therapy in delayed unions and nonunions. *Bone* **70**, 93–101 (2015).

114. Perez, J. R. *et al.* Tissue Engineering and Cell-Based Therapies for Fractures and Bone Defects. *Front. Bioeng. Biotechnol.* **6**, 1–23 (2018).

115. Goodman, S. B. & Lin, T. Modifying MSC Phenotype to Facilitate Bone Healing: Biological Approaches. *Front. Bioeng. Biotechnol.* **8**, 1–16 (2020).

116. Fu, R., Liu, C., Yan, Y., Li, Q. & Huang, R. L. Bone defect reconstruction via endochondral ossification: A developmental engineering strategy. *J. Tissue Eng.* **12**, (2021).

CHAPTER 3 – EFFECT OF INTRAMEDULLARY NAILING PATTERNS ON INTERFRAGMENTARY STRAIN IN A MOUSE FEMUR FRACTURE: A PARAMETRIC FINITE ELEMENT ANALYSIS

3.1   Abstract:

Delayed long bone fracture healing and nonunion continue to be a significant socioeconomic burden. While mechanical stimulation is known to be an important determinant of the bone repair process, understanding how the magnitude, mode, and commencement of interfragmentary strain (IFS) affect fracture healing can guide new therapeutic strategies to prevent delayed healing or non-union. Mouse models provide a means to investigate the molecular and cellular aspects of fracture repair, yet there is only one commercially available, clinically-relevant, locking intramedullary nail (IMN) currently available for studying long bone fractures in rodents. Having access to alternative IMNs would allow a variety of mechanical environments at the fracture site to be evaluated, and the purpose of this proof-of-concept finite element analysis study is to identify which IMN design parameters have the largest impact on IFS in a murine transverse femoral osteotomy model. Using the dimensions of the clinically relevant IMN as a guide, the nail material, distance between interlocking screws, and clearance between the nail and endosteal surface were varied between simulations. Of these parameters, changing the nail material from stainless steel (SS) to polyether ether ketone (PEEK) had the largest impact on IFS. Reducing the distance between the proximal and distal interlocking screws substantially affected IFS only when nail modulus was low. Therefore, IMNs with low modulus (e.g., PEEK) can be used alongside commercially available SS nails to investigate the effect of initial IFS or stability on fracture healing with respect to different biological conditions of repair in rodents.

3.2   Introduction:

Bone fractures are the most common musculoskeletal condition requiring medical resources in the United States, with more than 7 million patients undergoing fixation or stabilization of long bone fractures per year as estimated in 2010 [1]. While fracture repair is often uneventful, delayed healing and fracture nonunion remain a significant clinical and socioeconomic burden, with 5-10% of femoral and tibial fractures failing to heal fully. As a result, patients with impaired fracture healing require additional revision surgeries, leading to longer hospitalization stays, rehabilitation periods, increased medical expenses, and, importantly, decreased quality of life [2–4].

Delayed fracture healing and non-union can occur as a result of biological or mechanical failure. For instance, obesity, diabetes, advanced age, and smoking status can all increase the risks of delayed bone healing and non-union by altering a patient's biological potential for regenerating tissue [5–7]. Likewise, improper levels of interfragmentary strain (IFS) [8–10], defined as the movement within a fracture gap relative to the initial distance between bone fragments after fixation, can potentially delay fracture repair or lead to non-union. To overcome these barriers, bone grafting or exogenous growth factors can be applied to improve biological potential [11–13], and fixation instrumentation can be utilized to manipulate strain to promote bone growth [14–16]. Intramedullary (IM) nailing has become the standard of care for diaphyseal fractures of the tibia and femur, because early weight-bearing is possible and periosteal tissue can be better preserved than when internal plates or external fixators are utilized [17–19]. Surgeons can control fracture micromotion by selecting the nail material and diameter, and by changing working distance between the interlocking screws [20]. However, while clinical and pre-clinical studies have established that mechanical strain is an important determinant of the bone repair process [21–23], several factors, including the magnitude, mode, and start of IFS, require additional investigation before IFS can be utilized to promote optimal bone repair.

Given their experimental and temporal advantages over clinical and large animal models, including the availability of genetically modified animals, disease models, and monoclonal antibodies, more rapid fracture healing and breeding cycles, and less complicated husbandry [24–28], murine models of diaphyseal fractures are prevalent. Such fractures are commonly stabilized with either IM pins (e.g., Kirchner wire or syringe needle) [23,29], locked plates [30], or external fixation devices [31] . However, IM pins do not provide sufficient rotational stability, and

locked plates have not been used to investigate the effects of IFS on fracture healing in rodents. External fixators offer the ability to experimentally manipulate IFS throughout the course of healing [31,32], but these devices do not mimic the locked intramedullary nails (IMNs) frequently used in the clinic. RI System's MouseNail is a clinically relevant murine IMN with locking screws that supports secondary bone repair of transverse femoral osteotomies [33,34], but this construct is fixed in regards to nail material, diameter, and working distance between interlocking screws; thereby limiting its utility when investigating how IFS impacts fracture repair.

As an alternative option to iteratively designing and manufacturing murine IMNs for *in vivo* use, finite element (FE) modeling can be utilized to predict IFS distributions. These simulations can also be used to determine the relative contributions of tension, compression, and shear strain within a fracture or to evaluate the stresses within the fixation devices and surrounding bone. Some FE models have been used to quantify IFS throughout the entire time-course of fracture repair [35–38], but these studies examined only one fixation device or did not include fixation devices at all. Other groups have utilized FE models to investigate how novel IMN fixation strategies or distinct fracture geometries impact IFS and stresses within the nails and bone [39–42]. However, this approach has not been applied towards designing IMNs to stabilize transverse osteotomies or fractures in mice.

In this parametric FE analysis study, we investigated which design aspects of a locked IMN (distance between interlocking bone screws, clearance between nail and bone, and modulus of the nail) have the largest impact on the initial IFS in transverse femoral osteotomies in mice. In doing so, we hypothesized that the modulus of the nail has a larger impact on IFS than the distance between the proximal and distal interlocking screws when boundary conditions, representing maximum gait forces, compress and bend the fixed long bone. The outcomes from this study can be used to guide future *in vivo* studies.

3.3   Materials and Methods:

3.3.1 Creating a digital mouse femur from a micro-computed tomography scan

An intact right femur from a healthy 10-week-old male C57Bl/6J mouse was scanned at an isotropic voxel size of 12 µm (70 kVp, 114 µA, 300 ms) using a micro-computed tomography scanner (Scanco µCT 40, Scanco Medical, Basersdorf, Swtizerland). The femur was stored in ethanol at 4 ℃ before use. A hydroxyapatite phantom,

provided by the manufacturer, was used to convert attenuation to bone mineral density (mg-HA cm^{-3}). To maintain the trabecular bone architecture in the resulting scan, bone was segmented from the soft tissue using a lower threshold of 300 mg-HA cm^{-3} after applying a Gaussian noise filter (sigma = 0.2, support = 1). The soft tissue voxels were not included in the FE models. Using Scanco Medical's built-in image processing language, disconnected voxels were removed from the resulting segmented AIM file and a stereolithography surface mesh of the bone was generated. The surface mesh was repaired, smoothed, and simplified, in MeshLab (open-source) to reduce the total number of triangulated faces and ease computation [43,44]. Finally, to facilitate digital nail insertion and defect creation, the revised surface mesh was converted to an ACIS solid volume using a MATLAB script (MATLAB version R2019b, MathWorks, Natick, MA) [45]. The final bone geometry includes the cortical bone with a coarsened trabecular bone architecture.

3.3.2 Inserting the locked IMN and transverse osteotomy

The solid volume femur was imported into Ansys SpaceClaim (Ansys version 19.0, Ansys, Canonsburg, PA) and centered about the global origin. Initially, a cylinder, with a diameter of 0.82 mm and length of 9.5 mm, was created to mimic the dimensions of the commercially available murine IMN [46]. In subsequent thinner IMN simulations, focused on determining whether the rigid nail being investigated could engender IFS levels similar to those in the compliant nail simulations, the diameter of the nail was reduced to 0.74 mm, 0.66 mm, 0.63 mm, and 0.62 mm. In all simulations, two smooth cylinders, with a diameter of 0.33 mm and a length of 4 mm, were placed 1.75 mm or 3.5 mm from the midline of the IMN to represent medial-lateral interlocking screws spaced 3.5 mm and 7 mm apart, respectively. The IMN assembly was centered, visually, within the medullary cavity, and was inserted into the femur using SpaceClaim's built-in Boolean operations. Radial reaming of the bone was performed to create clearance between the nail and bone surfaces equal to 0.005 mm, 0.02 mm, 0.06 mm, or 0.1 mm. For the smaller-diameter rigid nails, the clearance between the nail and bone surfaces was maintained at 0.1 mm. A transverse osteotomy was created by slicing a 0.25 mm layer of bone, centered about the middle of the IMN and mid-point of the diaphysis (**Fig. 3.1(a)**). This slice represented a layer of granulation tissue, between the bone cortices, during the initial stage of healing. All disconnected bone fragments were removed from the final assembly.

3.3.3 Assigning material properties

The IMN assembly was loaded into the Ansys Static Structural module, where the assembly was meshed, material properties were assigned, boundary conditions were applied, and simulations were run. The fibrous tissue, IMN, and interlocking screws were meshed using a hexahedral dominant method while the distal and proximal bone fragments were meshed using a patch independent tetrahedral method. The resulting mesh, with approximately 4.1 x 10^5 elements and 8.4 x 10^5 nodes, had an average characteristic length and element quality of 43 µm and 0.73 µm, respectively. As listed in **Table 3.1**, each solid body was assigned a Young's modulus (E_s) and a Poisson's ratio (v) value. To predict how IMN stiffness affected IFS, the IMN was designated as either polyether ether ketone (PEEK) or stainless steel (SS). For computational simplicity, all of the materials were considered to be homogeneous, isotropic, and linearly elastic [47–49].

Table 3.1. Mechanical Properties of the Fixed Femur

Material	E_s (MPa)	v
Bone [49]	15,000	0.30
Granulation Tissue [50]	0.2	0.167
SS [51]	193,000	0.31
PEEK [51]	3,600	0.38

3.3.4 Applying boundary conditions and executing simulations

The contact regions between the nail and interlocking screws, between the nail and bone, and between the nail and granulation tissue were defined as frictional ($\mu = 0.2$) [52,53], while the contact regions between the bone and interlocking screws and between the bone and granulation tissue were bonded. To generate a maximum axial gait force of 6 times body weight (BW = 23 g) and a maximum bending moment of 10.7 x BW mm at the mid-diaphysis [54–57], a force vector of 0.352 N, 0.11 N, 1.356 N (lateral, anterior, distal) was applied to the surface of the femoral head and the center of the distal femur surface was fixed in all three dimensions (**Fig. 3.1(a)**). The analyses were run using the Ansys Mechanical direct solver. Equivalent (von Mises), maximum principal, minimum principal, and maximum shear strains were evaluated for the granulation tissue region while equivalent stress was evaluated

for the IMN and distal bone. The values of these stress tensor invariants were calculated using built-in evaluation options. Octahedral shear strain (γ_{oct}, OSS) correlated well with tissue type during fracture healing in rats [58], and so we calculated OSS from equivalent strain (ε_{vm}) using the following equation [59]:

$$\gamma_{oct} = \frac{\sqrt{2}}{3} \varepsilon_{vm} \tag{3.1}$$

Medial-lateral (ML), anterior-posterior (AP), and axial displacements were also evaluated to assess fracture motion in the osteotomy using built-in evaluation options (**Equation 3.2**). The median displacement ($\tilde{s}$) of the distal osteotomy surface nodes was subtracted from the median displacement of the proximal osteotomy surface nodes, and the initial length in all three dimensions was defined as the initial gap size (0.25 mm). A negative axial IFS represents compression, a negative medial-lateral IFS represents the proximal osteotomy surface translating further laterally than the distal osteotomy surface, and a negative anterior-posterior IFS represents the proximal osteotomy surface moving further posteriorly than the distal osteotomy surface. The total magnitude of IFS (combined IFS) was calculated using **Equation 3.3**.

$$IFS_{directional} = 100 * \frac{(\tilde{s}_{proximal} - \tilde{s}_{distal})}{0.25} \tag{3.2}$$

$$IFS_{combined} = 100 * \frac{\sqrt{\tilde{s}^2_{proximal,ML} + \tilde{s}^2_{proximal,AP} + \tilde{s}^2_{proximal,axial}} - \sqrt{\tilde{s}^2_{distal,ML} + \tilde{s}^2_{distal,AP} + \tilde{s}^2_{distall,axial}}}{0.25} \tag{3.3}$$

Finally, to better understand the strain vs. clearance trends, the final gap distances between the IMN and endosteal surface of the medullary canal were tabulated using the built-in contact tool option. The gap or distance between a bone element and an adjacent IMN element for the prescribed boundary conditions was recorded for each contact pair around the circumference of the nail. This was done along the length of the IMN (Z-location from -3.5 mm to 6 mm) at increments of 0.25 mm. The percent of IMN circumferential nodes in direct contact with the

surrounding bone (gap size = 0 mm) was calculated for each increment and plotted as a function of IMN length (proximal to distal end).

3.4   Results:

3.4.1 OSS in the fracture gap increases with reduced nail modulus and increased nail-bone clearance

For all of the simulations, the applied loading vector caused the proximal half of the femur to move primarily in the lateral direction, while the distal half of the femur was nearly motionless due to the fixation point on the distal surface (PEEK nail simulation shown in **Fig. 3.1(b)**). Depending on the nail-bone clearance (i.e., reaming diameter) and interlocking screw distance, switching from SS (high modulus) to PEEK (low modulus) resulted in a 1.74-4.07 fold change in median OSS within the granulation tissue (**Fig. 3.1(d)**). The largest median OSS within the granulation tissue was 24.7%, which occurred using a PEEK nail with 7.0 mm interlocking screw spacing and 0.1 mm nail-bone clearance. In contrast, the median OSS within the granulation tissue for the SS IMN did not exceed 8.7%, which occurred with 7.0 mm interlocking screw spacing and 0.06 mm nail-bone clearance.

OSS generally increased with increasing clearance between the nail and bone, but this strain versus clearance trend plateaued at smaller clearances in the SS IMN (between 0.02 mm and 0.06 mm) than in the PEEK IMN (between 0.06 mm and 0.1 mm). Switching the interlocking screw spacing from 3.5 mm to 7 mm resulted in 1.17-2.00 and 1.09-2.49 fold changes in median OSS within the granulation tissue for the PEEK and SS IMN simulations, respectively. However, the maximum absolute differences in OSS between these two interlocking screw spacings were 12.3% and 4.0% for the PEEK and SS IMN simulations, respectively. Furthermore, while this absolute difference in OSS widened with increasing clearance between bone and PEEK nail, the absolute difference in OSS between 3.5 mm and 7.0 mm interlocking screw spacing is less than 0.5% at both 0.0 mm and 0.1 mm SS IMN-bone clearance (**Fig. 3.1(d)**)
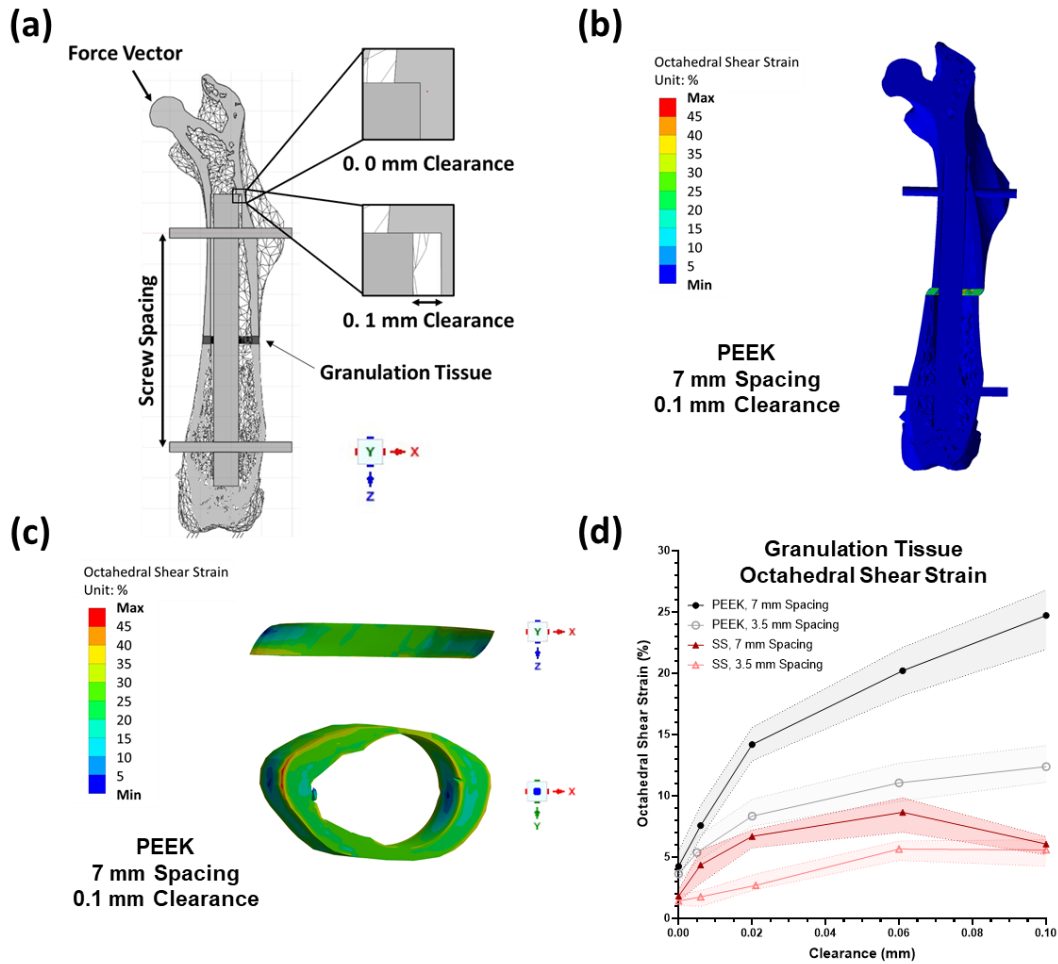
Fig 3.1. (a) A three-dimensional reconstruction of a 0.25 mm osteotomy fixed with an IMN with 7 mm interlocking screw spacing used to quantify the mechanical environments within the granulation tissue region, the nail, and the surrounding bone. Representative images of the OSS throughout the (b) entire geometry and (c) granulation tissue layer. (d) OSS within the granulation tissue (median ± IQR) generally increased with increasing nail-bone clearance but the effect of interlocking screw spacing was less consistent in the SS nail simulations.

3.4.2 Shear is the primary mode of strain in the fracture gap

Evaluating the individual strain components revealed that the maximum shear strain was larger than both the maximum principal strain and the absolute value of the minimum principal strain for all fixation strategies (**Fig. 3.2**). The absolute value of the minimum principal strain (i.e. compressive strain) exceeded the maximum principal strain (i.e. tensile strain) for the PEEK IMN simulations, but this trend in magnitude was less defined for the SS IMN simulations. Shear being the dominant mode of deformation within the granulation tissue can be explained by IFS typically being larger in the anterior-posterior and medial-lateral direction than in the axial direction (**Fig.**

3.3). IFS generally increased in all three orthogonal directions with increasing clearance between the nail and bone, but, similar to the OSS trend, IFS plateaued at smaller clearances in the SS IMNs than in the PEEK IMNs. These data indicate that bending of the IMN is limited for the prescribed boundary conditions with there being less bending in the stiffer SS IMN.
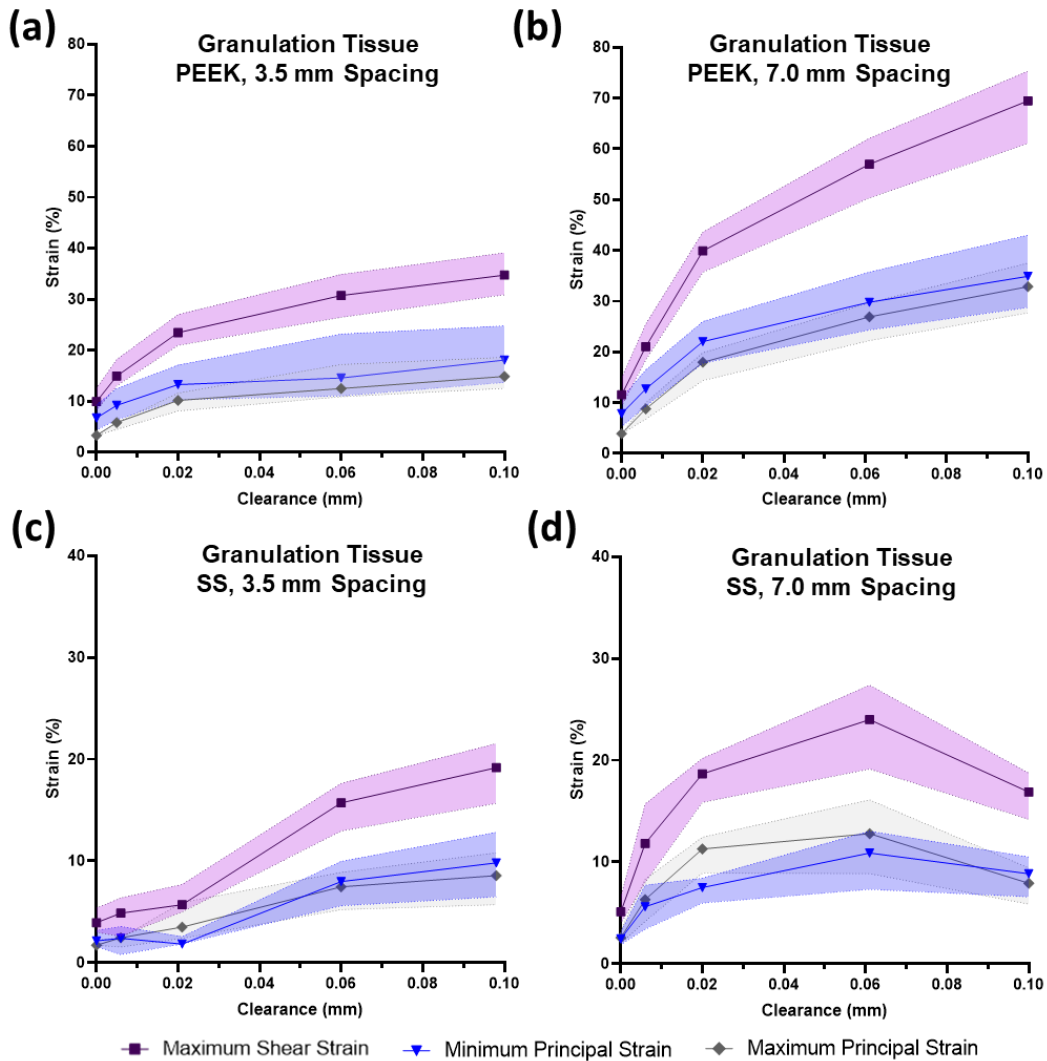
Fig 3.2. Maximum shear strain (median ± IQR) was the primary mode of strain within the granulation tissue when the osteotomy was fixed with (a) a PEEK IMN with 3.5 mm interlocking screw spacing, (b) a PEEK IMN with 7 mm interlocking screw spacing, (c) a SS IMN with 3.5 mm screw spacing, or (d) a SS IMN with 7 mm interlocking screw spacing
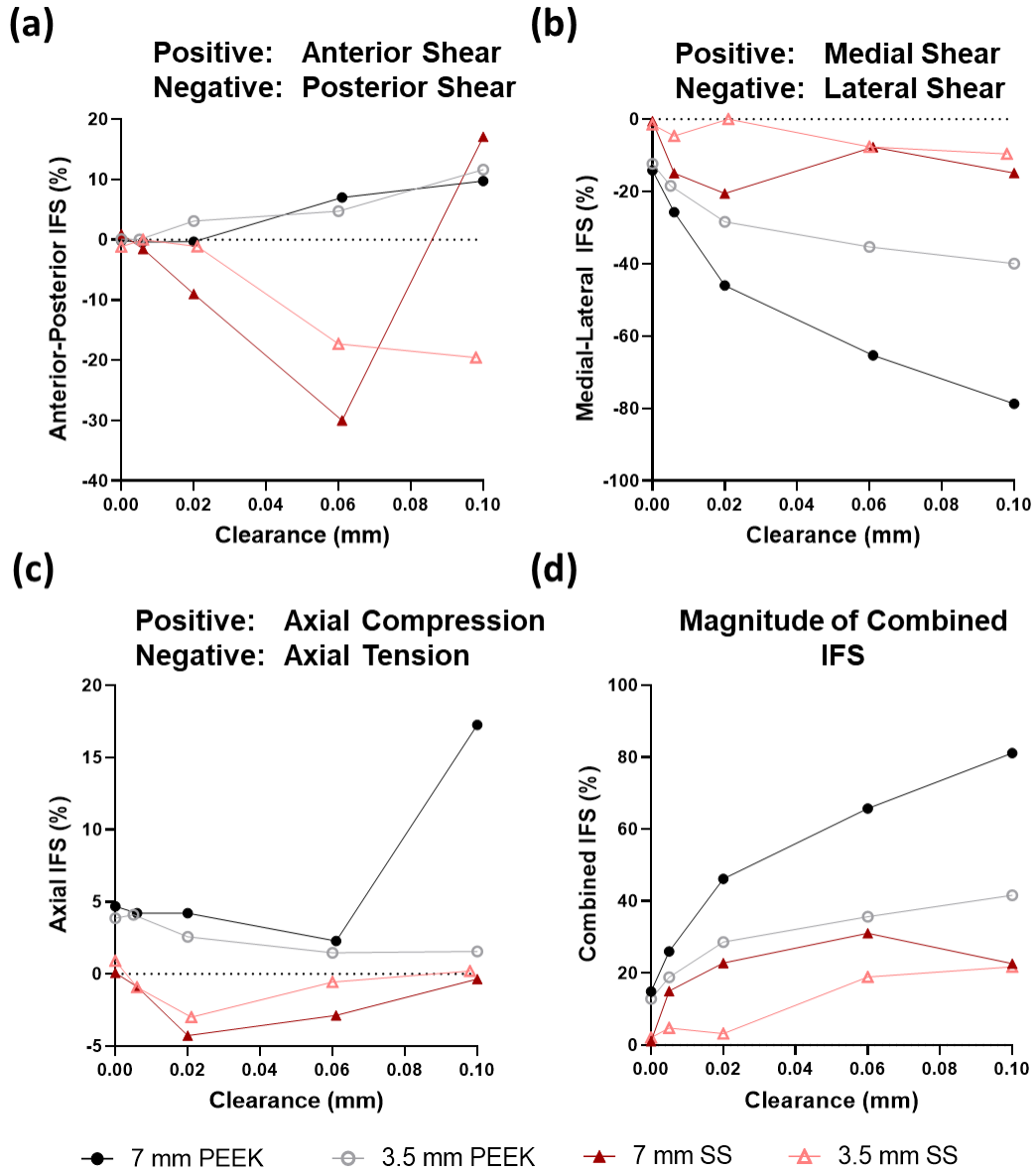
Fig. 3.3. IFS was typically greater in the anterior-posterior and medial-lateral directions than in the proximal-distal direction. (a) Fracture motion was in the posterior direction and in the anterior direction when the nail was SS and PEEK, respectively. One exception was the SS IMN with a spacing of 7 mm between screws and a clearance of 0.1 mm in that the motion of proximal surface switched to the anterior direction. (b) Regardless of spacing and material modulus, fracture motion was in the lateral direction such that medial-lateral IFS was higher for SS than for PEEK IMN. (c) SS IMN caused tensile IFS, while PEEK IMN caused compressive IFS. These strains were less than absolute 5%, except when there was a clearance of 0.1 mm between PEEK IMN and bone (7 mm spacing). (d) The change in the overall magnitude of IFS as clearance increased was similar to the change in OSS of the granulation tissue.

3.4.3 Stresses in the nail and bone are primarily below yield and endurance strengths

To anticipate whether any of the fixation constructs are likely to fail, equivalent (von Mises) stress was calculated for the IMNs and surrounding bone, and a factor of safety of 2.0 was applied to all relevant yield strengths (**Table 3.2**). The highest nail stresses were concentrated at the ends of the IMN and at the interlocking screws (**Supp. Fig. 3.1(a-d)** and **Supp. Fig. 3.2**), with fewer than 10% of nodes in the SS IMN predicted to exhibit equivalent stresses above the defined safety threshold for SS (**Supp. Fig. 3.1(e)**). In contrast, fewer than 0.04% of nodes in the PEEK nails were predicted to be exposed to equivalent stresses exceeding the designated threshold for PEEK (**Supp. Fig. 3.1(f)**). For most of the nail-bone clearances investigated, the nails with 7 mm interlocking screw spacing were predicted to contain more regions of high stress than the IMNs with 3.5 mm interlocking screw spacing. While the number of high-stress nodes decreased with increasing nail-bone clearance for the SS IMN with 7 mm interlocking screw spacing, the number of high-stress nodes for the SS nail with 3.5 mm interlocking screw spacing was projected to increase with increasing nail-bone clearance before reaching a maximum at a nail-bone clearance of 0.02 mm and decreasing rapidly with increasing nail-bone clearance. In contrast, the number of high stress nodes in the PEEK IMNs increased with increasing clearance.

Table 3.2. Yield and Safety Threshold Stresses of the Fixed Femur

Material	Yield Stress (MPa)	Safety Threshold (MPa)
Bone [60,61]	130	65
SS [62]	200	100
PEEK [62]	70	35

The equivalent stress within the surrounding bone was evaluated to identify regions of high-stress where damage could potentially accumulate. Representative images of the equivalent stress in the bone (**Supp. Fig. 3.3(a-b)**) showed that the regions of higher stress are located in the distal femur. The equivalent stress in the bone surrounding the PEEK IMN was lower than that in the bone surrounding the SS IMNs, and all of the nodes experiencing high levels of stress were located in the distal end of the bone-IMN assembly. The calculated equivalent stress values exceeded the safety threshold of bone in fewer than 0.25% and 4.5% of distal bone nodes in the PEEK and SS IMN simulations, respectively (**Supp. Fig. 3.3(c-d)**). In the SS IMN simulations, the percent

of high-stress nodes generally decreased with increasing nail-bone clearance, and the bone surrounding the nail with the 7 mm interlocking screw spacing was exposed to higher stresses than the bone surrounding the nail with the 3.5 mm interlocking screw spacing. In contrast, the percent of high-stress nodes in the bone surrounding the PEEK IMN remained relatively low for all nail-bone clearances investigated. In all of the simulations, the majority of nodes that were subjected to high levels of equivalent stress were concentrated at the interlocking screw, at the bottom of the nail, and at the fixation point (**Supp. Fig. 3.4**).

3.4.4 Thinner SS IMNs with 7.0 mm interlocking screw spacing can provide higher levels of IFS while IFS remains unchanged for nails with 3.5 mm interlocking screw spacing

The initial set of FE models predicted that the OSS maintained by the commercially available SS IMN would not exceed 8.7% within the osteotomy and would be similar between the 3.5 mm and 7 mm interlocking screw spacing options when the reaming-nail distance (i.e., gap size) is 0.0 mm or 0.1 mm (**Fig. 3.1(d)**). To determine whether it would be possible for rigid SS IMNs to produce levels of IFS comparable to those produced by the compliant PEEK IMNs, the diameter and, therefore, stiffness of the original SS IMN was reduced while maintaining a nail-bone clearance of 0.1 mm. The thinner SS IMN simulations with 3.5 mm interlocking screw spacing predicted a median OSS within the osteotomy around 6.3% for all diameters investigated. In the thinner SS IMN simulations with 7.0 mm screw spacing, once the nail diameter was reduced below 0.74 mm, the median OSS in the osteotomy increased with decreasing nail size until it reached a maximum value of 10.5% for a 0.62 mm diameter SS IMN (**Fig. 3.4(a)**). Similar to the original diameter IMN simulations, shear was the prevailing mode of strain (data not shown).

Fewer than 0.3% of nodes in the thinner SS IMNs were predicted to be exposed to equivalent stresses greater than the defined safety threshold of SS; and, for all nail diameters, more nodes in the 7 mm interlocking screw spacing models experienced these high stresses than in the 3.5 mm interlocking screw spacing models (**Fig. 3.4(b)**). As the diameter of the SS nail decreased, the percent of nodes in the IMN that exceed the safety threshold was predicted to increase (**Fig. 3.4(b)**). In contrast, the surrounding bone generally contained fewer high-stress

nodes with decreasing IMN thickness (**Fig. 3.4(c)**). The thinner SS IMNs with 7 mm interlocking screw spacing

generated more regions of high-stress in the distal bone than those with 3.5 mm screw spacing, but fewer than

0.25% of nodes in the bone were exposed to equivalent stresses greater than the safety threshold. Analogous to the

original SS IMN simulations, higher stresses were concentrated near the interlocking screws, the ends of the nail,

and the distal bone fixation site (**Supp. Fig. 3.5**).
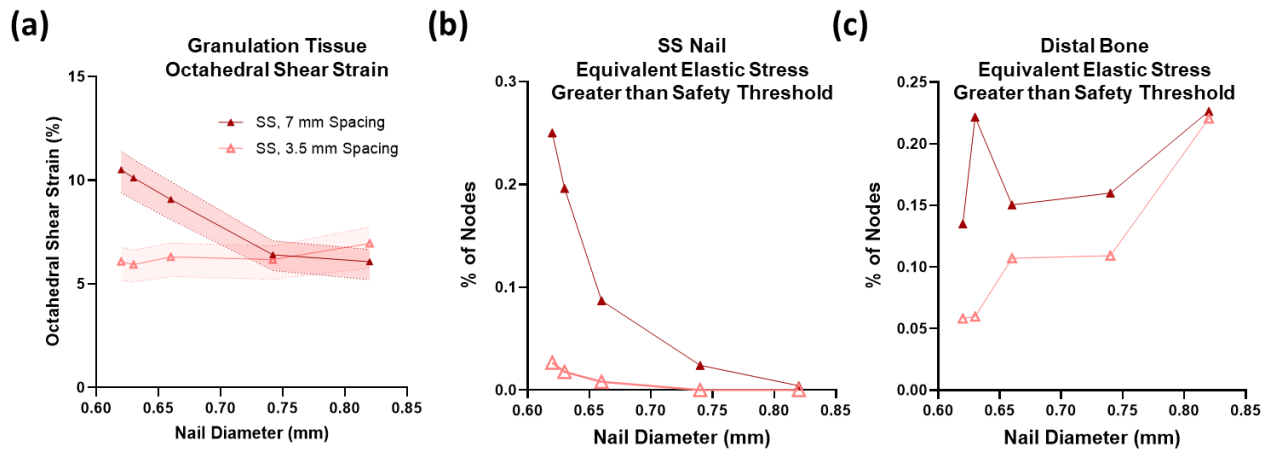
Fig 3.4. (a) The OSS within the granulation tissue (median ± IQR) only increased with decreasing SS IMN diameter when the interlocking screw spacing was set to 7 mm. (b) The percent of nodes in the thinner SS IMN exceeding the defined safety threshold of SS (100 MPa) decreased with increasing nail diameter but remained relatively low compared to the majority of the original thickness SS IMN simulations (**Supp. Fig. 3.1(e)**). (d) The percent of nodes in the distal bone, surrounding the thinner SS IMN, exceeding the defined safety threshold of bone (65 MPa) generally increased with increasing nail diameter but remained relatively low compared to the majority of the original thickness SS IMN simulations (**Supp. Fig. 3.3(d)**).

3.5   Discussion:

Clinically relevant murine models can be beneficial for investigating the interplay between fracture

biology and biomechanics, because such models can investigate how healing capacity (biology) and mechanical

stimulation (rigidity of fixation) work in concert during fracture repair. However, there is currently only one locking

IMN construct commercially available for use in mice [33], thereby restricting the capability for modulating the

mechanical environment to variable osteotomy size or fracture gap [53]. The purpose of this study was to use a

simplified FE model to evaluate the effects of the nail material, interlocking screw spacing, and nail-bone clearance

on IFS early in the fracture repair process. Together, these results can be utilized to identify which parameters

should be considered when selecting alternative IMN constructs for future *in vivo* studies. This study demonstrated that switching the IMN material from SS to PEEK consistently resulted in a large increase in IFS (i.e., octahedral strain within the osteotomy or fracture motion per gap size). In contrast, changing interlocking screw spacing had limited impact on IFS when the osteotomy was fixed with a rigid SS nail. Unless a smaller diameter, rigid nail can be manufactured and shown to survive normal loading conditions, using nails with variable modulus (rigid to compliant) provides the greatest manipulation of IFS when compared to other parameters (spacing of interlocking screws and reaming clearance).

Interestingly, while an increase in the clearance between the IMN and endosteal bone surface also increased IFS, the increase in IFS plateaued with the stiffer IMN; thus limiting the range in IFS that could be achieved by reaming compared to the compliant PEEK nail. The plateauing observed in the stiffer nail is potentially caused by the IM nail no longer making contact with the surrounding bone after loading (**Supp. Fig. 3.6**). The SS nail with 3.5 mm interlocking screw spacing lost contact with the mid-diaphysis between 0.005 mm and 0.02 mm clearance while the SS nail with 7 mm interlocking screw spacing and the PEEK nail with 3.5 mm interlocking screw spacing both lost contact with the mid-diaphysis between 0.06 mm and 0.1 mm clearance. The PEEK nail with 7 mm interlocking screw spacing remained in contact with the mid-diaphysis for all nail-bone clearances.

IMNs have been utilized clinically for decades to fix long bone fractures. While conventional IMNs are typically fabricated from SS or titanium-based alloys, more compliant PEEK-based nails have begun to show some clinical success in permitting early weight-bearing and promoting accelerated fracture healing [63–65]. The simulations herein predicted that a 0.82 mm diameter IMN, fabricated from SS, can produce median OSS between 1.4 % and 8.7 % within a 0.25 mm osteotomy in a murine femur. These strains will likely engender a similar secondary fracture repair response to that observed *in vivo* with the commercially available SS nail [33]. However, while strains below 2% and 10% are thought to promote primary fracture repair and secondary fracture repair, respectively, in humans with minimal vascular injury [66,67], both bone and cartilage can potentially withstand strains up to 30% in murine fracture models [48,55]. As predicted by the FE models, a PEEK nail with 7.0 mm interlocking screw spacing can be used to access the upper portion of this strain range while a SS nail can be used to engender median OSS less than 10% within the osteotomy. Therefore, having access to both a rigid (e.g., SS) and compliant (e.g., PEEK) IMN

with 7.0 mm interlocking screw spacing for use in a murine femoral fracture model would facilitate clinically relevant studies investigating the role of the mechanical environment in fracture healing.

To determine whether other SS IMN design parameters can be modified to provide similar levels of IFS to those produced by the PEEK nails, we wanted to investigate the impact of reducing the stiffness of SS nail. Considering that bending stiffness is proportional to diameter of the IMN [20,68], the diameter of the SS nail was systematically reduced to 0.62 mm while maintaining a constant nail-bone clearance. The thinner SS nail simulations predicted that reducing the diameter of the nail has minimal impact on the mechanical environment supported by the SS nail with 3.5 mm interlocking screw spacing while IFS increases with decreasing nail diameter for the SS nail with 7.0 mm interlocking screw spacing once the diameter falls below 0.74 mm. Furthermore, a median OSS greater than 10% within the osteotomy can be produced by SS nails with diameters less than or equal to 0.63 mm. However, it is unknown whether a smaller diameter SS IMN can be manufactured and whether it will withstand in vivo cyclic loading without yielding or failing. Moreover, the IFS engendered by using the thinner SS IMN remain well below those generated by the PEEK nail with 7.0 mm interlocking screw spacing. Therefore, a PEEK nail with 7.0 mm interlocking screw spacing will be more effective than a thinner SS nail at providing a high strain environment within a transverse osteotomy.

The FE models in this study also predicted that for the loading condition investigated, shear strain would exceed compressive and tensile strain for all of the nails investigated and that IFS would generally increase with increasing nail-bone clearance. These results are in agreement with other *ex vivo* and *in silico* studies that reported shear to be the primary mode of motion supplied by IMNs [69,70], and that increasing the diameter of the IMN or minimizing the annular gap between the nail and endosteal surface reduces interfragmentary motion [53,69]. While some studies have demonstrated that shear strain hinders fracture healing [71,72], others have concluded that shear strain may not be detrimental [73,74]. These conflicting conclusions are likely due in part to IMNs supporting both shear and axial strain [36]. Shear strain was the dominant mode of strain in our simulations, but compressive and tensile strains also existed within the granulation tissue region. The effects of these strain modes and the timing of their application must be investigated further to optimize healing in patients with compromised biological potential

While IMNs can fatigue and break in patients experiencing delayed healing or nonunion [75], immediate failure of the nail was not predicted in any of the simulated IMN constructs examined in this study. For almost all of the nail-bone clearances investigated, the largest percent of nodes supporting high stresses were observed in the original SS IMN construct. While this study only examines the mechanical environment shortly after creating the osteotomy, RI System's SS MouseNail, from which the original SS nail is designed, has demonstrated the ability to maintain fixation over 10 weeks, even in the case of non-union [34]. While it is currently unknown whether the higher OSS predicted for the osteotomies fixed with the PEEK and thinner SS IMNs can potentially alter fracture healing in vivo, the prediction that they will have smaller regions of high stress in the nails and in the surrounding bone suggest that these fixation strategies are less likely than the original SS nail to fail. These results are in agreement with prior clinical reports suggesting that clinically available PEEK nails can share more of the mechanical load with the fracture callus and surrounding bone than SS nails and are, therefore, less likely to fail [76,77].

These FE simulations contend that a PEEK-based IMN or a smaller diameter SS nail can potentially be used in a clinically relevant murine model for investigating the effects of increased IFS on fracture repair, but this study has a number of limitations. To allow movement between the between the nail and interlocking screws [78], a coefficient of friction of 0.2 was applied. This coefficient of friction has been used in similar FE studies [52,53], but it is unclear whether the amount of micromotion between the two bodies calculated in the simulations will match what will be seen *in vivo*. Furthermore, even though the loading conditions used in these simulations have been used in previous studies [55,56], it is not currently known whether these forces accurately recapitulate the gait forces observed early in the fracture healing process. To investigate whether the strain vs. nail-bone clearance trend (**Fig. 3.1(d)**) and the strain mode differences (**Fig. 3.2(b)**) observed in this study were dependent on the selected boundary conditions (**Fig. 3.1(a)**), the simulations of the PEEK nail with 3.5 and 7 mm interlocking screw spacing simulations were reanalyzed to include both a hip-joint reaction force and an abductor muscle force (**Supp. Fig. 3.9 (a)**) instead of the sole hip-joint reaction force that caused an axial gait force of 6 x BW and a bending moment of 10.7 x BW at the mid-diaphysis in the original simulations (**Fig. 3.1 (a)**). Due to insufficient information about abductor forces in mice, we adopted the two force vectors from FE models of the human femur in singled-legged stance [79–83], and

scaled them by mouse body weight. In agreement with the original simulations, all the strain modes investigated increased with increasing nail-bone clearance (**Supp. Fig. 3.9 (d-f)**). Even though the reduced lateral loading reduced medial-lateral IFS in these simulations (**Supp. Fig. 3.9 (b-c)**) relative to the original simulations (**Fig. 3.1 (b-c)**), maximum shear strain continued to exceed the maximum and minimum principal strains (**Supp. Fig. 3.9 (e-f)**).

Another limitation in the parametric study was the fixation of both the medial and lateral condyles (**Fig. 3.1(a)**). In FE models of human femurs with an IMN subject to single-legged stance, a point in the medial condyle was fixed in the three orthogonal directions, thereby allowing rotation of the distal end in the coronal plane and sagittal plane [42,84,85]. By preventing movement of both condyles, the present model favors higher stresses in the distal bone than these previous studies. Building the FE model from a scan of a single mouse femur also limits the generalizability of the observed trends, and we predict that IFS values would likely increase as the femur elongates with age. Finally, while mesh convergence testing was performed on the granulation tissue region (**Supp. Fig. 3.7**), the FE models herein were not validated with *ex vivo* mechanical testing. Consequently, the calculated IFS values may be imprecise. However, we conducted an intact bone simulation, using the same loading vector and fixation point, and calculated median maximum and minimum principal strains of 58 microstrain and 126 microstrain, respectively, along the external surface of the mid-diaphysis of the femur (**Supp. Fig. 3.7**). These strains are comparable to other *in silico* studies that have quantified mid-diaphyseal strains in murine tibiae during gait [86,87]. While confirming IFS accuracy will require model validation [88], relative comparisons can still be made between the different fixation groups.

An additional limitation of this study is that clearance between the nail and bone was created by digital reaming. While this process maintained the diameter and, therefore, stiffness of the nail, orthopedic reaming is often coupled with larger nail implantation to increase contact between the IMN and cortical bone and to improve the stiffness of the entire construct [20]. Reaming can also damage the endosteal blood supply [66,89], but studies have shown that the blood supply from the periosteum and surrounding soft tissue can compensate for this loss. While minimal reaming is required for MouseNail implantation [34] and 0.5-1.5 mm over-reaming is appropriate for IMN

implantation in humans [90], it is currently unknown whether nail-bone interference will make it more difficult to implant the compliant PEEK IMN or whether additional reaming will be required.

A further limitation is that the FE model geometry of a transverse osteotomy only includes a layer of granulation tissue between the bone cortices rather than a mature callus. This substitution was performed to simplify the simulations, and including more granulation tissue to the model is not expected to significantly affect the IFS trends due to the tissue's relatively low elastic modulus. However, while transverse osteotomies are more consistent regarding size and location than closed fractures created by three-point bending, the creation of these defects induces soft tissue trauma and inflammation. Furthermore, while transverse osteotomies commonly occur in surgical practice, they do not completely mimic traumatic fractures [91].

Finally, while other *in silico* studies have included other contributing variables, including hydrostatic stress, fluid flow, cellular infiltration, vascularization, oxygen concentration, and growth factors [35–38,92–95], this study only focusses on identifying how IMN design parameters affect IFS early in the fracture healing process. While all of these variables likely influence fracture repair, deformation has been shown to have a larger impact than hydrostatic pressure or fluid flow on the initial healing patterns in sheep [96], and OSS correlated well with tissue type during fracture healing in rats [58]. Nonetheless, the simulations herein can be used to identify relative IFS trends, but they cannot be used to predict healing patterns. The transient nature of fracture repair must also be considered when proposing new therapeutic strategies, because the mechanical environment can promote or hinder healing at any stage of the healing process [97–99]. Despite these limitations, the FE models herein indicate that PEEK IMNs or thinner SS nails can be used to support levels of IFS greater than what is provided by the commercially available SS IMN.

3.6   Conclusions:

This proof-of-concept FE modeling study investigated which locking IMN design components have the largest impact on the initial IFS in a murine transverse femur osteotomy model. The FE simulations revealed that IFS generally increases with increasing nail-bone clearance and with decreasing nail modulus. In contrast, while IFS is predicted to increase with increasing interlocking screw spacing for the PEEK IMNs and for SS IMNs with

diameters less than 0.74 mm, interlocking screw spacing is projected to have less of an impact on IFS when the original-diameter SS IMN is used. These findings suggest that a compliant PEEK IMN with 7.0 mm interlocking screw spacing can be used alongside a commercially available SS IMN in future *in vivo* studies to investigate how biological mechanisms and mechanical stimuli affect fracture healing and non-union in mice.

Supplemental Figures:
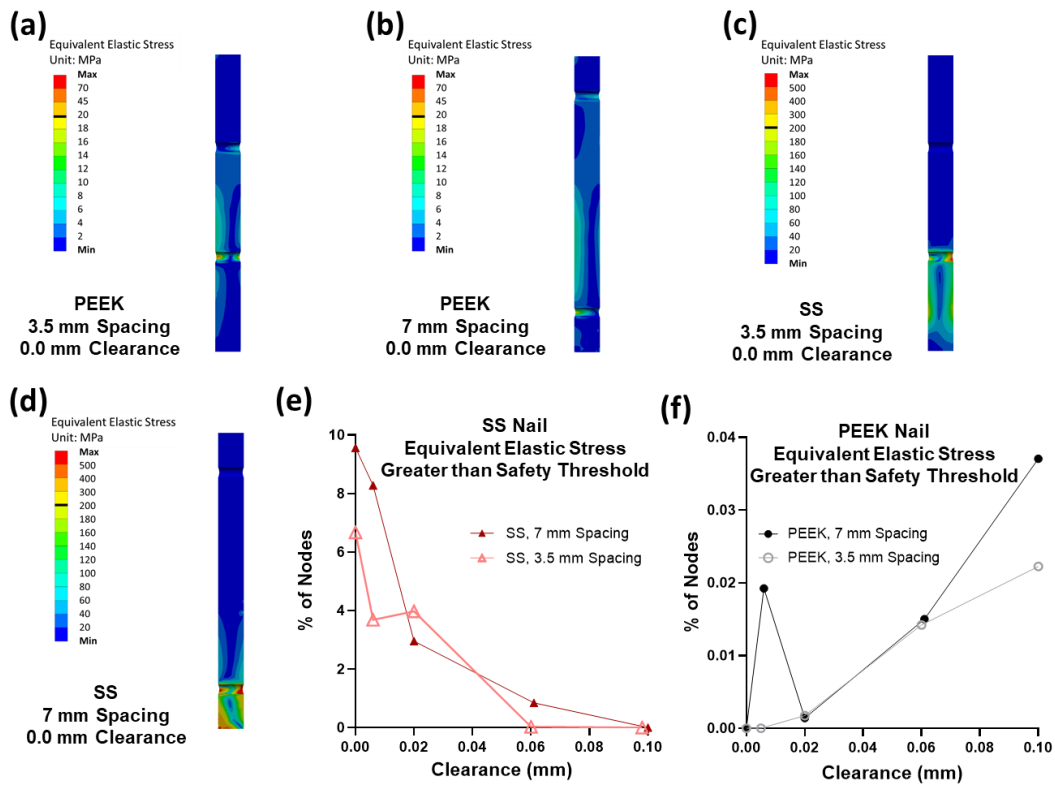
Supp. Fig. 3.1. Representative images of the equivalent elastic stress (von Mises stress) in (a) a PEEK IMN with 3.5 mm interlocking screw spacing, (b) a PEEK IMN with 7 mm interlocking screw spacing, (c) a SS IMN with 3.5 mm screw spacing, or (d) a SS IMN with 7 mm interlocking screw spacing. (e) The percent of nodes in the SS nails exceeding the defined safety threshold of SS (100 MPa) generally decreased with increasing nail-bone clearance. (f) The percent of nodes in the PEEK IMN exceeding the defined safety threshold of PEEK (35 MPa) generally increased with increasing nail-bone clearance, but the percent of nodes exceeding this threshold was low regardless of nail-bone clearance.
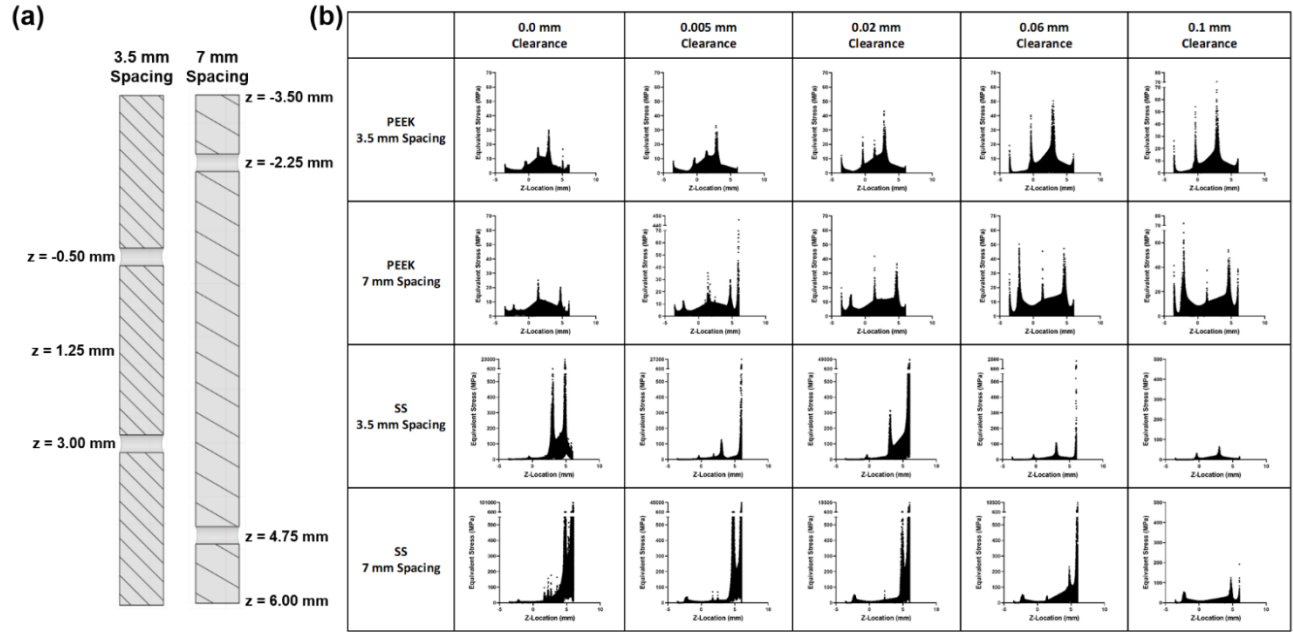
Supp. Fig. 3.2. (a) Proximal-distal positions of the IMN and interlocking screws. (b) The highest levels of equivalent stress in the IMN were concentrated at the ends of the nail and the interlocking screws for all constructs investigated.
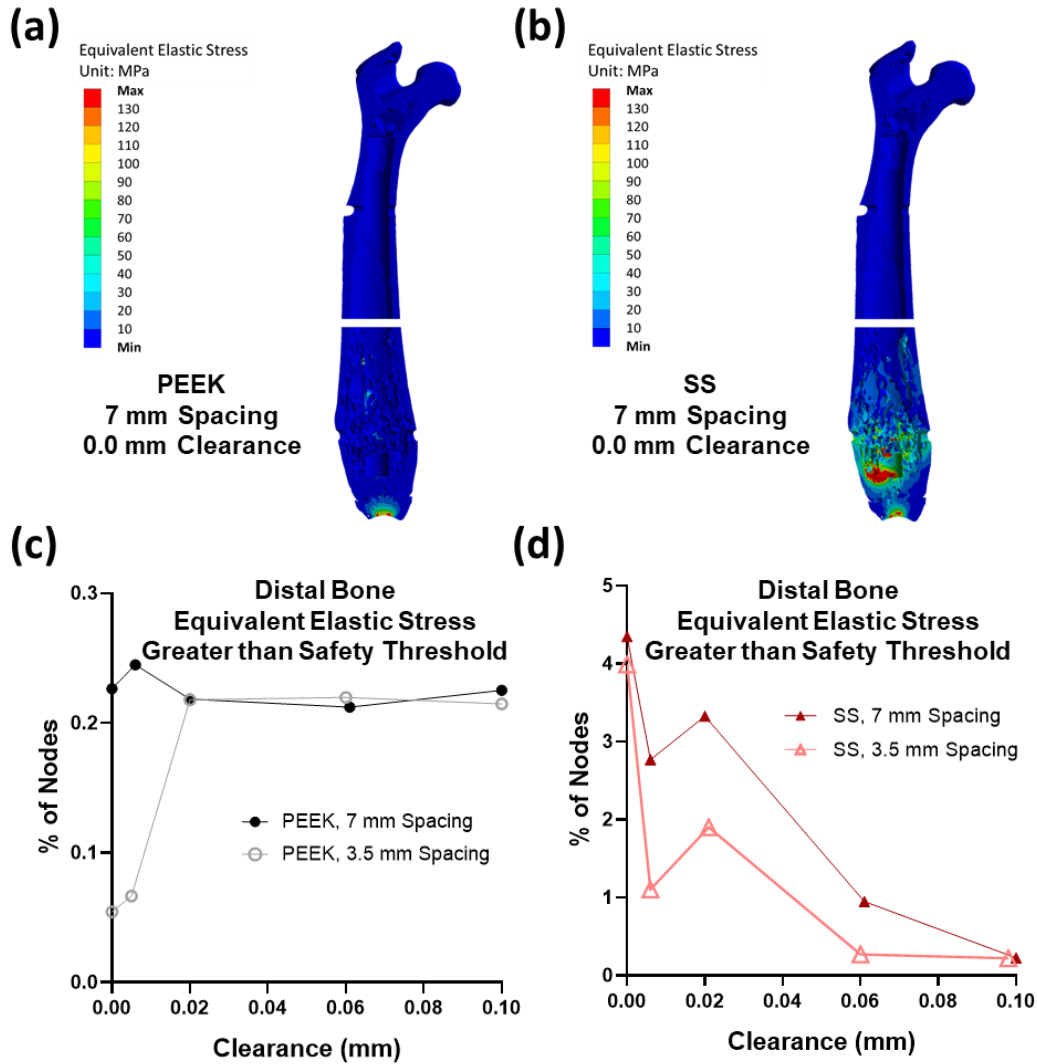
Supp. Fig. 3.3. Representative images of the equivalent stress in the bone surrounding (a) SS and (b) PEEK IMNs demonstrated that regions of higher stress were concentrated in the distal bone. (c) The percent of distal bone nodes, surrounding the PEEK IMNs, exposed to equivalent stresses greater than the defined safety threshold of bone (65 MPa), remained relatively low for all nail-bone clearances investigated. (d) The percent of distal bone nodes, surrounding the SS IMNs, exposed to equivalent stresses greater than the defined safety threshold of bone (65 MPa), generally decreased with increasing nail-bone clearances investigated. More distal bone nodes were exposed to high levels of equivalent stress in the 7 mm interlocking screw spacing simulations than in the 3.5 mm interlocking screw spacing simulations.
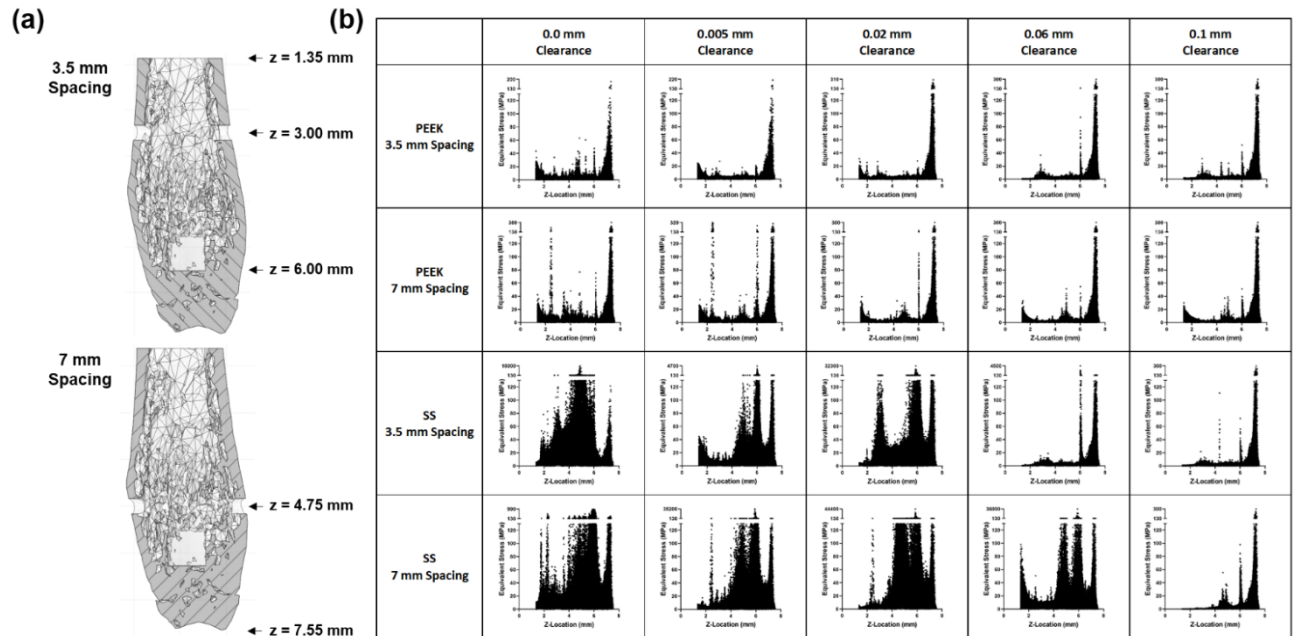
Supp. Fig. 3.4 (a) Proximal-distal positions of interlocking screws, nail edge, and fixation point. (b) The highest levels of equivalent stress in the distal bone were concentrated at the interlocking screw, end of the nail, and fixation point for all of the PEEK and SS IMN constructs investigated.

	0.62 mm Diameter	0.63 mm Diameter	0.66 mm Diameter	0.74 mm Diameter	0.82 mm Diameter
SS 3.5 mm Spacing Nail					
SS 3.5 mm Spacing Bone					
SS 7 mm Spacing Nail					
SS 7 mm Spacing Bone					
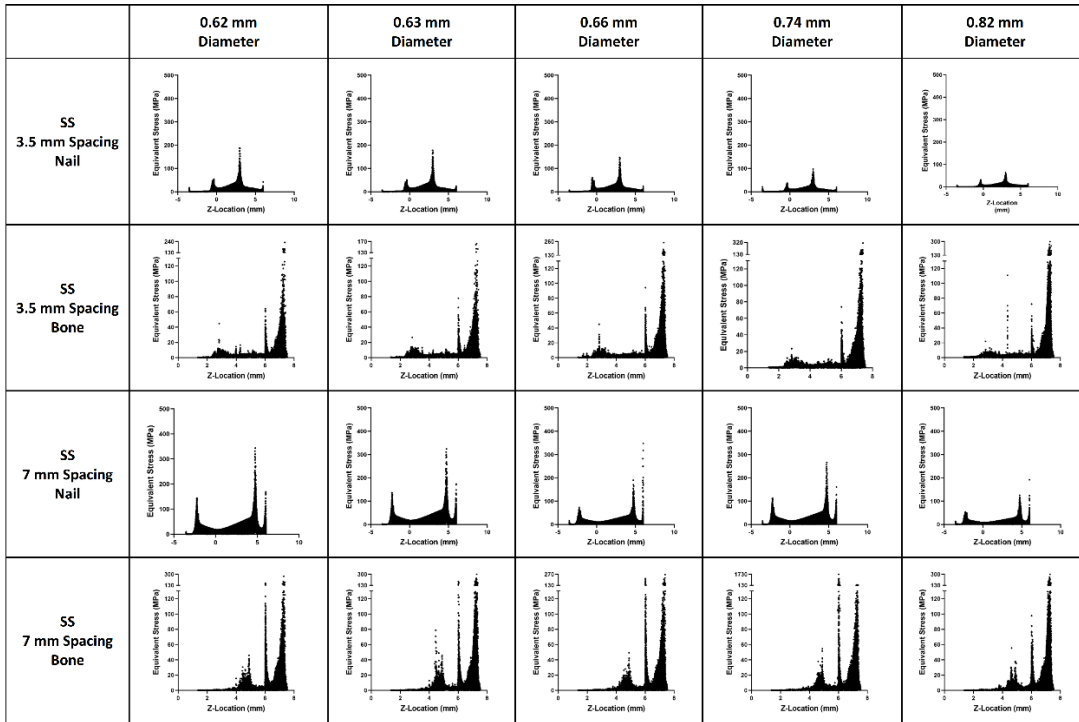
Supp. Fig. 3.5. The highest levels of equivalent stress in the IMN were concentrated at the ends of the nail and interlocking screws while the highest levels of equivalent stress in the distal bone were concentrated at the interlocking screw, end of the nail, and fixation point.
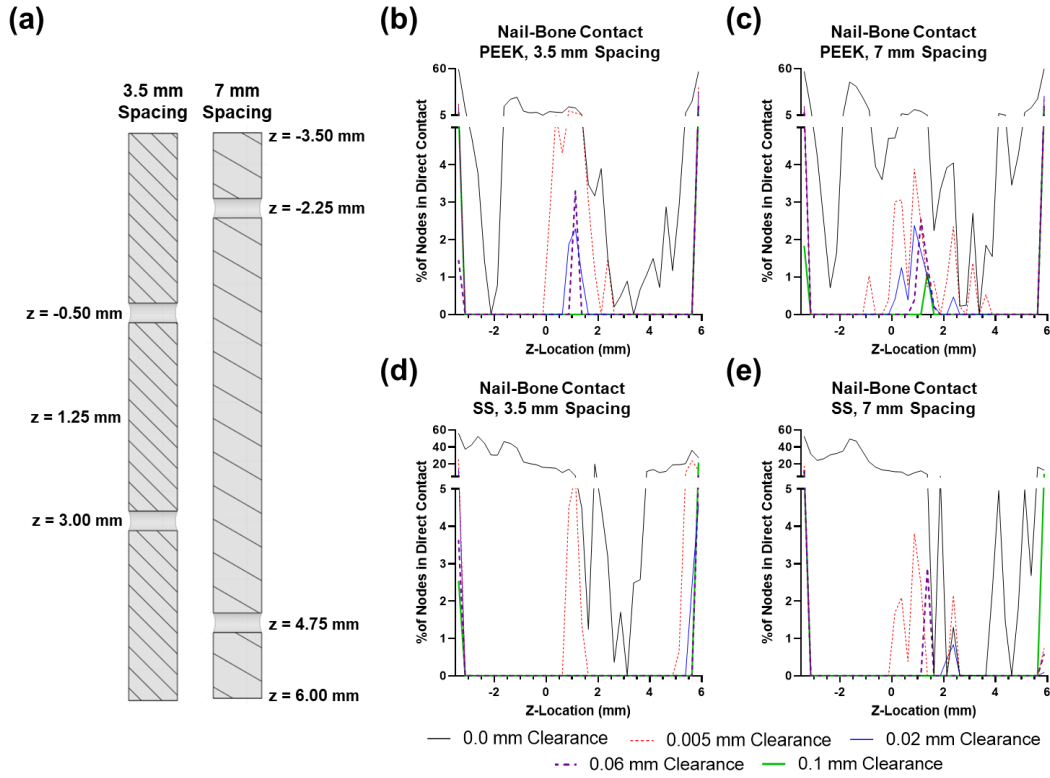
Supp. Fig. 3.6. (a) Proximal-distal positions of the IMN and interlocking screws. The percent of nail-bone contact pair nodes in direct contact (0 mm gap) for the (b) a PEEK IMN with 3.5 mm interlocking screw spacing, (c) a PEEK IMN with 7 mm interlocking screw spacing, (d) a SS IMN with 3.5 mm screw spacing, or (e) a SS IMN with 7 mm interlocking screw spacing. The stiffer SS IMNs lose contact with the mid-diaphysis at smaller nail-bone clearances than the more compliant PEEK IMNs.
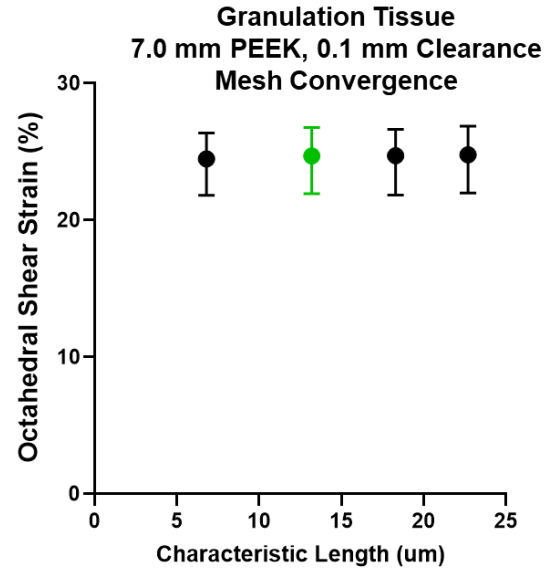
Supp. Fig. 3.7. Mesh convergence testing revealed that changing characteristic length of the granulation tissue elements minimally impacted the OSS in the granulation tissue for the 7.0 mm PEEK simulation with 0.1 mm nail-bone clearance. The characteristic length of the granulation tissue elements was varied between 6.8 and 22.7 µm while the mesh sizes for the bone, nail, and interlocking screws remained constant. A characteristic length of 13.2 µm (green) was chosen for all simulations contained herein.
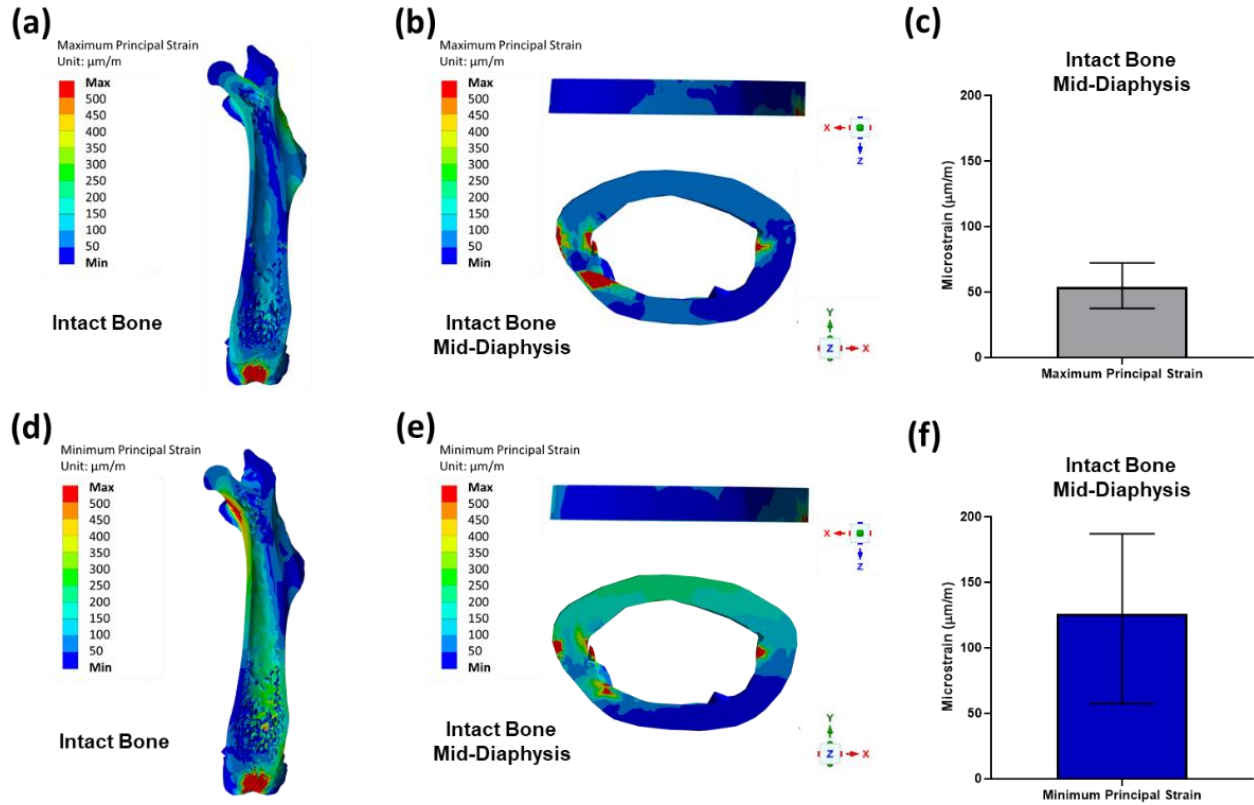
Supp. Fig. 3.8. Representative images of the maximum principal strain in (a) an intact bone or (b) along the mid-diaphyseal bone surface and of the minimum principal strain in (d) an intact bone or (e) along the mid-diaphyseal bone surface. (c) The maximum principal strain and (f) minimum principal strain distributions (median ± IQR) revealed the median maximum and minimum principal strains to be 58 microstrain and 126 microstrain, respectively, along the mid-diaphyseal bone surface.
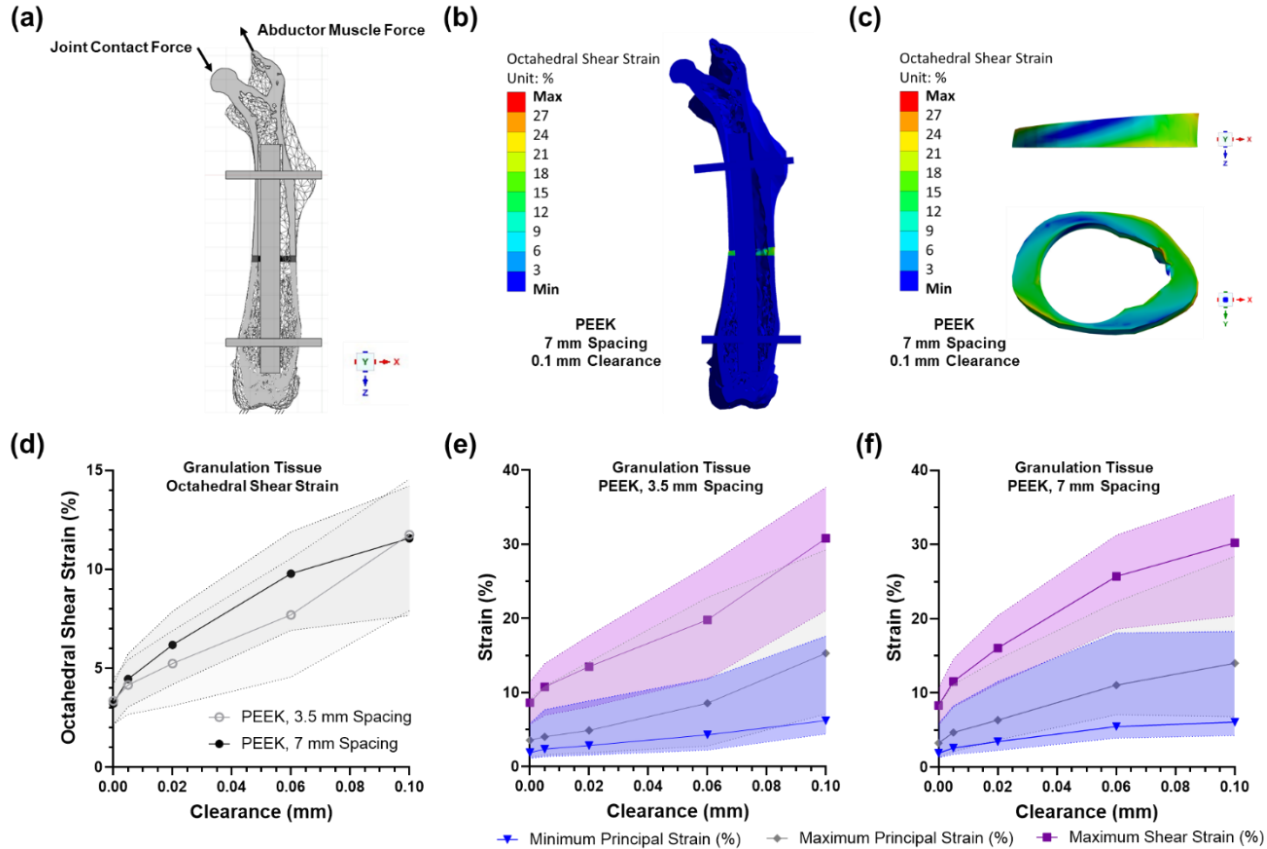
Supp. Fig. 3.9. (a) A three-dimensional reconstruction of a 0.25 mm osteotomy fixed with an IMN with 7 mm interlocking screw spacing used to quantify the mechanical environments within the granulation tissue region for single-legged stance loading conditions. The force vectors for the hip-joint contact force and the abductor muscle force were 0.14 N, 0.08 N, 0.61 N, and -0.11 N, 0.00 N, -0.27 N (lateral, anterior, distal), respectively. Representative images of the OSS throughout the (b) entire model and (c) granulation tissue layer after loading. (d) In agreement with the original simulations, OSS within the granulation tissue (median ± IQR) increased with increasing nail-bone clearance. Maximum shear strain (median ± IQR) continued to be the primary mode of strain within the granulation tissue when the osteotomy was fixed with (e) a PEEK IMN with 3.5 mm interlocking screw spacing and (f) a PEEK IMN with 7 mm interlocking screw spacing.

References:

1. Watkins-Castillo, S. & Andersson, G. *United States Bone and Joint Initiative: The Burden of Musculoskeletal Diseases in the United States (BMUS). The Burden of Musculoskeletal diseases int he United States* (2014).
2. Hak, D. J. *et al.* Delayed union and nonunions: Epidemiology, clinical issues, and financial aspects. *Injury* **45**, S3–S7 (2014).
3. Mills, L. A., Aitken, S. A. & Simpson, A. H. R. W. The risk of non-union per fracture: current myths and revised figures from a population of over 4 million adults. *Acta Orthopaedica* **88**, 434–439 (2017).
4. Zura, R. *et al.* Epidemiology of fracture nonunion in 18 human bones. *JAMA Surg.* **151**, 1–12 (2016).
5. Claes, L., Recknagel, S. & Ignatius, A. Fracture healing under healthy and inflammatory conditions. *Nat. Rev. Rheumatol.* **8**, 133–143 (2012).
6. Gaston, M. S. & Simpson, A. H. R. W. Inhibition of fracture healing. *J. Bone Jt. Surg. - Ser. B* **89**, 1553–1560 (2007).
7. Haffner-Luntzer, M., Liedert, A. & Ignatius, A. Mechanobiology of bone remodeling and fracture healing in the aged organism. *Innov. Surg. Sci.* **1**, 57–63 (2016).
8. Bhandari, M. *et al.* Predictors of reoperation following operative management of fractures of the tibial shaft. *J. Orthop. Trauma* **17**, 353–361 (2003).
9. Elliott, D. S. *et al.* A unified theory of bone healing and nonunion. *Bone Jt. J.* **98B**, 884–891 (2016).
10. Perren, S. M., Fernandez, A. & Regazzoni, P. Understanding fracture healing biomechanics based on the "strain" concept and its clinical applications. *Acta Chir. Orthop. Traumatol. Cech.* (2015).
11. Kostenuik, P. & Mirza, F. M. Fracture healing physiology and the quest for therapies for delayed healing and nonunion. *J. Orthop. Res.* **35**, 213–223 (2017).
12. Thompson, E. M., Matsiko, A., Kelly, D. J., Gleeson, J. P. & O'Brien, F. J. An Endochondral Ossification-Based Approach to Bone Repair: Chondrogenically Primed Mesenchymal Stem Cell-Laden Scaffolds Support Greater Repair of Critical-Sized Cranial Defects Than Osteogenically Stimulated Constructs In Vivo. *Tissue Eng. Part A* **22**, 556–567 (2016).
13. Wang, W. & Yeung, K. W. K. Bone grafts and biomaterials substitutes for bone defect repair: A review. *Bioact. Mater.* **2**, 224–247 (2017).
14. Epari, D. R., Wehner, T., Ignatius, A., Schuetz, M. A. & Claes, L. E. A case for optimising fracture healing through inverse dynamization. *Med. Hypotheses* **81**, 225–227 (2013).
15. Ferreira, N., Marais, L. C. & Aldous, C. Mechanobiology in the management of mobile atrophic and oligotrophic tibial nonunions. *J. Orthop.* **12**, S182–S187 (2015).
16. Glatt, V., Evans, C. H. & Tetsworth, K. A concert between biology and biomechanics: The influence of the mechanical environment on bone healing. *Front. Physiol.* **7**, 1–18 (2017).
17. Beltran, M. J., Collinge, C. A. & Gardner, M. J. Stress Modulation of Fracture Fixation Implants. *J. Am. Acad. Orthop. Surg.* **24**, 711–719 (2016).
18. Kubiak, E. N., Beebe, M. J., North, K., Hitchcock, R. & Potter, M. Q. Early Weight Bearing After Lower Extremity Fractures in Adults. *J. Am. Acad. Orthop. Surg.* **21**, 727–738 (2013).
19. Wood, G. W. Intramedullary nailing of femoral and tibial shaft fractures. in *Journal of Orthopaedic Science* (2006). doi:10.1007/s00776-006-1061-6
20. Rosa, N. *et al.* Intramedullary nailing biomechanics: Evolution and challenges. *Proc. Inst. Mech. Eng. Part H J. Eng. Med.* **233**, 295–308 (2019).
21. Betts, D. C. & Müller, R. Mechanical regulation of bone regeneration: Theories, models, and experiments. *Front. Endocrinol. (Lausanne).* **5**, 1–14 (2014).
22. Hente, R. & Perren, S. M. Mechanical Stimulation of Fracture Healing – Stimulation of Callus by Improved Recovery. 385–391 (2019).
23. Yuasa, M. *et al.* The Size of Intramedullary Fixation Affects Endochondral-Mediated Angiogenesis during Fracture Repair. *J. Orthop. Trauma* **33**, e385–e393 (2019).
24. Dallas, S. L., Xie, Y., Shiflett, L. A. & Ueki, Y. Mouse Cre Models for the Study of Bone Diseases. *Curr. Osteoporos. Rep.* **16**, 466–477 (2018).

25. Elefteriou, F. & Yang, X. Genetic mouse models for bone studies-Strengths and limitations. *Bone* **49**, 1242–1254 (2011).

26. Garcia, P. *et al.* Rodent animal models of delayed bone healing and non-union formation: A comprehensive review. *Eur. Cells Mater.* **26**, 1–14 (2013).

27. Histing, T. *et al.* Small animal bone healing models: Standards, tips, and pitfalls results of a consensus meeting. *Bone* **49**, 591–599 (2011).

28. Haffner-Luntzer, M., Kovtun, A., Rapp, A. E. & Ignatius, A. Mouse Models in Bone Fracture Healing Research. *Curr. Mol. Biol. Reports* **2**, 101–111 (2016).

29. Yuasa, M. *et al.* The temporal and spatial development of vascularity in a healing displaced fracture. *Bone* **67**, 208–221 (2014).

30. Histing, T. *et al.* An internal locking plate to study intramembranous bone healing in a mouse femur fracture model. *J. Orthop. Res.* **28**, 397–402 (2010).

31. Röntgen, V. *et al.* Fracture healing in mice under controlled rigid and flexible conditions using an adjustable external fixator. *J. Orthop. Res.* **28**, 1456–1462 (2010).

32. Bartnikowski, N. *et al.* Modulation of fixation stiffness from flexible to stiff in a rat model of bone healing. *Acta Orthop.* **88**, 217–222 (2017).

33. Garcia, P. *et al.* The LockingMouseNail—A New Implant for Standardized Stable Osteosynthesis in Mice. *J. Surg. Res.* **169**, 220–226 (2011).

34. Histing, T. *et al.* An intramedullary locking nail for standardized fixation of femur osteotomies to analyze normal and defective bone healing in mice. *J. Vis. Exp.* **2016**, (2016).

35. Ghiasi, M. S., Chen, J. E., Rodriguez, E. K., Vaziri, A. & Nazarian, A. Computational modeling of human bone fracture healing affected by different conditions of initial healing stage. *BMC Musculoskelet. Disord.* **20**, 562 (2019).

36. Mehboob, A. & Chang, S. H. Effect of initial micro-movement of a fracture gap fastened by composite prosthesis on bone healing. *Compos. Struct.* **226**, 111213 (2019).

37. OReilly, A., Hankenson, K. D. & Kelly, D. J. A computational model to explore the role of angiogenic impairment on endochondral ossification during fracture healing. *Biomech. Model. Mechanobiol.* **15**, 1279–1294 (2016).

38. Wilson, C. J., Schütz, M. A. & Epari, D. R. Computational simulation of bone fracture healing under inverse dynamisation. *Biomech. Model. Mechanobiol.* **16**, 5–14 (2017).

39. Cui, Y. *et al.* Characterization of novel intramedullary nailing method for treating femoral shaft fracture through finite element analysis. *Exp. Ther. Med.* (2020). doi:10.3892/etm.2020.8763

40. Rodrigues, L. B. *et al.* A finite element model to simulate femoral fractures in calves: Testing different polymers for intramedullary interlocking nails. *Vet. Surg.* (2012). doi:10.1111/j.1532-950X.2012.01032.x

41. Samiezadeh, S., Avval, P. T., Fawaz, Z. & Bougherara, H. Biomechanical assessment of composite versus metallic intramedullary nailing system in femoral shaft fractures: A finite element study. *Clin. Biomech.* (2014). doi:10.1016/j.clinbiomech.2014.05.010

42. Tucker, S. M., Wee, H., Fox, E., Reid, J. S. & Lewis, G. S. Parametric Finite Element Analysis of Intramedullary Nail Fixation of Proximal Femur Fractures. *J. Orthop. Res.* (2019). doi:10.1002/jor.24401

43. Cignoni, P. *et al.* MeshLab: An open-source mesh processing tool. in *6th Eurographics Italian Chapter Conference 2008 - Proceedings* (2008).

44. Kazhdan, M. & Hoppe, H. Screened poisson surface reconstruction. *ACM Trans. Graph.* **32**, 1–13 (2013).

45. Adam, A. STL to ACIS SAT conversion ((https://www.mathworks.com/matlabcentral/fileexchange/27174-stl-to-acis-sat-conversion), MATLAB Central File Exchange. (2020).

46. Histing, T. *et al.* A minimally invasive model to analyze endochondral fracture healing in mice under standardized biomechanical conditions. *J. Vis. Exp.* **2018**, 1–7 (2018).

47. El Halabi, F., Rodriguez, J. F., Rebolledo, L., Hurtós, E. & Doblaré, M. Mechanical characterization and numerical simulation of polyether-ether-ketone (PEEK) cranial implants. *J. Mech. Behav. Biomed. Mater.* **4**, 1819–1832 (2011).

48. Wehner, T., Steiner, M., Ignatius, A., Claes, L. & Aegerter, C. M. Prediction of the time course of callus

stiffness as a function of mechanical parameters in experimental rat fracture healing studies - A numerical study. *PLoS One* **9**, 1–16 (2014).

49. Yang, H. *et al.* Characterization of cancellous and cortical bone strain in the in vivo mouse tibial loading model using microCT-based finite element analysis. *Bone* **66**, 131–139 (2014).

50. Boccaccio, A., Uva, A. E., Fiorentino, M., Lamberti, L. & Monno, G. A mechanobiology-based algorithm to optimize the microstructure geometry of bone tissue scaffolds. *Int. J. Biol. Sci.* (2016). doi:10.7150/ijbs.13158

51. Osagie-Clouard, L. *et al.* Biomechanics of two external fixator devices used in rat femoral fractures. *J. Orthop. Res.* 1–6 (2019). doi:10.1002/jor.24034

52. Simon, U., Augat, P., Ignatius, A. & Claes, L. Influence of the stiffness of bone defect implants on the mechanical conditions at the interface - A finite element analysis with contact. *J. Biomech.* **36**, 1079–1086 (2003).

53. Wehner, T., Penzkofer, R., Augat, P., Claes, L. & Simon, U. Improvement of the shear fixation stability of intramedullary nailing. *Clin. Biomech.* **26**, 147–151 (2011).

54. Beaucage, K. L., Pollmann, S. I., Sims, S. M., Dixon, S. J. & Holdsworth, D. W. Quantitative in vivo micro-computed tomography for assessment of age-dependent changes in murine whole-body composition. *Bone Reports* **5**, 70–80 (2016).

55. Borgiani, E., Duda, G., Willie, B. & Checa, S. Bone healing in mice: Does it follow generic mechano-regulation rules? *Facta Univ. Ser. Mech. Eng.* **13**, 217–227 (2015).

56. Checa, S., Prendergast, P. J. & Duda, G. N. Inter-species investigation of the mechano-regulation of bone healing: Comparison of secondary bone healing in sheep and rat. *J. Biomech.* **44**, 1237–1245 (2011).

57. Wehner, T. *et al.* Internal forces and moments in the femur of the rat during gait. *J. Biomech.* **43**, 2473–2479 (2010).

58. Morgan, E. F. *et al.* Correlations between local strains and tissue phenotypes in an experimental model of skeletal healing. *J. Biomech.* **43**, 2418–2424 (2010).

59. Zhu, X. K. & Leis, B. N. Average shear stress yield criterion and its application to plastic collapse analysis of pipelines. *Int. J. Press. Vessel. Pip.* (2006). doi:10.1016/j.ijpvp.2006.06.001

60. Bi, X. *et al.* Correlations Between Bone Mechanical Properties and Bone Composition Parameters in Mouse Models of Dominant and Recessive Osteogenesis Imperfecta and the Response to Anti-TGF-β Treatment. *J. Bone Miner. Res.* (2017). doi:10.1002/jbmr.2997

61. Jepsen, K. J. *et al.* Type I collagen mutation alters the strength and fatigue behavior of Mov13 cortical tissue. *J. Biomech.* **30**, 1141–1147 (1997).

62. Callister, W. D. Materials science and engineering: An introduction (2nd edition). *Mater. Des.* (1991). doi:10.1016/0261-3069(91)90101-9

63. Sacchetti, F. *et al.* Carbon/PEEK nails: a case–control study of 22 cases. *Eur. J. Orthop. Surg. Traumatol.* **30**, 643–651 (2020).

64. Takashima, K. *et al.* Clinical outcomes of proximal femoral fractures treated with a novel carbon fiber-reinforced polyetheretherketone intramedullary nail. *Injury* **51**, 678–682 (2020).

65. Ziran, B. H., O'Pry, E. K. & Harris, R. M. Carbon fiber-reinforced PEEK versus titanium tibial intramedullary nailing: A preliminary analysis and results. *J. Orthop. Trauma* **34**, 429–433 (2020).

66. Baker, C. E. *et al.* Bone Fracture Acute Phase Response—A Unifying Theory of Fracture Repair: Clinical and Scientific Implications. *Clin. Rev. Bone Miner. Metab.* **16**, 142–158 (2018).

67. Perren, S. M. Physical and biological aspects of fracture healing with special reference to internal fixation. *Clin. Orthop. Relat. Res.* **NO. 138**, 175–196 (1979).

68. Harwood, P. J. & Stewart, T. D. Mechanics of musculoskeletal repair devices. *Orthop. Trauma* (2016). doi:10.1016/j.mporth.2016.04.008

69. Augat, P. *et al.* Interfragmentary movement in diaphyseal tibia fractures fixed with locked intramedullary nails. *J. Orthop. Trauma* **22**, 30–36 (2008).

70. Wehner, T., Claes, L., Ignatius, A. & Simon, U. Optimization of intramedullary nailing by numerical simulation of fracture healing. *J. Orthop. Res.* **30**, 569–573 (2012).

71. Augat, P. *et al.* Shear movement at the fracture site delays healing in a diaphyseal fracture model. *J.*

Orthop. Res. **21**, 1011–7 (2003).

72. Schell, H. *et al.* The course of bone healing is influenced by the initial shear fixation stability. *J. Orthop. Res.* **23**, 1022–1028 (2005).

73. Bishop, N. E. *et al.* Shear Does Not Necessarily Inhibit Bone Healing. *Clin. Orthop. Relat. Res.* **443**, 307–314 (2006).

74. Park, S. H., O'Connor, K., Mckellop, H. & Sarmiento, A. The influence of active shear or compressive motion on fracture-healing. *J. Bone Jt. Surg. - Ser. A* **80**, 868–878 (1998).

75. Bhat, A. K., Rao, S. K. & Bhaskaranand, K. Mechanical failure in intramedullary interlocking nails. *J. Orthop. Surg. (Hong Kong)* (2006). doi:10.1177/230949900601400206

76. Ramakrishna, S., Mayer, J., Wintermantel, E. & Leong, K. W. Biomedical applications of polymer-composite materials: A review. *Compos. Sci. Technol.* (2001). doi:10.1016/S0266-3538(00)00241-4

77. Wang, C. *et al.* Three-dimensional finite element analysis of intramedullary nail with different materials in the treatment of intertrochanteric fractures. *Injury* (2020). doi:10.1016/j.injury.2020.10.102

78. Bong, M. R., Kummer, F. J., Koval, K. J. & Egol, K. A. Intramedullary nailing of the lower extremity: Biomechanics and biology. *J. Am. Acad. Orthop. Surg.* **15**, 97–106 (2007).

79. Heijink, A., Zobitz, M. E., Nuyts, R., Morrey, B. F. & An, K. N. Prosthesis design and stress profile after hip resurfacing: a finite element analysis. *J. Orthop. Surg. (Hong Kong)* **16**, 326–332 (2008).

80. Rohlmann, A., Mössner, U., Bergmann, G. & Kölbel, R. Finite-element-analysis and experimental investigation of stresses in a femur. *J. Biomed. Eng.* **4**, 241–6 (1982).

81. Seker, A., Baysal, G., Bilsel, N. & Yalcin, S. Should early weightbearing be allowed after intramedullary fixation of trochanteric femur fractures? A finite element study. *J. Orthop. Sci.* **25**, 132–138 (2020).

82. Stolk, J., Verdonschot, N. & Huiskes, R. Hip-joint and abductor-muscle forces adequately represent in vivo loading of a cemented total hip reconstruction. *J. Biomech.* **34**, 917–926 (2001).

83. Werner, C. & Gorla, R. S. R. Probabilistic Study of Bone Remodeling Using Finite Element Analysis. *Ijame* **18**, 911–921 (2013).

84. Eberle, S., Gerber, C., Von Oldenburg, G., Hungerer, S. & Augat, P. Type of hip fracture determines load share in intramedullary osteosynthesis. *Clin. Orthop. Relat. Res.* **467**, 1972–1980 (2009).

85. Goffin, J. M., Pankaj, P. & Simpson, A. H. A computational study on the effect of fracture intrusion distance in three- and four-part trochanteric fractures treated with Gamma nail and sliding hip screw. *J. Orthop. Res.* **32**, 39–45 (2014).

86. Prasad, J., Wiater, B. P., Nork, S. E., Bain, S. D. & Gross, T. S. Characterizing gait induced normal strains in a murine tibia cortical bone defect model. *J. Biomech.* **43**, 2765–2770 (2010).

87. Song, H., Polk, J. D. & Kersh, M. E. Rat bone properties and their relationship to gait during growth. *J. Exp. Biol.* (2019). doi:10.1242/jeb.203554

88. Erdemir, A., Guess, T. M., Halloran, J., Tadepalli, S. C. & Morrison, T. M. Considerations for reporting finite element analysis studies in biomechanics. *J. Biomech.* **45**, 625–633 (2012).

89. Schemitsch, E. H., Kowalski, M. J., Swiontkowski, M. F. & Harrington, R. M. Comparison of the effect of reamed and unreamed locked intramedullary nailing on blood flow in the callus and strength of union following fracture of the sheep tibia. *J. Orthop. Res.* **13**, 382–389 (1995).

90. White, R. & Camuso, M. Intramedullary nailing. *AO Surgery Reference* (2012). Available at: https://surgeryreference.aofoundation.org/orthopedic-trauma/adult-trauma/tibial-shaft/simple-fracture-transverse/intramedullary-nailing. (Accessed: 31st December 2020)

91. Klein, M. *et al.* Comparison of healing process in open osteotomy model and open fracture model: Delayed healing of osteotomies after intramedullary screw fixation. *J. Orthop. Res.* **33**, 971–978 (2015).

92. Carter, D. R., Beaupré, G. S., Giori, N. J. & Helms, J. A. Mechanobiology of skeletal regeneration. *Clin. Orthop. Relat. Res.* S41-55 (1998).

93. Claes, L. E. & Heigele, C. A. Magnitudes of local stress and strain along bony surfaces predict the course and type of fracture healing. *J. Biomech.* **32**, 255–266 (1999).

94. Lacroix, D. & Prendergast, P. J. A mechano-regulation model for tissue differentiation during fracture healing: Analysis of gap size and loading. *J. Biomech.* **35**, 1163–1171 (2002).

95. Prendergast, P. J., Huiskes, R. & Søballe, K. Biophysical stimuli on cells during tissue differentiation at

implant interfaces. *J. Biomech.* (1997). doi:10.1016/S0021-9290(96)00140-6

96.   Epari, D. R., Taylor, W. R., Heller, M. O. & Duda, G. N. Mechanical conditions in the initial phase of bone healing. *Clin. Biomech.* **21**, 646–655 (2006).

97.   Claes, L. *et al.* Early dynamization by reduced fixation stiffness does not improve fracture healing in a rat femoral osteotomy model. *J. Orthop. Res.* **27**, 22–27 (2009).

98.   Claes, L. *et al.* Late Dynamization by Reduced Fixation Stiffness Enhances Fracture Healing in a Rat Femoral Osteotomy Model. *J. Orthop. Trauma* **25**, 169–174 (2011).

99.   Glatt, V. *et al.* Improved healing of large segmental defects in the rat femur by reverse dynamization in the presence of bone morphogenetic protein-2. *J. Bone Jt. Surg. - Ser. A* **94**, 2063–2073 (2012).

CHAPTER 4 – SYNTHETIC CALCIUM POLYPHOSPHATE AS AN ALTERNATIVE TO ILIAC CREST BONE GRAFT FOR POSTERIOR LUMBAR FUSION PROCEDURES IN MICE

4.1   Abstract:

Spinal fusion procedures are becoming increasingly common, but the incidence of pseudoarthrosis continues to be a significant socioeconomic burden, with up to 35% of all spinal fusions developing pseudoarthrosis. Autologous iliac crest bone graft (ICBG) is the gold standard bone graft material used to engender spinal fusion, but it is limited by donor site morbidity and supply. Therefore, having access to a synthetic bone graft material that induces spinal fusion at a similar or higher rate than ICBG would improve patient outcomes. Recent studies have brought attention to amorphous calcium polyphosphate (Ca-polyP) nanoparticles that are relatively easy to fabricate, are readily resorbed, and promote more robust bone growth than other ceramics being researched. However, it is currently unknown whether Ca-polyP can successfully be used to bring about spinal fusion. The purpose of this study was to synthesize amorphous Ca-polyP nanoparticles and determine how well these nanoparticles engender spinal fusion in a clinically relevant posterior lumbar fusion (PLF) model in mice. Amorphous Ca-polyP nanoparticles, fabricated using a longer-chain sodium polyphosphate (Na-polyP) precursor salt, induced significantly more bone formation than ICBG, but the bone volume fraction of this new bone was significantly less than that exhibited in the ICBG and sham treatment groups. However, the BV/TV, Tb.Sp., and Tb.Th. were not significantly different from between newly formed bone and the host trabecular bone, in any of the groups, suggesting that all of the treatments supported the formation of high-quality bone. These findings suggest that Ca-polyP nanoparticles have the capacity to extend or replace ICBG in murine PLF procedures, but additional research is required to investigate whether similar outcomes can be achieved in large animals or humans.

4.2   Introduction:

Over the past two decades, spinal fusion procedures have become increasingly common with more than 400,000 surgeries being performed in 2015 [1,2]. While these procedures have become increasingly expensive, costing more than $100,000 per procedure [3], the incidence of pseudoarthrosis still remains unacceptably high, with up to 35% of all spinal fusions developing pseudoarthrosis [4,5]. Pseudoarthrosis, often caused by inadequate fixation or insufficient bone growth [6], can lead to increased patient morbidity and need for revision surgery [7,8]. Therefore, advancements in surgical techniques, fixation strategies, and bone grafting would have the potential to reduce the rates of pseudoarthrosis and improve patient outcomes.

While its use is hampered by donor site morbidity and limited supply [9], autologous iliac crest bone graft (ICBG), in combination with prosthetic fixation, is the gold standard for engendering spinal fusion [10]. Other therapeutic strategies often combine ceramic particles, including hydroxyapatite [11], beta-tricalcium phosphate [12], or demineralized bone [13], with exogenous growth factors, including vascular endothelial growth factor (VEGF) [14], platelet-derived growth factor (PDGF) [15], or bone morphometric proteins (BMPs) [10,15], but these strategies only promote intramembranous bone formation while autograft promotes a combination of intramembranous and endochondral ossification [16]. Mesenchymal stem cells (MSCs) [17] and hypertrophic chondrocytes [18] have been used in preclinical models to drive endochondral bone formation and induce spinal fusion at a similar rate to ICBG, but the cells' therapeutic potential is limited by cell harvesting and expansion. Thus, there remains a need for an abundantly available bone graft alternative that can be used to fuse vertebrae at high success rates, with limited adverse side effects.

Recently, amorphous calcium polyphosphate (Ca-polyP) nanoparticles have gained interest as a potential bone graft alternative due to their relatively easy fabrication and their ability to be resorbed and promote bone growth [19]. polyP is thought to be, primarily, a store of metabolic energy and inorganic phosphate for the formation of hydroxyapatite [23], but polyP can also act as a chelator for Ca^{2+} ions [22,26]. Because this removal of Ca^{2+} can be toxic to cells [27], Na-polyP can't be used directly in bone healing applications. Instead, Na-polyP can be used to fabricate amorphous Ca-polyP nanoparticles that have exhibited the ability to enhance MSC [20,21], human umbilical vein endothelial cell (HUVEC) [22], and osteosarcoma cell (SaOS-2) growth and improve SaOS-2 cells

mineralization relative to that induced by hydroxyapatite [19,20] *in vitro*. Furthermore, Ca-polyP nanoparticles, encapsulated within poly(lactic-co-glycolic acid) microparticles, successfully induced the healing of critical-sized calvarial defects in rats, while similarly encapsulated beta-tricalcium phosphate could not [21,22]. However, it is currently unknown whether Ca-polyP can successfully be used to promote sufficient bone growth to successfully engender spinal fusion in a clinically relevant murine posterior lumbar fusion (PLF) model.

We hypothesize that Ca-polyP nanoparticles will perform as well as ICBG at engendering spinal fusion and that, similar to ICBG, Ca-polyP will induce a combination of intramembranous and endochondral bone formation. To test this hypothesis, Ca-polyP nanoparticles were surgically implanted into the posterolateral spinal gutters of a genetically identical mice, and new bone was allowed to form for up to 42 d of normal activity. Bone formation and the number of fused vertebrae were quantified by microcomputed tomography (μCT).

4.3   Materials and Methods:

4.3.1 Ca-polyP nanoparticle synthesis and classification

4.3.1.1 Fabricating Ca-polyP nanoparticles

Ca-polyP nanoparticles were fabricated following the previously published method by Müller, W.E.G., et al [19]. Longer chain-length sodium polyphosphate (Na-polyP) salt, provided as a gift (RegeneTiss, Inc.; Nagano, Japan), was dissolved in deionized water (20 g L^{-1}), and aqueous sodium hydroxide (NaOH, 1M) was added to the Na-polyP solution until the pH was approximately 10. Calcium chloride dihydrate ($CaCl_2$, Sigma-Aldrich; St. Louis, MO) was dissolved in distilled water (112 g L^{-1}) and added dropwise to the Na-polyP solution (1 mL/min). The 1M NaOH solution was added throughout to maintain a pH close to 10. Once all of the $CaCl_2$ solution was added to the Na-polyP solution, the suspension was stirred for an additional 4 h while using the 1M NaOH solution to maintain a pH close to 10. After 4 h, the particles were washed twice with ethanol by centrifuging the suspended particles, aspirating the supernatant, and resuspending the particles in ethanol. After the second wash, the particles were dried in a 60 °C oven.

4.3.1.2 Quantifying the average chain-length of Na-polyP by NMR

The average chain-length of the Na-polyP salt was quantified by Phosphorus-31 nuclear magnetic resonance spectroscopy (^{31}P-NMR) [24]. 100 mg Na-polyP was dissolved in 550 µL deionized water and 50 µL D_2O (Sigma-Aldrich; St. Louis, MO), and the NMR analysis was conducted at 500 MHz on a DRX-500 FT-NMR spectrometer (Bruker; Billerica, MA). The spectrum peaks of the internal and external phosphates were integrated in TopSpin (Bruker; Billerica, MA), and the average chain-length was calculated using **Equation 4.1**.

$$Average\ Chain\ Length = \frac{2 * Peak\ Area_{Internal\ Phosphates}}{Peak\ Area_{External\ Phosphates}} \tag{4.1}$$

4.3.1.3 Quantifying the average particle size of the Ca-polyP nanoparticles by DLS and SEM

The average particle size of the Ca-polyP nanoparticles was quantified by digital light scattering (DLS) and by scanning electron microscopy (SEM). For DLS analysis, the Ca-polyP nanoparticles were suspended in deionized water at a concentration of 5 mg mL^{-1}. After sonication for less than 1 minute and dilution to 0.1 mg mL^{-1}, the average particle size was measured using a Zetasizer (Malvern Panalytical Ltd; Malvern, Worcestershire, England). For SEM imaging, the Ca-polyP nanoparticles were dispersed across an SEM stub with carbon tape and gold sputter-coated with a 108 Auto Sputter Coater (Ted Pella Inc.; Redding, CA). The nanoparticles were imaged using a MERLIN SEM with a GEMINI II column (Carl Zeiss Inc.; Thornwood, NY), and the average particle size was quantified using ImageJ (NIH, https://imagej.nih.gov/ij/). The diameters of at least 50 particles were measured in each of 15 SEM images for a total of 868 measurements.

4.3.1.4 Characterizing the chemical composition of the Ca-polyP nanoparticles by FTIR

The chemical composition of the Ca-polyP nanoparticles was characterized by Fourier transform infrared spectroscopy (FTIR). 2 mg Ca-polyP was pressed into a 200 mg KBr pellet, and the pellet was scanned using a Tensor 27 FTIR (Bruker; Billerica, MA).

4.3.1.4 <u>Characterizing the crystallinity of the Ca-polyP nanoparticles by XRD</u>

The crystallinity of the Ca-polyP nanoparticles was analyzed by x-ray diffraction (XRD). Ca-polyP nanoparticles were evenly dispersed across a glass slide and were scanned from 10° to 80° (2-theta) using a SmartLab diffractometer with Cu Kα X-ray source (Rigaku; Tokyo, Japan).

4.3.2 <u>Harvesting and implanting ICBG</u>

All animal procedures were reviewed and approved by the Institutional Animal Care and Use Committee (IACUC) of Vanderbilt University Medical Center. Male C57BL/6J mice were purchased from Jackson Laboratory and housed at Vanderbilt University in a 12-h light/dark cycle with food and water provided ad libitum. At approximately 8-9 weeks of age, a cohort of mice were sacrificed by CO_2 inhalation, and ICBG was harvested. The harvested ICBG was standardized by volume.

Immediately after harvesting the ICBG, posterolateral lumbar surgeries were performed on separate, yet genetically identical, male mice. Following adequate anesthesia and analgesic, ICBG, Ca-polyP nanoparticles, or saline (sham), was transplanted into the posterolateral gutters of age-matched mice. The internal fascia and skin were closed with absorbable and nylon sutures, respectively, and the mice were transferred to their respective cages and monitored until they regained normal ambulation. For the first 3 d after surgery, analgesic was administered every 12 h to minimize pain.

4.3.3. <u>Quantifying bone formation and lumbar fusion by μCT</u>

The mice were sacrificed 42 d post-surgery, and their lumbar spines were scanned at an isotropic voxel size of 20 μm (55 kVp, 145 μA, 232 ms) using a μCT 40 (Scanco Medical AG; Wangen-Brüttisellen, Switzerland). To quantify fusion, the μCT scans were converted to DICOM image stacks and imported into RadiAnt (Medixant; Poznań, Poland). The image stacks were visually inspected, serially, in all three planes (sagittal, coronal, and axial planes), and the number of fused vertebrae were counted. Fusion had to be seen in at least two planes to be considered. Volume renderings of the posterior lumbar spine, between the L3 and L5 vertebrae, were also generated using RadiAnt.

Next, to quantify the amount of new bone and evaluate its quality, all of the newly formed bone was contoured using Scanco's evaluation module (**Supp. Fig. 4.1**). For simplicity, any remaining ICBG was included. The calcified tissue was segmented from the soft tissue, using a global threshold of 150 per mille of the X-ray attenuation coefficient (1/1000) and no Gaussian noise filter, and the total bone volume (BV), bone volume fraction (BV/TV), trabecular spacing (Tb.Sp.), and trabecular thickness (Tb.Th.) were evaluated using a built-in evaluation script. To compare the bone morphometric properties of the new bone to those of native host bone, a 200 μm thick region of trabecular bone, in the trabecular arch of each vertebra of interest (three vertebrae), was contoured and segmented using the same global parameters.

4.3.4 Statistical analysis

Spinal fusion, bone formation, and bone volume were assessed by Kruskal–Wallis one-way analysis of variance (ANOVA). Tb.Th. and Tb.Sp. were assessed by Welch and Brown-Forsythe ANOVA. The statistical analyses were conducted in Prism V9 (GraphPad; San Diego, California), and all of the averaged results are presented as mean ± standard deviation.

4.4   Results:

4.4.1 Ca-polyP fabrication led to the creation of amorphous nanoparticles

The Na-polyP used to fabricate the Ca-polyP nanoparticles had an average chain-length of 85 ± 19 residues (**Fig. 4.1(a)**), and the particle sizes measured by SEM (**Fig. 4.1(b-c)**) and DLS (**Fig. 4.1(d)**) were 107 ± 42 nm and 106 ± 13 nm, respectively.   The FTIR spectrum (**Fig. 4.1(e)**) contained the characteristic peaks for polyP, including symmetric and asymmetric P-O-P vibrations (730 and 906 cm^{-1}, respectively), symmetric and asymmetric $(PO_2)^{2-}$ vibrations (1001 and 1140 cm^{-1}, respectively) and asymmetric $(PO_2)^{3-}$ vibrations (1244 cm^{-1}), and the XRD spectrum (**Fig. 4.1(f)**) revealed the absence of crystalline peaks.
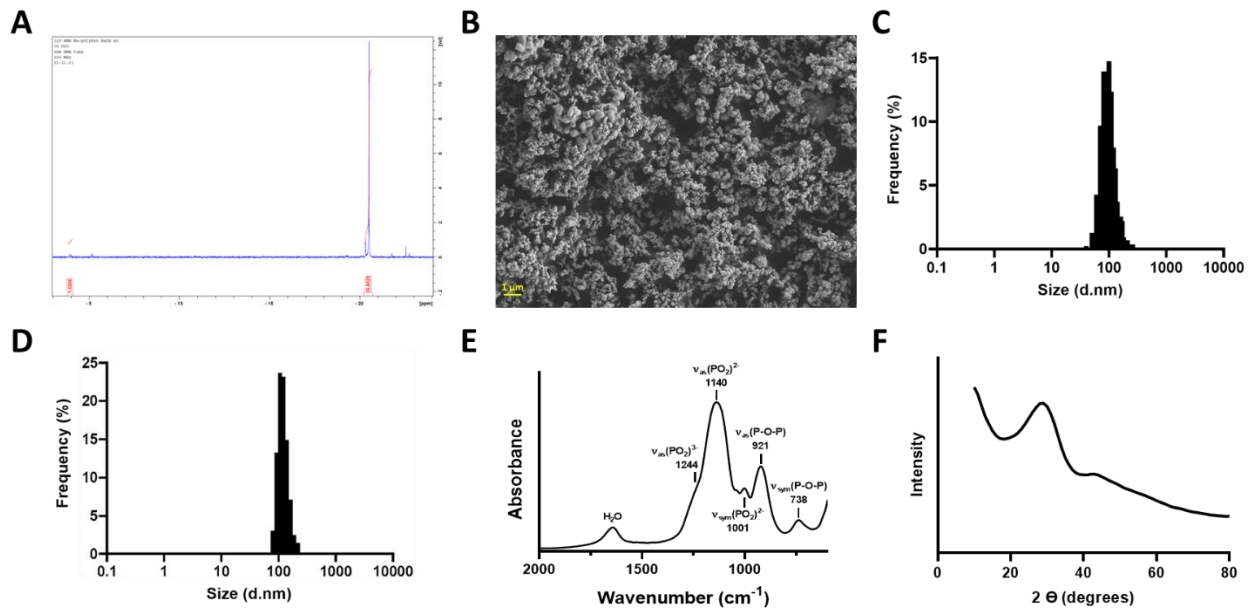
Fig. 4.1. Particle classification analyses were performed to confirm the presence of amorphous Ca-polyP nanoparticles. (a) A representative ^{31}P-NMR spectrum of the Ca-polyP. The average chain-length of the Na-polyP was 85 ± 19 residues. (b) A representative SEM image of the Ca-polyP nanoparticles. The particle sizes measured by SEM (c) and DLS (d) were 107 ± 42 nm and 106 ± 13 nm, respectively. (e) The FTIR spectrum revealed the presence of characteristic peaks for polyP. (f) The absence of crystalline peaks in the XRD spectrum confirmed the amorphous nature of the Ca-polyP nanoparticles.

4.4.2 Ca-polyP treatment induced increased bone formation but decreased bone density relative to ICBG

The 3D reconstructions of the μCT scans (**Fig. 4.2**) suggested that the Ca-polyP and ICBG treatments induced more bone growth than the sham treatment, and these differences were confirmed by the bone morphometric property analyses. The volume of new bone formed 6 wk after Ca-polyP treatment was significantly larger than that formed after sham treatment ($p = 0.0007$), but the bone volume differences between the ICBG and sham treatment groups ($p = 0.0916$) and between the ICBG and Ca-polyP groups ($p = 0.3900$) were not significant (**Fig. 4.3(a)**). In contrast, BV/TV was significantly lower in the Ca-polyP group than in the sham ($p = 0.0387$) and ICBG ($p = 0.0068$) groups (**Fig. 4.3(b)**). Tb.Sp. (**Fig. 4.3(c)**) and Tb.Th. (**Fig. 4.3(d)**) were not significantly different between the treatment groups ($p > 0.85$), and neither BV/TV, Tb.Sp., nor Tb.Th. were significantly different between the newly formed bone and the trabecular bone in the vertebral arch ($p > 0.5$).
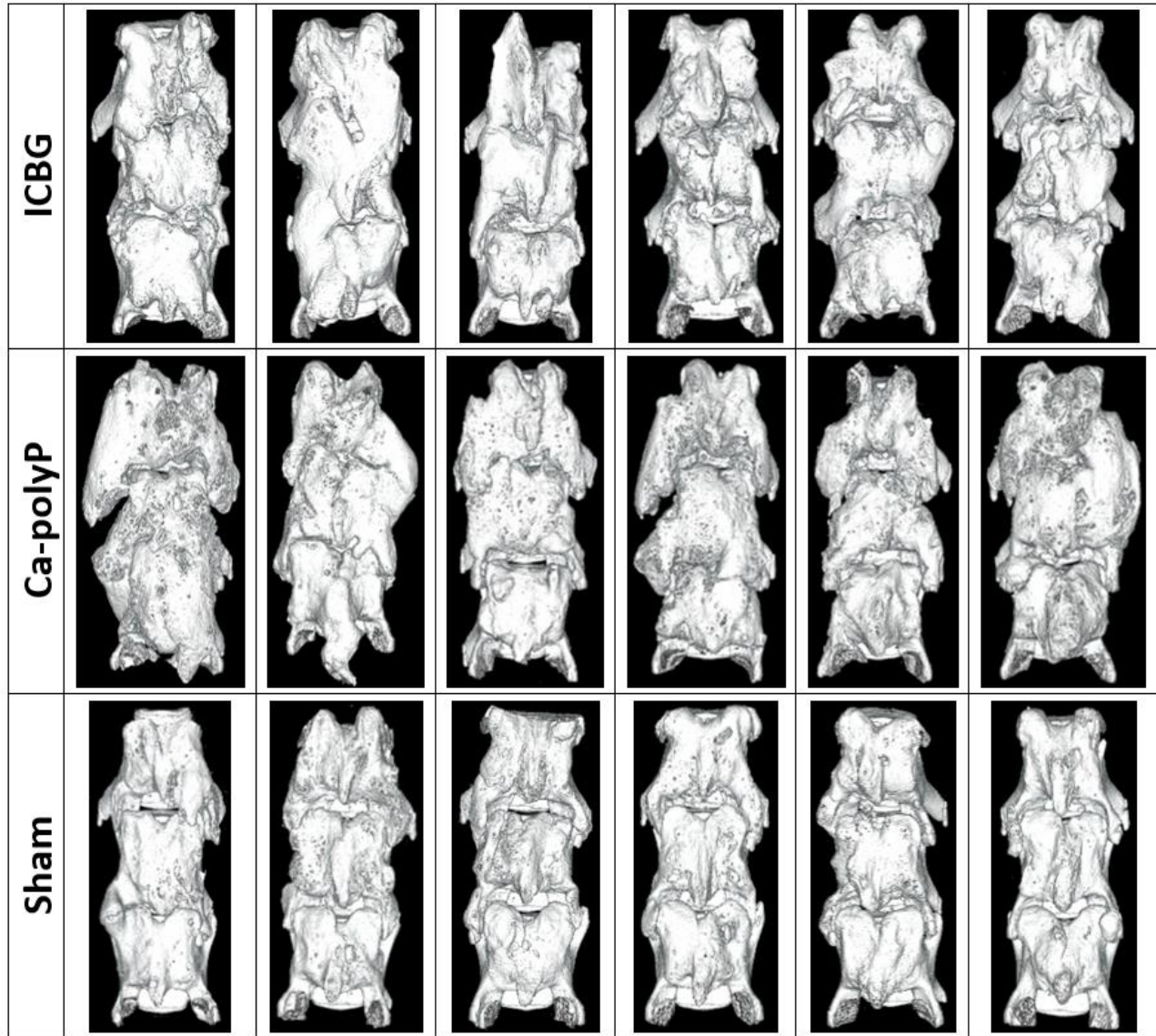
Fig. 4.2. Representative 3D reconstructions of the µCT scans that show the bone growth induced by Ca-polyP nanoparticles, ICBG, and saline (sham).
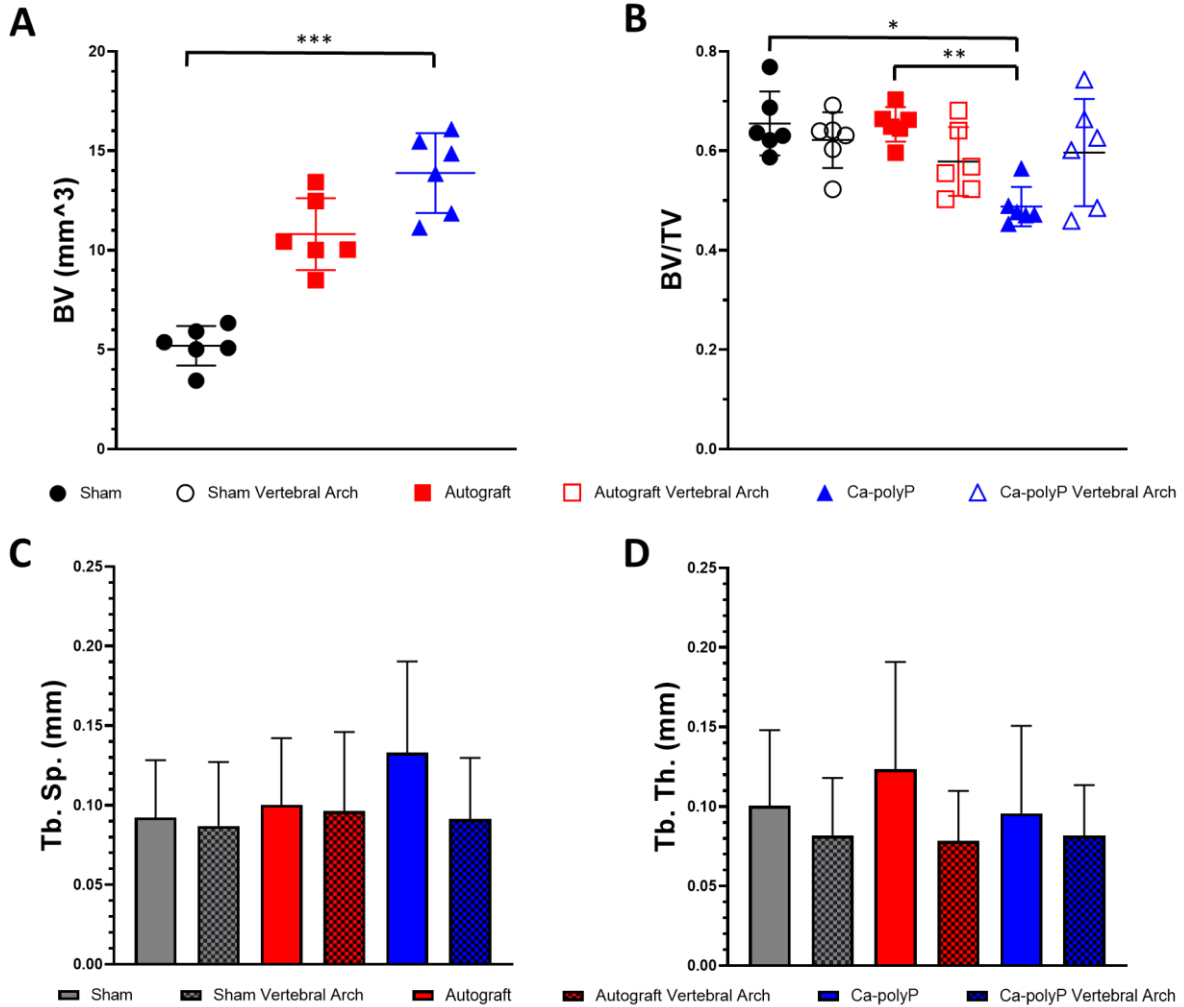
Fig. 4.3. The bone morphometric properties of the new bone and host bone were quantified by μCT. (a) The Ca-polyP nanoparticles induced the formation of slightly more bone than ICBG (p = 0.3900) and significantly more bone than saline (p = 0.0007). (b) The BV/TV of the new bone in the Ca-polyP group was smaller than that in the ICBG (p = 0.0068) and sham (p = 0.0387) groups. (c) Tb.Sp. and (d) Tb.Th. were not significantly different between any of the treatment groups, and none of the bone morphometric properties were significantly different between the new bone and the vertebral arch host bone.

4.4.3 Ca-polyP treatment engendered increased spinal fusion relative to ICBG

Serial inspection of the μCT scans coronally (**Fig. 4.4(a)**), sagittally (**Fig. 4.4(b)**), and axially revealed that the majority of the vertebrae in the region of interest didn't fuse (**Fig. 4.4(c)**) and that the new bone induced by the Ca-polyP nanoparticles and ICBG was beginning to osseointegrate (**Fig. 4.5**). None of the vertebrae fused after sham treatment, and only two of the mice treated with ICBG exhibited any spinal fusion. In contrast, five of mice

treated with Ca-polyP had at least one set of fused vertebrae. The maximum percent of fused vertebrae in any one animal was 75%, observed in one of the ICBG mice, but the mean percentage of fused vertebrae also did not exceed 25% for the ICBG and Ca-polyP treatment groups. The percent of fused vertebrae was significantly higher in Ca-polyP treatment group than in the sham treatment group (p = 0.0220), but the percent of fused vertebrae was not significantly higher in the Ca-polyP treatment group than in the ICBG treatment group (p = 0.4548). Similarly, the percent of fused vertebrae was not significantly higher in the ICBG treatment group than in the sham treatment group (p = 0.6374).
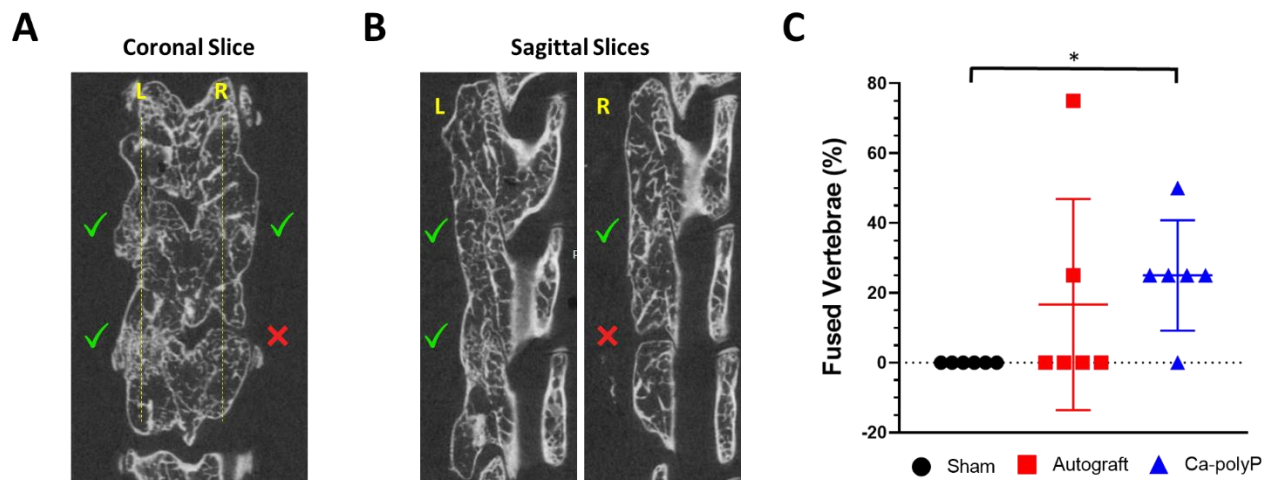
Fig. 4.4. The percentage of fused vertebrae were quantified by μCT. Representative μCT images in the (a) coronal and (b) sagittal planes show fused vertebra. Fusion had to be observed in at least two planes to be counted. (c) A larger percentage of vertebrae fused in the Ca-polyP group than in the ICBG (p = 0.4548) and sham (p = 0.0220) groups, but the average percentage of fused vertebrae did not exceed 25% in any of the treatment groups.
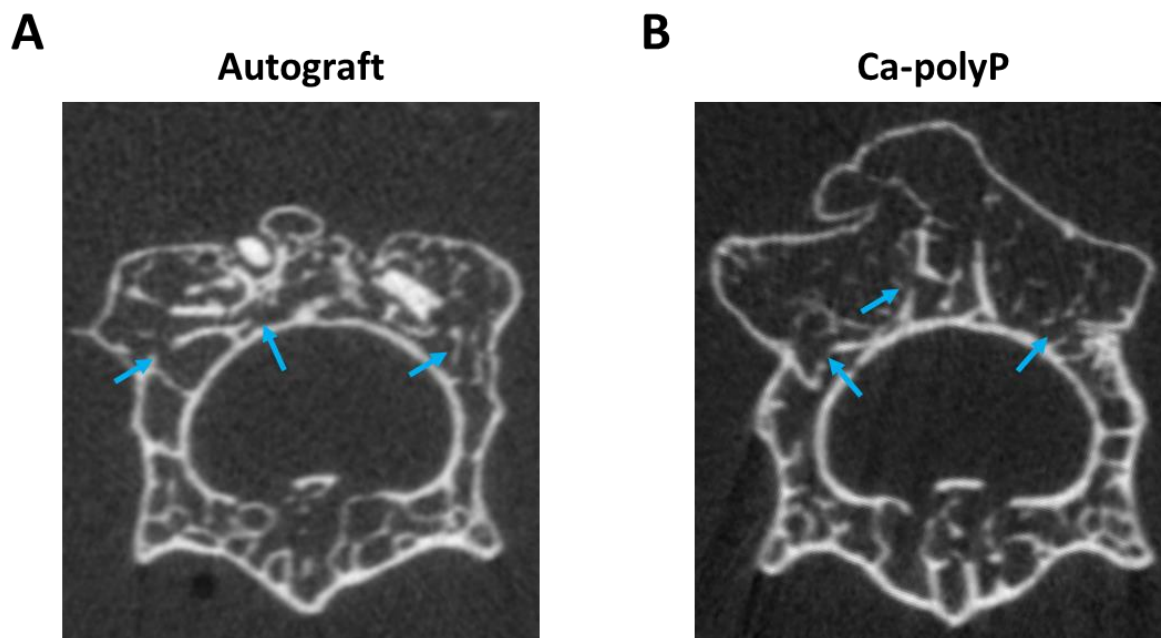
Fig. 4.5. Inspection of the μCT scans, in the axial plane, revealed that the new bone induced by the (a) ICBG and (b) Ca-polyP nanoparticles was beginning to osseointegrate with the vertebrae at 42 d post-implantation (blue arrows highlighting regions of cortical bone resorption).

4.5   Discussion:

Spinal fusion procedures are becoming increasingly common [1,2], but the frequency of unsuccessful fusion remains high [4,5]. Furthermore, current surgical protocols often require the implantation of ICBG, which requires an additional surgery and increased patient morbidity [9,10]. Having access to a synthetic bone graft material that induces spinal fusion at a similar or higher rate than ICBG would improve patient outcomes, and the purpose of this study was to start investigating whether amorphous Ca-polyP nanoparticles have the potential to meet this clinical need.

Ca-polyP nanoparticles were successfully fabricated following a previously published method [19], and, even though a longer-chain Na-polyP salt was used, the nanoparticles' properties were similar to those previously reported [19,23,25]. These Ca-polyP nanoparticles promoted significantly more bone formation than ICBG and induced spinal fusion at a higher, but not statistically significant, rate than ICBG. Additionally, the bone morphometric properties, quantified by μCT, were not significantly different between the newly formed bone and the host trabecular bone, suggesting that high quality bone was formed [26,27].

Interestingly, while the volume of new bone in the mice treated with Ca-polyP nanoparticles was larger than that in the mice treated with ICBG, the bone volume fraction in the Ca-polyP group was significantly smaller than both the sham and ICBG groups. This smaller bone volume fraction may be the result of the Ca-polyP nanoparticles escaping the posterolateral spinal gutters and spreading further from the vertebrae. A similar loss of material, from a defect site, was observed in a recent study, in which a Ca-polyP nanoparticle-saline paste leaked from the alveolar clefts of adolescents after mixing with blood [28]. Mixing the nanoparticles with another synthetic ceramic particle or encapsulating them in a polymer matrix has shown to improve their handling properties while continuing to promote robust bone growth [21,22], but, while Ca-polyP-containing hydrogels have the ability to promote SaOS-2 cell growth and increased gene expression of bone-related genes *in vitro* [29], further investigation is needed to determine whether Ca-polyP-containing scaffolds can successfully promote sufficient bone growth *in vivo*.

One limitation to this study is the amorphous Ca-polyP nanoparticles, used in this model, were only fabricated from longer-chain Na-polyP. The particle classification tests revealed that the Ca-polyP nanoparticles exhibited physicochemical properties comparable to published values [19,30], but the Ca-polyP nanoparticles described herein were synthesized from Na-polyP with a phosphate chain-length approximately twice as long. In humans, the highest concentration of inorganic polyP is contained within platelets (chain-length of 70-75 residues) [23,24], but osteoblasts also contain high concentrations inorganic polyP (chain-length of 210 residues) [31]. Ca-polyP, with a chain-length of 40 residues, was found to increase HUVEC tube formation and intracellular ATP levels more than Ca-polyP with chain-lengths of 3 or 25 residues [32], but the impact of Ca-polyP chain-length on bone formation and spinal fusion requires further investigation.

Another limitation is that the spinal fusion rates and bone morphometric properties were only quantified after 42 d. While this was enough time for the Ca-polyP nanoparticles to be completely replaced by new bone, residual autograft remained in many of the ICBG animals. This remaining ICBG did not impact spinal fusion rates, but the presence of the ICBG fragments likely resulted in slightly larger bone volume, bone volume fraction and trabecular thickness values and slightly smaller trabecular spacing values. However, these values were not

significantly different from the native bone morphometric properties, suggesting that sufficient ICBG had been resorbed.

Next, histological analyses are required to determine whether the Ca-polyP nanoparticles induced intramembranous or endochondral bone formation. Endochondral bone formation is typically observed between the fragments of bridging bone during long bone fracture repair [16,33], but it is also engendered by ICBG. In contrast, many of the synthetic bone graft materials previously investigated as potential "autograft extenders" for spinal fusion applications, including demineralized bone matrix [34], beta-tricalcium phosphate [35,36], biphasic calcium phosphate (85% beta-tricalcium phosphate, 15% hydroxyapatite) [37,38], poly(thioketal urethane) [39], poly (propylene fumarate) [40,41], and poly(lactic-co-glycolic acid) [42,43], primarily promote direct/intramembranous bone formation. Initial histological analysis, performed on formalin-fixed decalcified samples that were embedded in paraffin, cut into 5 μm axial sections, and double-stained with Alcian blue and picrosirius red, revealed the presence of GAG, representing cartilaginous tissue, and collagen, representing bone, in both the Ca-polyP and ICBG mice at 14 d (**Supp. Fig. 4.2(a)**). However, at 42 d, minimal or no GAG staining could be seen in the Ca-polyP and ICBG mice, respectively (**Supp. Fig. 4.2(b)**), indicating that most, if not all, of the cartilage had been converted to bone. This initial analysis suggests that Ca-polyP may induce endochondral bone formation, like autograft, but additional analyses, especially at earlier timepoints, are required.

Finally, while this murine PLF model mimics the bone graft implantation process that takes place during patient surgeries, fixation devices can't be used to stabilize the murine vertebrae after surgery due to the animal's small size. This lack of fixation may expose the fusing vertebrae to higher strains, defined as the movement between the vertebrae relative to their initial distance, and these higher strains can potentially suppress bone formation and enhance cartilage or fibrous tissue formation [33,44,45]. Therefore, the murine PLF model used herein may promote more endochondral bone formation and suppress fusion relative to what would be observed in humans. Additional large animal studies, using fixation strategies similar to those used in humans, could determine whether Ca-polyP nanoparticles can successfully engender spinal fusion in a lower strain environment. Despite these limitations, the Ca-polyP nanoparticles still engendered significantly more bone formation and a higher rate of fusion than ICBG, and the quality of the newly formed bone was not significantly different than that of native bone.

4.6   Conclusions:

This murine PLF study compared the capacity for Ca-polyP nanoparticles to fuse vertebrae and synthesize bone to that for ICBG. The Ca-polyP nanoparticles induced significantly more bone formation and vertebral fusion than the sham treatment and non-significantly induced more bone formation and vertebral fusion than ICBG. While the newly synthesized bone in the Ca-polyP group had a significantly smaller bone volume fraction than that in the ICBG sham groups, none of the bone morphometric properties were significantly different than the host trabecular bone, indicating that high-quality bone was formed in all three groups. Altogether, these findings suggest that Ca-polyP nanoparticles have the capacity to extend or replace ICBG in murine PLF surgeries, but additional studies, with relevant fixation strategies, are required to ascertain whether Ca-polyP nanoparticles have the potential to induce spinal fusion in larger animals or humans.

Supplemental Figures:
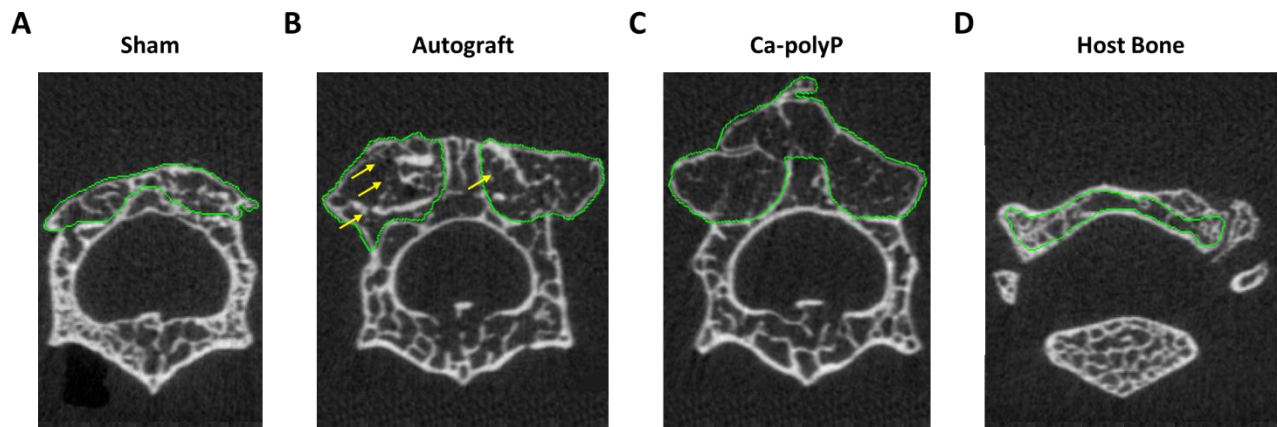
Supp. Fig. 4.1. Representative μCT contours of new bone formed after (a) sham, (b) autograft, and (c) Ca-polyP treatment. Yellow arrows highlight residual autograft after 6 weeks. (d) Representative μCT contour of host bone in the vertebral arch of sham treatment mice.
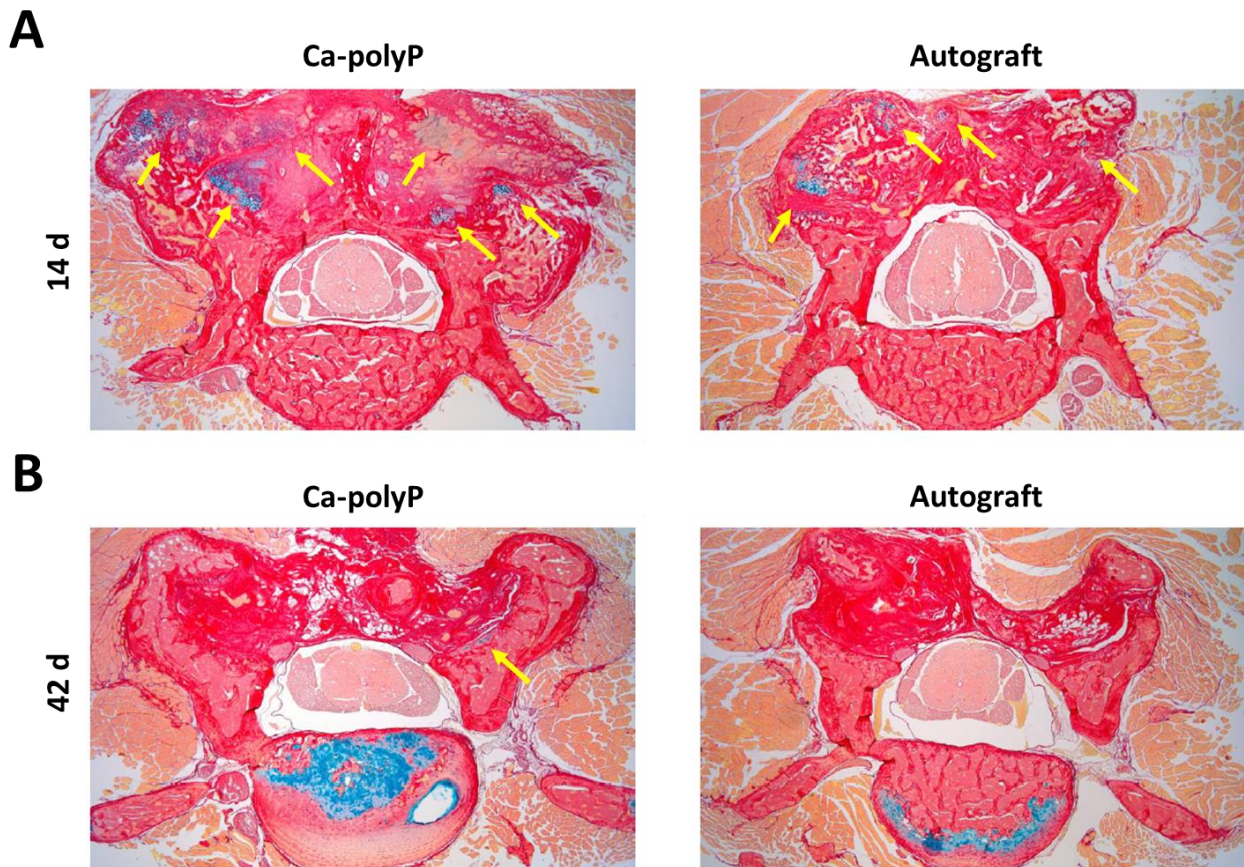
Supp. Fig. 4.2. Initial histological analysis of axial sections that were double-stained with Alcian blue and picrosirius red suggest that Ca-polyP may form bone through endochondral ossification. (a) GAG (blue staining, yellow arrows), representing cartilaginous tissue, and collagen (red staining), representing bone, were present in both the Ca-polyP and ICBG mice at 14 d. (b) At 42 d, minimal or no GAG staining could be seen in the Ca-polyP and ICBG mice, respectively.

References:

1. Martin, B. I. *et al.* Trends in Lumbar Fusion Procedure Rates and Associated Hospital Costs for Degenerative Spinal Diseases in the United States, 2004 to 2015. *Spine (Phila. Pa. 1976).* **44**, 369–376 (2019).
2. Reisener, M. J., Pumberger, M., Shue, J., Girardi, F. P. & Hughes, A. P. Trends in lumbar spinal fusion—a literature review. *J. Spine Surg.* **6**, 752–76 (2020).
3. Sheikh, S. R. *et al.* Can We Justify It Trends in the Utilization of Spinal Fusions and Associated Reimbursement. *Clin. Neurosurg.* **86**, E193–E202 (2020).
4. Chun, D. S., Baker, K. C. & Hsu, W. K. Lumbar pseudarthrosis: A review of current diagnosis and treatment. *Neurosurg. Focus* **39**, 1–8 (2015).
5. How, N. E. *et al.* Pseudarthrosis in adult and pediatric spinal deformity surgery: a systematic review of the literature and meta-analysis of incidence, characteristics, and risk factors. *Neurosurg. Rev.* **42**, 319–336 (2019).
6. Kullar, R., Klineberg, E. & Gupta, M. Complications: Pseudoarthrosis/Nonunion. in *Spine Surgery Basics*

533–540 (Springer Berlin Heidelberg, 2014). doi:10.1007/978-3-642-34126-7_41

7.   Adogwa, O. *et al.* Long-term outcomes of revision fusion for lumbar pseudarthrosis: Clinical article. *J. Neurosurg. Spine* **15**, 393–398 (2011).

8.   Dede, O. *et al.* Revision surgery for lumbar pseudarthrosis. *Spine J.* **15**, 977–982 (2015).

9.   Wang, W. & Yeung, K. W. K. Bone grafts and biomaterials substitutes for bone defect repair: A review. *Bioact. Mater.* **2**, 224–247 (2017).

10. Duarte, R. M., Varanda, P., Reis, R. L., Duarte, A. R. C. & Correia-Pinto, J. Biomaterials and Bioactive Agents in Spinal Fusion. *Tissue Eng. - Part B Rev.* **23**, 540–551 (2017).

11. Spivak, J. M. & Hasharoni, A. Use of hydroxyapatite in spine surgery. *Eur. Spine J.* **10**, 197–204 (2001).

12. Muschik, M., Ludwig, R., Halbhübner, S., Bursche, K. & Stoll, T. β-tricalcium phosphate as a bone substitute for dorsal spinal fusion in adolescent idiopathic scoliosis: Preliminary results of a prospective clinical study. *Eur. Spine J.* **10**, 178–184 (2001).

13. Wang, J. C. *et al.* A comparison of commercially available demineralized bone matrix for spinal fusion. *Eur. Spine J.* **16**, 1233–1240 (2007).

14. Ito, H. *et al.* Remodeling of cortical bone allografts mediated by adherent rAAV-RANKL and VEGF gene therapy. *Nat. Med.* **11**, 291–297 (2005).

15. Lowery, G. L., Kulkarni, S. & Pennisi, A. E. Use of autologous growth factors in lumbar spinal fusion. *Bone* **25**, 47–50 (1999).

16. Zipfel, G. J., Guiot, B. H. & Fessler, R. G. Bone grafting. *Neurosurg. Focus* **14**, e8 (2003).

17. Salamanna, F. *et al.* Mesenchymal stem cells for the treatment of spinal arthrodesis: From preclinical research to clinical scenario. *Stem Cells Int.* **2017**, (2017).

18. Sielatycki, J. A. *et al.* Autologous chondrocyte grafting promotes bone formation in the posterolateral spine. *Jor Spine* **1**, 1–8 (2018).

19. Müller, W. E. G. *et al.* A new polyphosphate calcium material with morphogenetic activity. *Mater. Lett.* **148**, 163–166 (2015).

20. Müller, W. E. G. *et al.* Fabrication of amorphous strontium polyphosphate microparticles that induce mineralization of bone cells in vitro and in vivo. *Acta Biomater.* **50**, 89–101 (2017).

21. Wang, X. *et al.* Amorphous polyphosphate/amorphous calcium carbonate implant material with enhanced bone healing efficacy in a critical-size defect in rats. *Biomed. Mater.* **11**, (2016).

22. Müller, W. E. G. *et al.* Amplified morphogenetic and bone forming activity of amorphous versus crystalline calcium phosphate/polyphosphate. *Acta Biomater.* **118**, 233–247 (2020).

23. Wang, X., Schröder, H. C. & Müller, W. E. G. Amorphous polyphosphate, a smart bioinspired nano-/bio-material for bone and cartilage regeneration: Towards a new paradigm in tissue engineering. *J. Mater. Chem. B* **6**, 2385–2412 (2018).

24. Smith, S. A. *et al.* Polyphosphate exerts differential effects on blood clotting, depending on polymer size. *Blood* **116**, 4353–4359 (2010).

25. Müller, W. E. G. *et al.* Amorphous polyphosphate-hydroxyapatite: A morphogenetically active substrate for bone-related SaOS-2 cells in vitro. *Acta Biomater.* **31**, 358–367 (2016).

26. Greenwood, C. *et al.* The micro-architecture of human cancellous bone from fracture neck of femur patients in relation to the structural integrity and fracture toughness of the tissue. *Bone Reports* **3**, 67–75 (2015).

27. Nakashima, D. *et al.* Quantitative CT-based bone strength parameters for the prediction of novel spinal implant stability using resonance frequency analysis: a cadaveric study involving experimental micro-CT and clinical multislice CT. *Eur. Radiol. Exp.* **3**, 1 (2019).

28. Alkaabi, S. A. *et al.* Safety and feasibility study of using polyphosphate (PolyP) in alveolar cleft repair: a pilot study. *Pilot Feasibility Stud.* **7**, 1–8 (2021).

29. Müller, W. E. G. *et al.* Morphogenetically active scaffold for osteochondral repair (Polyphosphate/alginate/N,O-carboxymethyl chitosan). *Eur. Cells Mater.* **31**, 174–190 (2016).

30. Müller, W. E. G., Tolba, E., Schröder, H. C. & Wang, X. Polyphosphate: A Morphogenetically Active Implant Material Serving as Metabolic Fuel for Bone Regeneration. *Macromol. Biosci.* **15**, 1182–1197 (2015).

31. Schröder, H. C., Kurz, L., Müller, W. E. G. & Lorenz, B. Polyphosphate in Bone. *Biochem.* **65**, 296–303 (2000).

32. Müller, W. E. G. *et al.* Role of ATP during the initiation of microvascularization: Acceleration of an autocrine sensing mechanism facilitating chemotaxis by inorganic polyphosphate. *Biochem. J.* **475**, 3255–3273 (2018).

33. Baker, C. E. *et al.* Bone Fracture Acute Phase Response—A Unifying Theory of Fracture Repair: Clinical and Scientific Implications. *Clin. Rev. Bone Miner. Metab.* **16**, 142–158 (2018).

34. Cammisa, F. P. *et al.* Two-Year Fusion Rate Equivalency between Grafton® DBM Gel and Autograft in Posterolateral Spine Fusion: A Prospective Controlled Trial Employing a Side-by-Side Comparison in the Same Patient. *Spine (Phila. Pa. 1976).* **29**, 660–666 (2004).

35. Dai, L. Y. & Jiang, L. S. Single-level instrumented posterolateral fusion of lumbar spine with β-tricalcium phosphate versus autograft: A prospective, randomized study with 3-year follow-up. *Spine (Phila. Pa. 1976).* **33**, 1299–1304 (2008).

36. Lerner, T., Bullmann, V., Schulte, T. L., Schneider, M. & Liljenqvist, U. A level-1 pilot study to evaluate of ultraporous β-tricalcium phosphate as a graft extender in the posterior correction of adolescent idiopathic scoliosis. *Eur. Spine J.* **18**, 170–179 (2009).

37. Smucker, J. D., Petersen, E. B., Nepola, J. V. & Fredericks, D. C. Assessment of Mastergraft(®) strip with bone marrow aspirate as a graft extender in a rabbit posterolateral fusion model. *Iowa Orthop. J.* **32**, 61–68 (2012).

38. Smucker, J. D., Petersen, E. B. & Fredericks, D. C. Assessment of MASTERGRAFT PUTTY as a graft extender in a rabbit posterolateral fusion model. *Spine (Phila. Pa. 1976).* **37**, 1017–1021 (2012).

39. Mcgough, M. A. P. *et al.* Poly(Thioketal Urethane) Autograft Extenders in an Intertransverse Process Model of Bone Formation. *Tissue Eng. - Part A* **25**, 949–963 (2019).

40. Hile, D. D. *et al.* A poly(propylene glycol-co-fumaric acid) based bone graft extender for lumbar spinal fusion: In vivo assessment in a rabbit model. *Eur. Spine J.* **15**, 936–943 (2006).

41. Lewandrowski, K. U. *et al.* Augmentation of osteoinduction with a biodegradable poly(propylene glycol-co-fumaric acid) bone graft extender. *Biomed. Mater. Eng.* **9**, 325–334 (1999).

42. Chedid, M. K., Tundo, K. M., Block, J. E. & Muir, J. M. Hybrid Biosynthetic Autograft Extender for Use in Posterior Lumbar Interbody Fusion: Safety and Clinical Effectiveness. *Open Orthop. J.* **9**, 218–225 (2015).

43. Walsh, W. R. *et al.* Application of resorbable poly(lactide-co-glycolide) with entangled hyaluronic acid as an autograft extender for posterolateral intertransverse lumbar fusion in rabbits. *Tissue Eng. - Part A* **17**, 213–220 (2011).

44. Borgiani, E., Duda, G., Willie, B. & Checa, S. Bone healing in mice: Does it follow generic mechano-regulation rules? *Facta Univ. Ser. Mech. Eng.* **13**, 217–227 (2015).

45. Wehner, T., Steiner, M., Ignatius, A., Claes, L. & Aegerter, C. M. Prediction of the time course of callus stiffness as a function of mechanical parameters in experimental rat fracture healing studies - A numerical study. *PLoS One* **9**, 1–16 (2014).

CHAPTER 5 – A PERFUSION BIOREACTOR MODEL OF TUMOR-INDUCED BONE DISEASE USING HUMAN CELLS

5.1   Abstract

Advanced solid tumors often metastasize to bone, and, once established in bone, these tumors can induce bone destruction, resulting in decreased quality of life and increased mortality. Neither two-dimensional (2D) *in vitro* models nor three-dimensional (3D) animal models sufficiently recapitulate the human bone-tumor microenvironment needed to fully understand the complexities of bone metastasis; thus highlighting the need for new models. A 3D *in vitro* humanized model of tumor-induced bone disease was developed by dynamically culturing human osteoblast, osteoclast, and metastatic cancer cells together within tissue-engineered bone constructs. Cell-mediated resorption was observed by micro-computed tomography and was quantified by change in mass. Together, these methods can be used to investigate whether the metastatic cancer cells included in the model have the potential to drive osteoclastogenesis and cell-mediated resorption *in vitro*.

5.2   Introduction

Many cancer patients experience tumor-induced bone disease (TIBD), resulting in increased risk of pathologic fracture, reduction in mobility, and severe bone pain [1]. Currently it is not possible to predict which tumors will metastasize to bone or how they will respond to therapeutic intervention after metastasizing. Two-dimensional (2D) cell culture in well plates and animal models have been critical in understanding the underlying mechanisms that mediate the progression of TIBD. However, 2D cell culture techniques are often incapable of replicating the complex three-dimensional (3D) bone-tumor microenvironment that is known to interact with cells and affect disease progression [2]. While animal models more effectively recapitulate the bone-tumor microenvironment, genetic and phenotypic differences

between animal and human tissues hinder clinical translation [3]. Thus, there remains a compelling need for 3D *in vitro* human cell models that can bridge the gap between traditional 2D cell culture and animal models.

Models of TIBD must contain osteoblast precursor cells, osteoclast precursor cells, and metastatic breast cancer cells. Mesenchymal stem cells (MSCs) are multipotent osteoblast cells that have the potential to differentiate into a number of mesenchymal tissues, including bone, cartilage, and fat [4]. MSCs readily adhere to tissue culture flasks *in vitro* and can differentiate into osteoblasts and synthesize a mineralized matrix in the presence of ascorbic acid, dexamethasone, and β-glycerophosphate. MSCs can be harvested from bone marrow [5] or purchased from a supplier. Unlike MSCs, peripheral blood mononuclear cells (PBMCs) can be isolated from discarded, de-identified whole blood samples and can be differentiated towards a macrophage phenotype prior to being differentiated into mature osteoclasts [6]. Finally, MDA-MB-231 metastatic breast cancer cells, which can be purchased from a supplier, have the ability to induce osteolytic bone loss *in vivo*, and many MDA-MB-231 subclones have shown the capacity to colonize and proliferate in bone.

A number of factors must be considered when selecting parameters for a model of TIBD. To promote relevant cell behavior, models must recapitulate the mechanical and morphometric properties of bone and apply mechanical forces comparable to those that occur *in vivo*. The bone-like scaffolds must also contain a sufficient number of osteoblast precursor cells, osteoclast precursor cells, and metastatic breast cancer cells, throughout the entire scaffold, before proceeding with the dynamic cell culture. Additionally, the scaffolds must be immersed in medium throughout the duration of the trial, and sterility must be maintained between the cell seeding and dynamic culture stages. Finally, it is critical to be able to measure scaffold resorption, and we hypothesized that resorption could be quantified by weighing and imaging the scaffolds before cell seeding and after dynamically culturing the cells for 28 d.

Chapter V

5.3   Materials and Methods:

5.3.1 Fabricating bone-like scaffolds

The porous femoral head-tissue engineered bone constructs (FH-TEBCs) used in this model of TIBD were manufactured, following a previously published method [7], from a nanocrystalline hydroxyapatite (nHA)-poly(ester urethane) (PEUR) hybrid polymer composite. These cylindrical FH-TEBCs were 5 mm in diameter and height and had a porosity of 80.2%, an average pore size of 0.7 mm, and a Structure Model Index (SMI) of 1.0.

FH-TEBC molds were printed using a 3Z Studio Inkjet 3D printer (Solidscape), and the support material was dissolved from the castable wax by submerging the molds in Bioact VSO leaching oil (Solidscape; 970041) for at least 24 h in a beaker atop a stirring hot plate, with the heat to set 80 ℃ and the stirrer set to half-maximum. The molds were removed from the oil bath and air-dried for at least 12 h in a chemical fume hood before being filled with nHA-PEUR.

The nHA-PEUR was synthesized from nHA (Sigma-Aldrich; 677418), lysine diisocyanate (LDI; Kyowa Hakka Chemical Co. Ltd.), Poly(caprolactone) triol (PCL300; Sigma-Aldrich; 200387), and iron (iii) acetylacetonate (FeAA; Sigma-Aldrich; 517003) catalyst. The FeAA catalyst was prepared by dissolving 5% FeAA in ε-caprolactone (Fisher Scientific; AC173442500). Using a SpeedMixer (FlackTek Inc.; DAC 150 FVZ-K), the nHA was grafted to the LDI by mixing them together, at a ratio of 45:55 by weight, 10 times for 1 min at 3500 RPM. A 1 min dwell time was implemented between each spin to prevent excessive heat generation. The nHA grafted-LDI was placed in a 50 ℃ oven for 3-5 h, to complete the grafting process, and purged with dried Ar before being stored at 4 ℃. 1. The nHA-PEUR was fabricated by mixing nHA grafted-LDI, PCL300, and 5% FeAA catalyst, at a ratio of 360:140:1, for 30 s at 3500 RPM.

Before the nHA-PEUR became tacky, it was suctioned into the FH-TEBC molds using a vacuum pump. The filled molds were placed in a 50 °C oven for at least 12 h to allow the polymer composite to fully cure. After 12 h, the molds were removed from the oven and the excess nHA-PEUR was cut from the

71

tops and bottoms of the molds using a razor blade. The castable wax mold was then dissolved in a 1:1

acetone:water mixture, leaving behind the FH-TEBCs. Finally, the FH-TEBCs were washed with water,

dried in a 50 °C oven for at least 8 h, and stored at room temperature in a desiccated bottle.

5.3.2 Preparing cell culture media

Osteoblast precursor cells, osteoclast precursor cells, and metastatic breast cancer cells were

cultured separately, in vented tissue culture flasks, before being cultured together, on the FH-TEBCs. Each

cell type required its own cell culture medium, and the cell culture media that were used in this model are

defined in **Table 5.1**.

Table 5.1. Cell culture media used in static and dynamic culture

Cell culture medium	Composition
Complete α-MEM	MEM Alpha, (1X) with L-Glutamine, no nucleosides (α-MEM; Thermo Fisher Scientific; 12561-056) supplemented with 10% Fetal Bovine Serum, Defined (FBS; Fisher Scientific; SH3007002), 1% Anti-Anti 100X (Thermo Fisher Scientific; 15240-062), and 0.1% Amphotericin B (Thermo Fisher Scientific; 15290-026)
Osteogenic α-MEM	Complete α-MEM supplemented with 50 µg mL-1 L-ascorbic acid (Sigma-Aldrich; A4403), 10 nM dexamethasone (Sigma-Aldrich; D4902), 10 mM β-glycerophosphate (Sigma-Aldrich; G9422), and 10 nM Vitamin D (Sigma-Aldrich; D1530)
Osteoclastogenic α-MEM	Complete α-MEM supplemented with 25 ng mL-1 macrophage colony-stimulating factor (M-CSF; Sigma-Aldrich; M6518-10UG) and 50 ng mL-1 receptor activator of nuclear factor kappa-B ligand (RANKL; Sigma-Aldrich; SRP3161-10UG)
Osteoclast precursor expansion α-MEM	Complete α-MEM supplemented with 25 ng mL-1 M-CSF
Co-culture α-MEM	Complete α-MEM supplemented with 10 nM Vitamin D
Complete DMEM	Dulbecco's Modification of Eagle's Medium, 1X with 4.5 g L-1 glucose, L-glutamine, and sodium pyruvate (DMEM; Fisher Scientific; MT10013CV) supplemented with 10% FBS, 1% Anti-Anti 100X, and 0.1% Amphotericin B
MSC growth medium	Mesenchymal Stem Cell Growth Medium 2 with Supplement-Mix (PromoCell; C-28009), 1% Anti-Anti 100X, and 0.1% Amphotericin B

5.3.3 Thawing, isolating, and expanding cells for the model of TIBD

The model of TIBD required osteoblast precursor, osteoclast precursor, and metastatic breast cancer cells to be cultured together within the same scaffolds (tri-culture), and the tri-culture was compared to osteoblast-osteoclast (co-culture) samples and no cell controls. The cells, as summarized in **Table 5.2,** were isolated, thawed, and expanded, following basic cell culture techniques [8]. Both static and dynamic cell culture took place at 37 °C and 5% CO_2 in a humidified cell culture incubator.

Table 5.2: Cells used in the model of TIBD

Cell Type	Supplier
Osteoblast Precursor	
Human Bone Marrow Mesenchymal Stem Cell (hBM-MSC)	Extem Biosciences
Osteoclast Precursor	
Peripheral Blood Mononuclear Cell (PBMCs)	Patient-derived from whole blood (Cooperative Human Tissue Network - Western Division at Vanderbilt University Medical Center)
Metastatic Breast Cancer	
MDA-MB-231	Bone clone from laboratory [9]

hBM-MSCs, frozen at -80 °C after receipt from the vendor, were thawed and suspended in MSC growth medium and transferred to a vented tissue culture flask. The MSC growth medium was changed every 2-3 days, with a Dulbecco's phosphate-buffered saline (DPBS) wash, until the cells reached 80-90% confluence. The hBM-MSCs were passaged twice at a ratio of 1:5 by covering the cells with 0.25% Trypsin, 2.21 mM EDTA, 1X, without sodium bicarbonate (Trypsin; Fisher Scientific; 15333651), incubating the cells for 5-10 min at 37 °C, transferring the cells to a centrifuge tube, centrifuging the cells at 300 ×g and 4 °C for 4 minutes, aspirating the supernatant, and resuspending the cells in MSC growth medium.

The PBMCs were isolated from patient whole blood. The blood was diluted at a 1:1 ratio with DPBS before being carefully layered on top of Ficoll-Paque Plus (Sigma Aldrich; GE17-1440-02) in a centrifuge tube. The volume of Ficoll-Paque Plus was half the volume of diluted blood. The centrifuge tube

was centrifuged at 800 x g and 4 ℃ for 20 min, with brake turned off. The top plasma layer was discarded, and the buffy PBMC layer was transferred to a fresh centrifuge tube. The PBMC layer was washed twice by diluting the layer 1:5 with DPBS and centrifuging the diluted sample at 300 $\times$g at 4 ℃ for 10 min. After the second wash, the PBMC layer was resuspended in macrophage expansion medium, plated in a vented tissue culture flask, and incubated overnight at 37 ℃ and 5% CO_2. The medium was changed, with a DPBS wash, the following morning, after 3 d, and after 6 d. Finally, the osteoclast precursor cells were lifted from the tissue culture plate, counted, and seeded, by incubating the cells in Trypsin at 37 ℃ for 15-30 min, scraping them off with a cell scraper (Fisher Scientific; 08-771-1A), transferring them to a centrifuge tube, centrifuging them at 300 x g for 5 min, and resuspending them in the appropriate volume of osteoclastogenic α-MEM.

MDA-MB-231 cells, frozen at -80 ℃, were thawed and suspended in complete DMEM and transferred to a vented tissue culture flask. The complete DMEM was changed every 2-3 days, with a Dulbecco's phosphate-buffered saline (DPBS) wash, until the cells reached 80-90% confluence. The MDA-MB-231 cells were passaged twice at a ratio of 1:5 by covering the cells with Trypsin, incubating the cells for 5-10 min at 37 ℃, transferring the cells to a centrifuge tube, centrifuging the cells at 300 $\times$g and 4 ℃ for 4 minutes, aspirating the supernatant, and resuspending the cells in complete DMEM.

5.3.4 Quantifying PBMC differentiation and osteoclast resorption

The time-course of PBMC differentiation was identified by seeding the expanded PBMCs from Section 5.3.3 in a multi-well tissue culture plate or atop 2D nHA-PEUR substrates and culturing them in osteoclastogenic α-MEM for up to 21 d. Following the manufacturer's instructions, a tartrate-resistant acid phosphatase (TRAP) staining kit (Sigma-Aldrich; 387A-1KT) was used to quantify number of osteoclasts at each timepoint. The cells were only considered osteoclasts if they were multi-nucleated and stained positive for TRAP (TRAP+). Scanning electron microscopy (SEM) imaging was also performed to visualize resorption of the 2D nHA-PEUR substrates. These nHA-PEUR samples were washed with DPBS

and fixed in 5% glutaraldehyde solution, diluted from Glutaraldehyde Solution, 25% (Fisher Scientific; 02957-1) with water, followed by 2% osmium tetroxide solution (Sigma-Aldrich; 75632-5ML) prior to being dehydrated with ethanol and dried overnight at 80 °C in a vacuum oven. After drying, the samples were placed on SEM stubs with carbon tape, gold sputter-coated with a 108 Auto Sputter Coater (Ted Pella Inc.) and imaged using a MERLIN SEM with GEMINI II column (Carl Zeiss Inc.).

This PBMC differentiation timeline was used to help finalize the cell seeding and dynamic culture timelines outlined in Sections 5.3.7 and 5.3.8.

5.3.5 Determining a viable seeding density for the model of TIBD

MDA-MB-231 cells were seeded onto the scaffolds at various densities to determine how many cells of each type were required. FH-TEBCs were soaked in 70% ethanol for at least 30 min to sterilize. The scaffolds were then washed with DPBS and soaked in 5 μg mL^{-1} fibronectin solution, prepared from fibronectin human protein, plasma (Thermo Fisher; 33016015) dissolved in sterile water, for 1 h at 37 °C. Finally, the scaffolds were transferred to fresh 96-well assay plates and exposed to UV light for 30 min in a cell culture hood. 10^4, 10^5, or 10^6 MDA-MB-231 cells were seeded on these scaffolds and cultured in complete DMEM for 5 d. Following the procedure outlined in Section 5.3.4, the scaffolds were washed, fixed, and imaged by SEM. However, the scaffolds had to be cut in half (2-2.5 mm) or into quarters (1-1.25 mm), using a razor blade, so that the sample heights were compatible the microscope.

5.3.6 Simulating fluid flow within the FH-TEBCs

A computational fluid design (CFD) model was created to determine whether the flow rate applied during the dynamic culture period would be appropriate. This was achieved by comparting the wall shear stress (WSS) distribution within the scaffold to those reported in other *in vitro* studies. The micro-computed tomography (μCT) scan, used to create the scaffold molds, was converted into a stereolithography surface mesh using Scanco Medical's built-in image processing language. The surface mesh was repaired,

smoothed, and simplified, in MeshLab (open-source), to reduce the total number of triangulated faces and ease computation, and the revised surface mesh was converted to an ACIS solid volume using a MATLAB script (MATLAB version R2019b, MathWorks) [10]. This solid volume was imported into Ansys SpaceClaim (Ansys version 18.2, Ansys Inc.) and centered about the global origin. A hollow cylinder, with the same inner diameter as the tubing being used in the bioreactor system, was created and positioned around the scaffold geometry. Using SpaceClaim's volume extract too, the fluid volume in and around the scaffold was created. The geometry was imported into Ansys Fluent, and boundary conditions were applied. The superficial velocity of the inlet fluid was set to 180 μm s^{-1}, calculated from a volumetric flow rate of 0.24 mL min^{-1}, and no outlet gauge pressure was applied. The cell culture medium was assumed to be an incompressible fluid with a constant density of 1000 kg m^3 and a constant dynamic viscosity of 1.45 g m^{-1} s^{-1} [11]. The scaffold and bioreactor tubing were assumed to be rigid and stationary.

5.3.7 Seeding cells onto the FH-TEBCs

The static seeding and dynamic culture timelines are summarized in **Figure 5.1**.
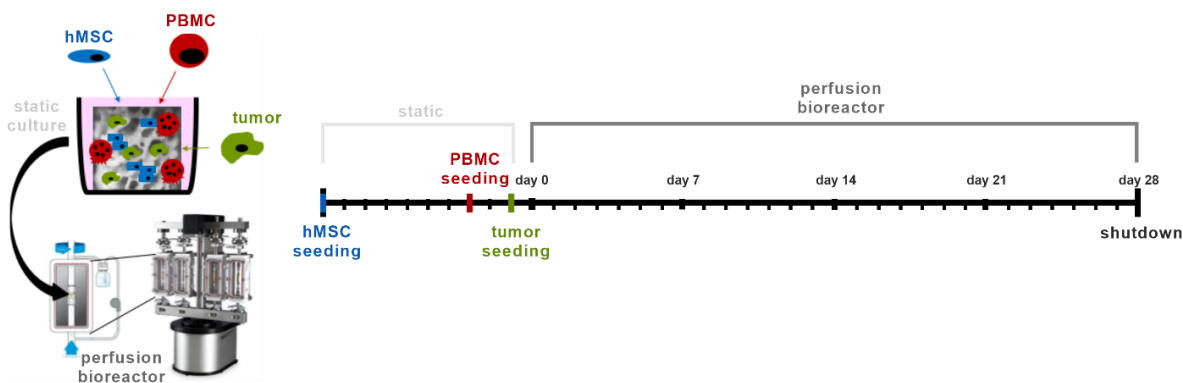
Fig. 5.1. Cell seeding and dynamic culture protocol. hBM-MSCs were seeded in static culture and differentiated for 7 d. Subsequently, PBMCs and MDA-MB-231 cells were seeded in static culture on the same scaffolds. The scaffolds were transferred to the perfusion bioreactor 1 d after tumor cell seeding and are cultured dynamically for 28 d.

Prior to preparing the scaffolds for seeding, the scaffolds were weighed and scanned by μCT, following the steps outlined in Section 5.3.9. After these initial measurements were taken, the FH-TEBCs

were sterilized in 70% ethanol for at least 30 min, washed with DPBS, and soaked in 5 μg mL^{-1} fibronectin solution for 1 h at 37 ^{o}C. Finally, the scaffolds were transferred to fresh 96-well assay plates and exposed to UV light for 30 min in a cell culture hood.

10^5 hBM-MSCs, suspended in 50 μL osteogenic α-MEM, were pipetted onto each of the scaffolds and allowed to adhere for 3 h in a humidified 37 ^{o}C, 5% CO_2 incubator. After 3 h, an additional 150 μL of cell-free osteogenic α-MEM was added to each of the scaffold-containing wells. The scaffolds were incubated for 7 d in static culture, with spent osteogenic α-MEM being exchanged with 200 μL fresh osteogenic α-MEM every 2 d. After 7 d, the spent osteogenic α-MEM was aspirated and 10^5 PBMCs, suspended in 50 μL osteoclastogenic α-MEM, were pipetted onto each of the scaffolds. After 3 h incubation, an additional 150 μL of cell-free osteoclastogenic α-MEM was added to each of the scaffold-containing wells, and the cells were incubated for 2 d in static culture. After 2 d, the spent osteoclastogenic was aspirated and 10^5 MDA-MB-231 cells, suspended in 50 μL osteoclastogenic α-MEM, were pipetted onto each of the scaffolds. After 3 h incubation, an additional 150 μL of cell-free osteoclastogenic α-MEM was added to each of the scaffold-containing wells, and the cells were incubated for 1 d in static culture.

Scaffolds were imaged by confocal microscopy to confirm that all three cell types were present in the scaffold. Following the manufacturer's instructions, the hMSCs and PBMCs were stained with Deep Violet BMQC and CM-Dil CellTracker™ membrane dyes (Thermo Fisher Scientific; C10094 and C7000), respectively, prior to seeding. At the end of the cell-seeding sequence, the scaffolds were cut into quarters, placed on a microscope slide, and imaged using a LSM980 confocal microscope (Carl Zeiss Inc.).

5.3.8 Dynamically culturing cell laden FH-TEBCs

After that final day of static culture, the FH-TEBCs were transferred into lengths of 1/4" ID platinum cured silicon tubing (Cole-Parmer; EW-96201-93). The lengths of platinum cured silicon tubing were connected to the BioDyamic 5200 (TA Instruments) perfusion bioreactor pump to form a closed loop. The bioreactor pump was powered on and the volumetric flow rate was set to 0.24 mL min^{-1}. The cells were

dynamically cultured in co-culture α-MEM for 28 d. After 28 d, the scaffolds were removed from the tubing and prepared for analysis.

5.3.9 Quantifying resorption gravimetrically and by μCT

Resorption was quantified gravimetrically and by μCT, and these analyses required initial measurements to be taken before seeding cells onto the scaffolds and final measurements to be taken after the dynamic culture period.

Prior to taking the initial mass and μCT measurements, the scaffolds were dried overnight in an 80 °C vacuum oven. The scaffolds were then weighed, using an analytical balance, and imaged using a μCT50 (Scanco Medical). The scans were performed with an isotropic voxel size of 5 um, and an integration time of 300 ms. The energy and intensity were set to 70 kV and 114 μA, respectively.

After the dynamic culture period, the scaffolds, designated for SEM, were washed, fixed, and imaged by SEM, following the steps outlined in Section 5.3.4. The scaffolds designated for gravimetric and μCT analyses were washed with DPBS before being placed in microcentrifuge tubed filled with 0.25 M ammonium hydroxide. The microcentrifuge tubes were then placed in a water-filled ultrasonic cleaner for 30 min before being cycled through three freeze-thaw cycles using a -80 °C freezer. Finally, the scaffolds were transferred to a multi-well tissue culture plate and left to dry overnight in an 80 °C vacuum oven.

5.4   Results:

5.4.1 PBMC differentiation timeline

The expanded PBMCs differentiated into osteoclasts within 6 d of being stimulated with RANKL and M-CSF, and the number of osteoclasts increased through the entire 21 d of culture (**Fig. 5.2 (a-b)**). Furthermore, the expanded PBMCs were able to adhere to and differentiate atop the 2D nHA-PEUR substrates (**Fig. 5.2 (c)**), and these osteoblasts exhibited the ability to resorb 2D nHA-PEUR substrates (**Fig. 5.2 (d)**). These data suggested that dynamically culturing the cells for 28 d should be sufficiently long to observe cell-mediated scaffold resorption.
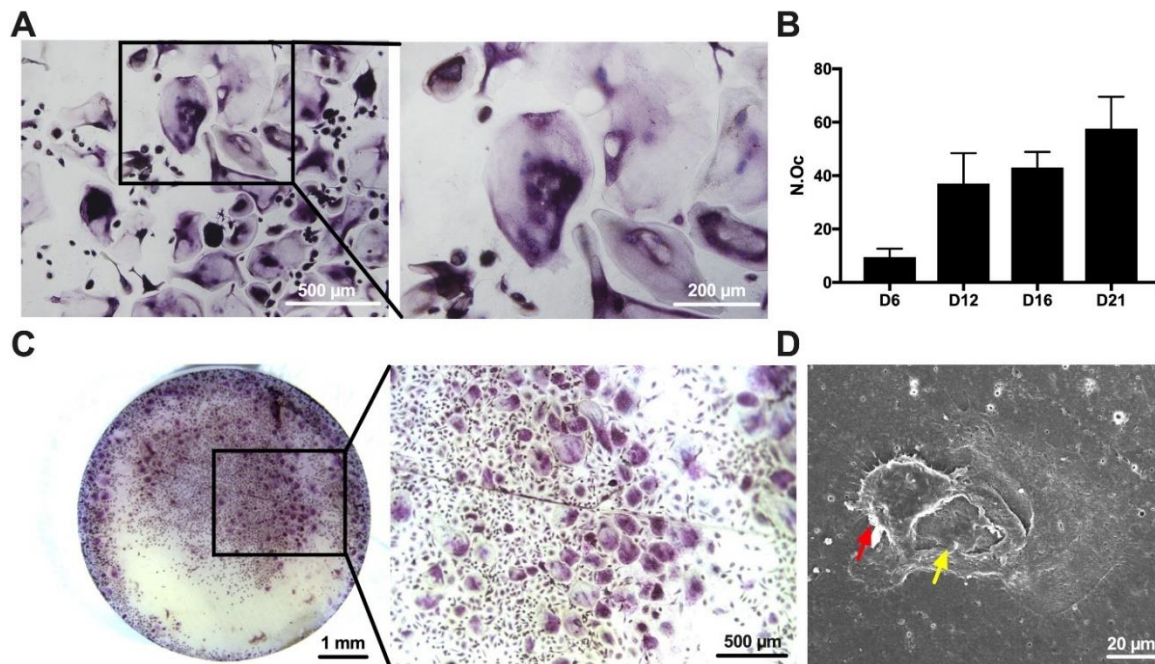
Fig. 5.2. Osteoclast precursor cells were differentiated on multi-well tissue culture plates or resorbable 2D nHA-PEUR substrates. (a-b) TRAP staining at predetermined time points indicated that number of osteoclasts (N.Oc.) within a multi-well tissue culture plate steadily increased over 21-day period. (c) TRAP staining on 2D substrates fabricated from a nHA-PEUR hybrid polymer demonstrated significant osteoclast formation on the surface of nHA-PEUR. (d) Osteoclast pitting of resorbable nHA-PEUR was observed by SEM after 21 d of culture in osteoclastogenic α-MEM.

5.4.2 Cell seeding densities

As shown in **Fig. 5.3 (a-c)**, 10^4 metastatic breast cancer cells ($5*10^4$ cell mL^{-1} in 200 μL) were not enough to completely cover the bone-like scaffold surface while 10^5 cells ($5*10^5$ cell mL^{-1} in 200 μL) and 10^6 cells ($5*10^6$ cell mL^{-1} in 200 μL) of each cell type were sufficient to support cell attachment and proliferation on the scaffolds. Consequently, 10^5 cells of each cell type were seeded onto the bone-like scaffolds when preparing the tri-culture model. Confocal microscopy images after the cell-seeding period revealed that this was a sufficient number of cells to cover the entire scaffold with all three cell types (**Fig 5.3 (d)**).
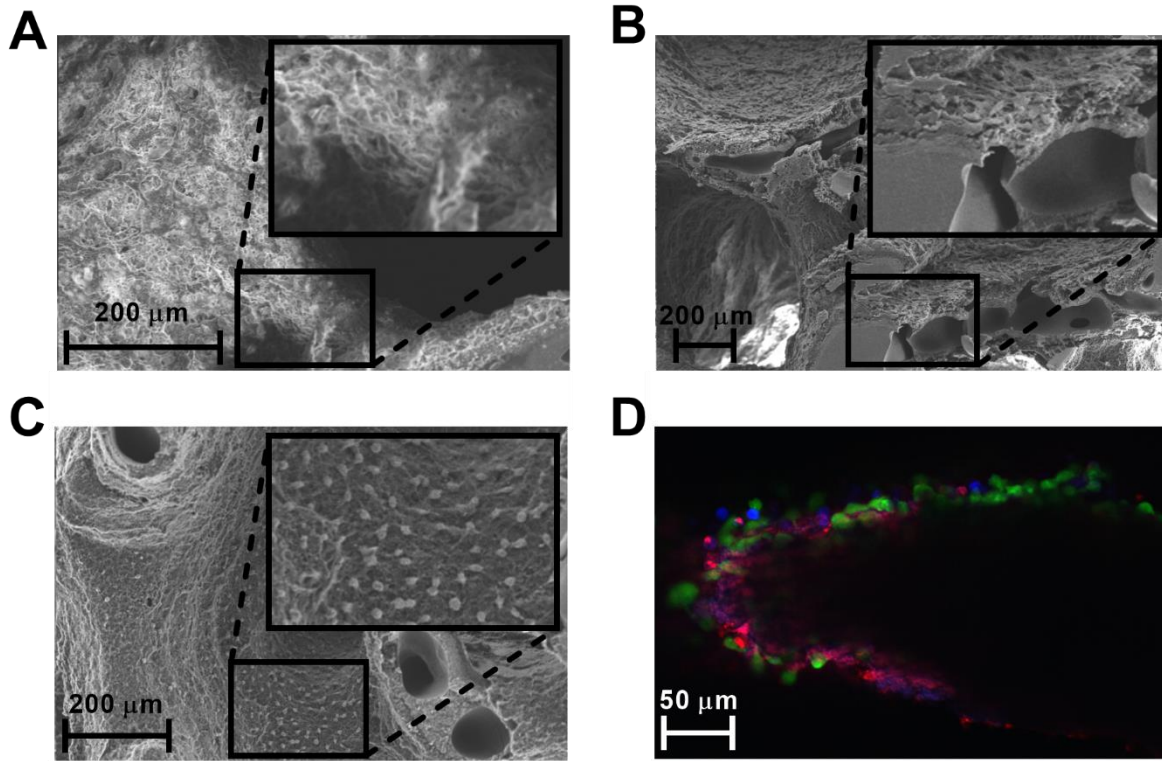
Fig. 5.3. SEM and confocal imaging were used to identify an appropriate cell seeding density. Human metastatic breast cancer cells (a-d), osteoblast precursor cells (d), and osteoclast precursor cells (d) were seeded on bone-like scaffolds and imaged by SEM (a-c) and by single-photon confocal microscopy (d) after 5 d of culture. (a-c) The spherical breast cancer cells were not observed on bone-like scaffolds seeded with 10^4 cells (a), while the bone-like scaffolds seeded with 10^5 (B) and 10^6 (c) cells showed and abundance of cells attached to the surface after 5 d of culture. (d) The osteoblast precursor cells and osteoclast precursor cells were stained with fluorescent dyes (CellTracker™ Violet BMQC and CM-Dil dyes, respectively, Thermo Fisher Scientific) and appear as red and blue, respectively, while the metastatic breast cancer cells were green fluorescent protein labeled.

5.4.3 CFD model of fluid flow

The CFD model of the perfusion bioreactor predicted that cell culture media would flow through the entire scaffold and that regions of higher shear stress were present throughout the inner pores (**Fig. 5.4(a)**). The average superficial velocity and average wall shear stress were calculated to be 180 μm s^{-1} and 4.75 mPa (**Fig. 5.4(b)**), respectively. These data confirmed that the volumetric flow rate settings chosen for this model of TIBD were appropriate.
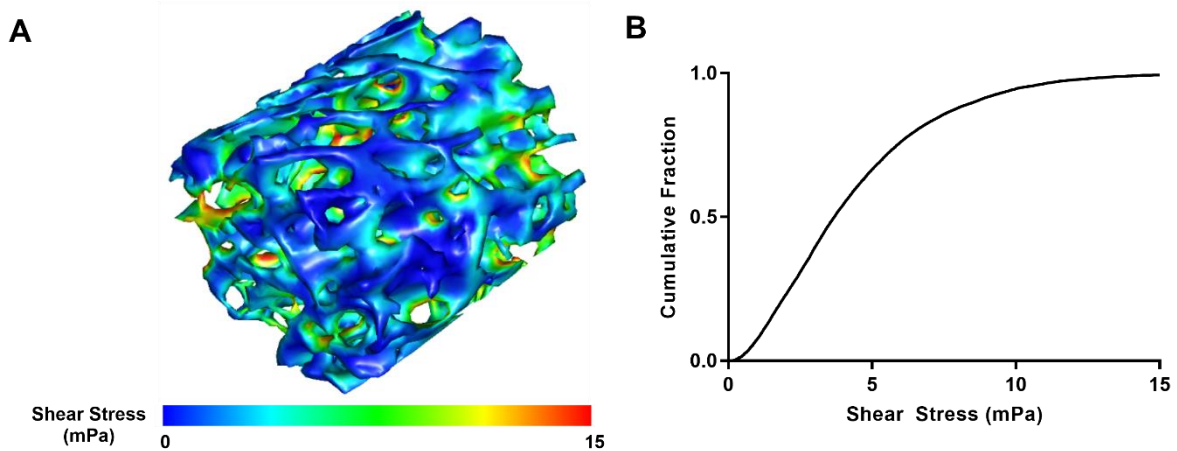
Fig 5.4. Shear stress within the FH-TEBCs was calculated using a CFD model of the perfusion bioreactor. (a) 3D representation of the wall shear stress. (b) Cumulative distribution function of the shear stress data set.

5.4.4 Cancer cell-mediated scaffold resorption

After 7 d of static culture in osteogenic α-MEM, the scaffolds seeded with hBM-MSCs were coated with extracellular matrix, as visualized by SEM (**Fig. 5.5**), and, after 28 d of dynamic culture, SEM images of the scaffold showed the presence of extracellular matrix or tumor cells throughout the co-culture and tri-culture scaffolds (**Fig. 5.6(a)**). TRAP staining of the cells remaining in the multi-well tissue culture plates also revealed that the tri-culture wells contained more mature osteoclasts than the co-culture control group (**Fig. 5.6(b)**). Gravimetrically, the tri-culture scaffolds exhibited significantly more weight loss than the co-culture and no cell control groups (**Fig. 5.6(c)**), and μCT imaging showed that there were regions of bone formation and scaffold resorption throughout the scaffolds (**Fig. 5.6(d)**).
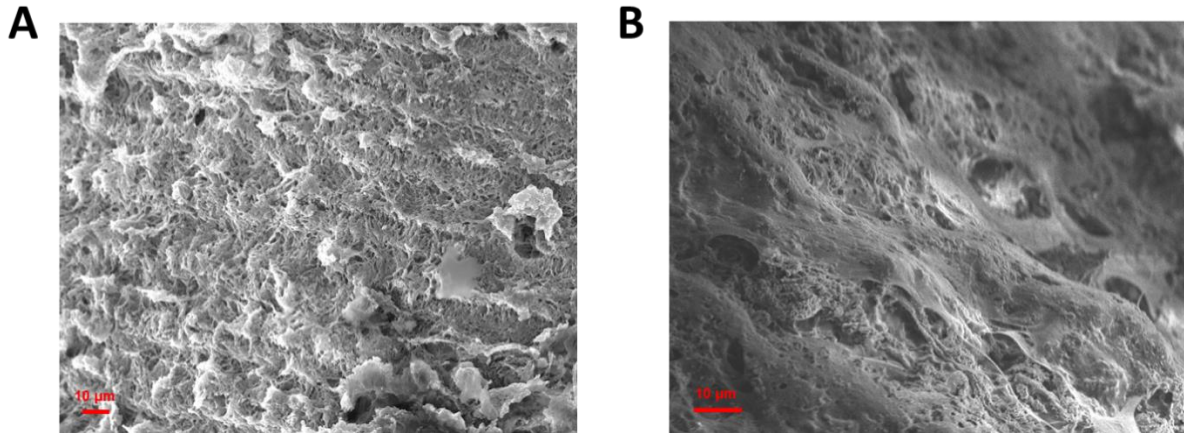
Fig 5.5. Osteoblast precursor cells were seeded and differentiated on resorbable bone-like scaffolds before osteoclast precursor cell and metastatic breast cancer cell seeding. SEM imaging of bone-like scaffolds (a) without osteoblast precursor cells or (b) with osteoblast precursor cells after 7 d of static culture. The images show differentiating osteoblast precursor cells and stringy extracellular matrix in the osteoblast precursor cell-containing scaffolds.
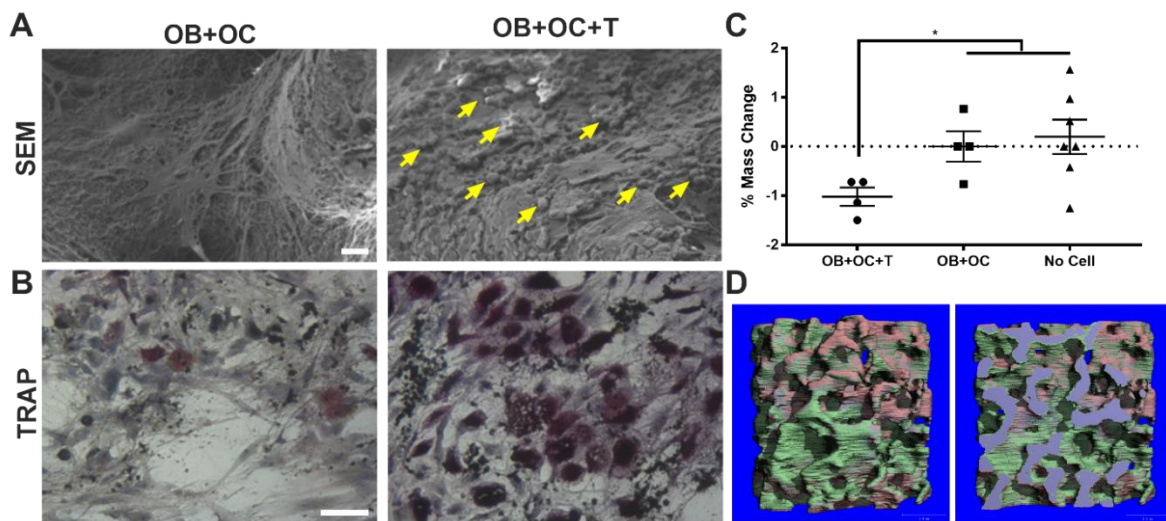
Fig. 5.6. Osteoblast (OB) and osteoclast (OC) precursor cells were dynamically cultured with and without tumor (T) cells on resorbable FH-TEBCs. (a) Representative SEM images of OB+OC and OB+OC+T cohorts on FH-TEBCs after 28 d culture (scale bar = 20 μm). Clusters of spherical tumor cells (yellow arrows) inhabited the extracellular matrix produced by the osteoblasts. (b) Representative TRAP staining of OB+OC and OB+OC+T cohorts after 28 d culture in multi-well tissue culture plates. (c) Percent mass change of FH-TEBCs before and after 28 d perfusion bioreactor culture. (d) Representative overlaid μCT images of an FH-TEBC before/resorbed (red) and after/formed (green) after 28 d of dynamic culture. Purple coloring indicates regions of no volume change, such as within the scaffold interior. The image on the left shows the scaffold exterior while the image on the right is a cross-section of the scaffold.

5.5   Discussion:

Metastatic cancer cells produce tumor-associated factors that drive osteoclastic bone resorption, thus weaking the affected bones and increasing the risk of fracture [12]. However, with the *in vitro* and *in vivo* models currently available, it is not possible to accurately predict where tumor cells will metastasize, how the cancer cells will behave in a bony environment, or how the cells will respond to therapeutic intervention. Therefore, having access to a humanized 3D *in vitro* model of TIBD would facilitate the investigation of the mechanisms of cancer metastasis and the testing of potential therapeutics.

It has been reported that co-culture of tumor cells with hBM-MSCs and monocytes on decellularized trabecular bone induces bone resorption [13], and it has been found that breast cancer cell spheroid formation is enhanced when the breast cancer cells are co-cultured with hBM-MSCs within 3D-printed lattice-type scaffolds [14]. However, the 3D-printed synthetic scaffolds used in this study more faithfully recapitulate the morphometric properties of human trabecular bone, thereby enabling the study of the effects of differences in morphometric properties at multiple skeletal sites on tumor cell fate. Further, the resorbable scaffold material provides a functional endpoint beyond traditional cellular outputs such as gene expression and histological analysis.

There are also a number of *in vivo* models of bone metastasis [15]. Animal models provide a platform for assessing long-term outcomes without a bioreactor and allow investigation of a larger, more representative selection of cellular and biochemical contributions to TIBD than is possible *in vitro*. However, it may be difficult to decouple and evaluate the roles of a single cell type or specific cell signaling pathways, and some preclinical models require immunosuppressed animals that may not be appropriate for use in drug screening.

The 3D *in vitro* model, developed for this study, included the three key cell types involved in TIBD and mimicked the bone-specific features of the *in vivo* TIBD milieu. The SEM imaging showed high surface coverage of the scaffolds with cells and extracellular matrix, suggesting that bone and tumor cells adhered to and proliferated on the scaffolds during culture in the perfusion bioreactor. Additionally, scaffolds

containing osteoblasts, osteoclasts, and tumor cells exhibited significant mass loss while the co-culture scaffolds and no-cell controls exhibited none. Finally, the TRAP staining of cells remaining in multi-well tissue culture plates revealed significantly more TRAP+ multi-nucleated cells in the wells containing osteoblasts, osteoclasts, and tumor cells compared to the wells containing only osteoblasts and osteoclasts. Together, these data suggest that the tumor cells promoted osteoclastogenesis and osteoclast-mediated resorption, making this a model of TIBD that can be used to study how cell activity and therapeutic strategies affect bone loss.

Additively manufactures FH-TEBCs [7] were used in this model of TIBD, they more effectively replicate the complex plate- and rod-like structures found in bone than scaffolds fabricated by gas foaming [17], particulate leaching [18], or freeze-drying techniques [19], and nHA-PEUR was chosen as the model's scaffold material, because it exhibits bone-like strength, promotes osteoblast mineralization relative to pure nHA, and is hydrolytically stable, resorbable, and non-toxic [20]. Other resorbable scaffold materials could potentially be used in this model of TIBD, but the effects of the chemical composition, mechanical properties, and architecture on cell seeding, cell behavior, and the ability to maintain long-term dynamic culture must be considered. Hydrolytic stability should also be evaluated, because if hydrolytic degradation causes too much mass loss, it can potentially affect cell behavior or mask the cell-mediated resorption. To mimic the organic matrix found in bone, scaffolds are often fabricated from natural materials, including collagen type I [21], silk [22], and alginate [23], or from synthetic materials such as poly(α-esters) [24], poly(propylene fumarate) [25,26], and poly(ester urethane)s [20,27,28]. Hydroxyapatite or tricalcium phosphate are typically used as the mineral phase of bone-like scaffolds. Before a new scaffold material is considered, a 2D resorption experiment, using PBMCs and osteoclastogenic α-MEM, should be conducted to confirm that mass loss can be measured and that resorption pits can be seen (**Supp. Fig. 5.1**) [20,29].

The mechanical forces from fluid shear were also kept low in this model of TIBD to promote cell survival without inducing other mechanobiological cellular responses. Other groups have applied superficial velocities between $8 - 4250$ μm s^{-1}, corresponding to wall shear stresses ranging from $0.1 - 170$

mPa [31–33], but the applied superficial velocity of 180 μm s^{-1} in this model of TIBD only generated a median wall shear stress of 4.75 mPa, with higher wall shear stress values existing within the interior of the scaffold and lower wall shear stress values existing along the exterior. Different flow rates could potentially be considered for this model of TIBD, but higher levels of shear stress thought to stimulate osteogenic behavior. This means that changes to the applied flow rate could affect model outcomes.

Changes to the type of bioreactor being used could also impact cell behavior. Dynamic cell culture facilitates the exchange of nutrients and waste products, allowing for improved cell distribution and viability within 3D scaffolds during prolonged experiments. The most common bioreactors used for dynamic 3D cell culture include spinner flasks, rotary wall vessels, and perfusion bioreactors [34]. While spinner flasks and rotary wall vessels can be used improve cell viability along the exterior of 3D scaffolds, perfusion bioreactors are best at sustaining cell viability throughout large porous constructs.

While the model of TIBD described herein successfully utilized SEM imaging and scaffold resorption as functional outcomes, changes can be made to make the model more robust. Optimizing the cell seeding protocol or adding more hBM-MSCs, PBMCs, or MDA-MB-231 cells to the system, throughout the dynamic culture period [35], could potentially extend the duration of dynamic culture or result in increased mass loss. Incorporating additional analyses, such as gene expression, flow cytometry, and extracellular matrix staining, could also make this model a more powerful tool for studying the progression of TIBD. Finally, replacing the MDA-MB-231 cells with patient tumor cells could provide a technology platform for assessing the risk of bone metastases in individual patients.

5.6   Conclusions:

This study focused on creating an *in vitro* humanized model of TIBD using resorbable nHA-PEUR bone-like scaffolds that mimic the bony architecture found in trabecular bone. SEM imaging of the scaffolds showed that the cell seeding and dynamic culture methods resulted in high surface coverage with cells and extracellular matrix, and the gravimetric analysis revealed that the tri-culture scaffolds exhibited significant

mass loss while the co-culture and no-cell controls exhibited no changes in mass. The TRAP staining of cells remaining in multi-well tissue culture plates that revealed the presence of significantly more osteoclasts in the tri-culture wells than in the co-culture wells, suggesting that the mass loss observed in the tri-culture scaffold group was likely caused by the cancer cells promoting osteoclastogenesis and osteoclast-mediated resorption. This model of TIBD can be used to study cancer progression or the effects and mechanisms of therapeutic strategies, and these analytical methods can be used quantify the relative osteoclast-mediated resorption rates of different scaffold materials.

Supplemental Figure:
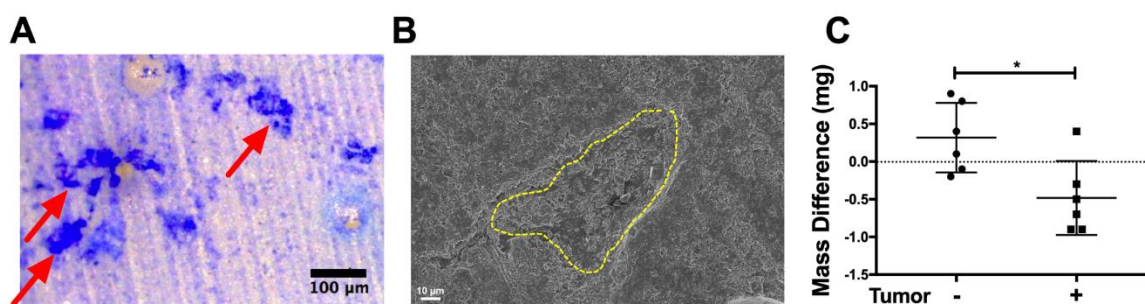
Supp. Fig. 5.1. 2D pilot experiment in which human osteoblast and osteoclast precursor cells were co-cultured with and without tumor cells. (a) Resorption pits on the surface of resorbable nHA-PEUR substrates were stained with toluidine blue. (b) SEM image of resorption pits (outlined in yellow). (c) Substrates showed mass loss in the presence of tumor cells.

References:

1. Coleman, R. E. Skeletal complications of malignancy. *Cancer* **80**, 1588–94 (1997).
2. Vanderburgh, J., Sterling, J. A. & Guelcher, S. A. 3D Printing of Tissue Engineered Constructs for In Vitro Modeling of Disease Progression and Drug Screening. *Ann. Biomed. Eng.* **45**, 164–179 (2017).
3. Sieberath, A. *et al.* A comparison of osteoblast and osteoclast in vitro co-culture models and their translation for preclinical drug testing applications. *Int. J. Mol. Sci.* **21**, 1–23 (2020).
4. Pittenger, M. F. Multilineage Potential of Adult Human Mesenchymal Stem Cells. *Science (80-.).* **284**, 143–147 (1999).
5. Tare, R. S., Mitchell, P. D., Kanczler, J. & Oreffo, R. O. C. Isolation, differentiation, and characterisation of skeletal stem cells from human bone marrow in vitro and in vivo. *Methods Mol. Biol.* **816**, 83–99 (2012).
6. Henriksen, K., Karsdal, M. A., Taylor, A., Tosh, D. & Coxon, F. P. Generation of human osteoclasts from peripheral blood. *Methods Mol. Biol.* (2012). doi:10.1007/978-1-61779-415-5_11
7. Vanderburgh, J. P., Fernando, S. J., Merkel, A. R., Sterling, J. A. & Guelcher, S. A. Fabrication of

Trabecular Bone-Templated Tissue-Engineered Constructs by 3D Inkjet Printing. *Adv. Healthc. Mater.* **1700369**, 1700369 (2017).

8. Phelan, K. & May, K. M. Basic techniques in mammalian cell tissue culture. *Curr. Protoc. Toxicol.* (2016). doi:10.1002/cptx.13

9. Johnson, R. W. *et al.* TGF-beta promotion of Gli2-induced expression of parathyroid hormone-related protein, an important osteolytic factor in bone metastasis, is independent of canonical Hedgehog signaling. *Cancer Res.* **71**, 822–831 (2011).

10. Adam, A. STL to ACIS SAT conversion ((https://www.mathworks.com/matlabcentral/fileexchange/27174-stl-to-acis-sat-conversion), MATLAB Central File Exchange. (2020).

11. Liu, B., Han, S., Hedrick, B. P., Modarres-Sadeghi, Y. & Lynch, M. E. Perfusion applied to a 3D model of bone metastasis results in uniformly dispersed mechanical stimuli. *Biotechnol. Bioeng.* **115**, 1076–1085 (2018).

12. Lynch, M. E. & Fischbach, C. Biomechanical forces in the skeleton and their relevance to bone metastasis: Biology and engineering considerations. *Adv. Drug Deliv. Rev.* **79**, 119–134 (2014).

13. Villasante, A. *et al.* Tissue-Engineered Model of Human Osteolytic Bone Tumor. *Tissue Eng. Part C Methods* **23**, 98–107 (2017).

14. Zhu, W., Holmes, B., Glazer, R. I. & Zhang, L. G. 3D printed nanocomposite matrix for the study of breast cancer bone metastasis. *Nanomedicine Nanotechnology, Biol. Med.* **12**, 69–79 (2016).

15. Simmons, J. K. *et al.* Animal Models of Bone Metastasis. *Vet. Pathol.* (2015). doi:10.1177/0300985815586223

16. Dondossola, E. *et al.* Intravital microscopy of osteolytic progression and therapy response of cancer lesions in the bone. *Sci. Transl. Med.* (2018). doi:10.1126/scitranslmed.aao5726

17. Thein-Han, W. & Xu, H. H. K. Prevascularization of a Gas-Foaming Macroporous Calcium Phosphate Cement Scaffold Via Coculture of Human Umbilical Vein Endothelial Cells and Osteoblasts. *Tissue Eng. Part A* (2013). doi:10.1089/ten.tea.2012.0631

18. Zhang, J., Zhou, H., Yang, K., Yuan, Y. & Liu, C. RhBMP-2-loaded calcium silicate/calcium phosphate cement scaffold with hierarchically porous structure for enhanced bone tissue regeneration. *Biomaterials* (2013). doi:10.1016/j.biomaterials.2013.08.059

19. Fereshteh, Z., Fathi, M., Bagri, A. & Boccaccini, A. R. Preparation and characterization of aligned porous PCL/zein scaffolds as drug delivery systems via improved unidirectional freeze-drying method. *Mater. Sci. Eng. C* (2016). doi:10.1016/j.msec.2016.06.009

20. Lu, S. *et al.* Resorbable nanocomposites with bone-like strength and enhanced cellular activity. *J. Mater. Chem. B* **5**, 4198–4206 (2017).

21. Sokol, E. S. *et al.* Growth of human breast tissues from patient cells in 3D hydrogel scaffolds. *Breast Cancer Res.* (2016). doi:10.1186/s13058-016-0677-5

22. Gupta, P. *et al.* Biomimetic, Osteoconductive Non-mulberry Silk Fiber Reinforced Tricomposite Scaffolds for Bone Tissue Engineering. *ACS Appl. Mater. Interfaces* (2016). doi:10.1021/acsami.6b11366

23. Wang, Y. *et al.* Study of bilineage differentiation of human-bone-marrow-derived mesenchymal stem cells in oxidized sodium alginate/N-succinyl chitosan hydrogels and synergistic effects of RGD modification and low-intensity pulsed ultrasound. *Acta Biomater.* (2014). doi:10.1016/j.actbio.2013.12.052

24. Zhang, P. *et al.* RGD-conjugated copolymer incorporated into composite of poly(lactide-co-glycotide) and poly(l-lactide)-grafted nanohydroxyapatite for bone tissue engineering. *Biomacromolecules* (2011). doi:10.1021/bm2004725

25. Trachtenberg, J. E. *et al.* Extrusion-Based 3D Printing of Poly(propylene fumarate) in a Full-Factorial Design. *ACS Biomater. Sci. Eng.* (2016). doi:10.1021/acsbiomaterials.6b00026

26. Trachtenberg, J. E. *et al.* Effects of Shear Stress Gradients on Ewing Sarcoma Cells Using 3D Printed Scaffolds and Flow Perfusion. *ACS Biomater. Sci. Eng.* acsbiomaterials.6b00641 (2017).

doi:10.1021/acsbiomaterials.6b00641

27. Bonzani, I. C. *et al.* Synthesis of two-component injectable polyurethanes for bone tissue engineering. *Biomaterials* (2007). doi:10.1016/j.biomaterials.2006.08.026

28. Kishan, A. P., Wilems, T., Mohiuddin, S. & Cosgriff-Hernandez, E. M. Synthesis and Characterization of Plug-and-Play Polyurethane Urea Elastomers as Biodegradable Matrixes for Tissue Engineering Applications. *ACS Biomater. Sci. Eng.* (2017). doi:10.1021/acsbiomaterials.7b00512

29. Jimi, E. *et al.* Osteoclast function is activated by osteoblastic cells through a mechanism involving cell-to-cell contact. *Endocrinology* (1996). doi:10.1210/endo.137.5.8612568

30. Manolagas, S. C. Birth and death of bone cells: Basic regulatory mechanisms and implications for the pathogenesis and treatment of osteoporosis. *Endocr. Rev.* **21**, 115–137 (2000).

31. Ban, Y. *et al.* Response of osteoblasts to low fluid shear stress is time dependent. *Tissue Cell* **43**, 311–317 (2011).

32. Kim, J. & Ma, T. Perfusion regulation of hMSC microenvironment and osteogenic differentiation in 3D scaffold. *Biotechnol. Bioeng.* **109**, 252–261 (2012).

33. McCoy, R. J., Jungreuthmayer, C. & O'Brien, F. J. Influence of flow rate and scaffold pore size on cell behavior during mechanical stimulation in a flow perfusion bioreactor. *Biotechnol. Bioeng.* **109**, 1583–1594 (2012).

34. Gaspar, D. A., Gomide, V. & Monteiro, F. J. The role of perfusion bioreactors in bone tissue engineering. *Biomatter* (2012). doi:10.4161/biom.22170

35. Krishnan, V., Vogler, E. A., Sosnoski, D. M. & Mastro, A. M. In vitro mimics of bone remodeling and the vicious cycle of cancer in bone. *J. Cell. Physiol.* **229**, 453–462 (2014).

CHAPTER 6: SUMMARY AND CONCLUSIONS

In this work, *in vitro*, *in silico*, and *in vivo* models were developed to evaluate synthetic bone graft alternatives and novel fixation devices and to investigate their impact on bone growth and the biomechanics of fracture repair. This dissertation was motivated by the high incidence of delayed fracture healing and nonunion, that occurs as a result of biological or mechanical failure as well as the limited number of therapeutic options for preventing these outcomes. Biological failure can be combatted with bone grafting, but autograft is hampered by its limited availability and donor site morbidity. Furthermore, autograft also does not provide much structural support in weight-bearing sites, meaning that early weight-bearing is primarily supported by the fixation device. Mechanical failure can be fixed by removing fibrous tissue from the fracture and selecting a different fixation strategy, but additional research is required to optimize loading patterns and IFS.

Chapter 3 of this dissertation focused on designing a murine IMN for future fracture biomechanics studies. Delayed fracture repair or nonunion can occur if a fracture is not exposed to proper IFS or if a patient's biological healing capacity is inadequate, and this chapter was focused on addressing the first of these causes. Murine models offer experimental and temporal advantages over clinical and large animal models, but there is only one clinically relevant murine IMN with interlocking screws available for purchase, thereby limiting the potential to study how IFS affects fracture repair. Instead of iteratively designing, manufacturing, and trialing different murine IMNs for *in vivo* use, a suite of FE models was created and utilized to predict how different IMN design parameters affect the maximum IFS during gait, the relative contributions of tension, compression, and shear strain within a fracture, and the stresses within the IMN and surrounding bone. Of the parameters investigated (nail material, distance between interlocking screws, and clearance between the nail and endosteal surface), changing the nail material from rigid SS to more compliant PEEK had the largest impact on IFS. The SS nail was predicted to engender OSS less than 10% within the osteotomy, which is in the range expected to promote fracture repair in humans, and the PEEK nail was predicted to engender OSS up to 25%, which is in the upper range of strains that bone and cartilage can withstand in mice. While we hypothesized that reducing the distance between the proximal

and distal interlocking screws would reduce IFS in all of the simulations, reducing this distance had minimal impact on IFS when the IMN was made from SS. Therefore, **Chapter 3** determined that having rigid (e.g., SS) and compliant (e.g., PEEK) IMNs, for use in a murine femoral fracture model, would more effectively support clinically relevant studies investigating the role of the mechanical environment in fracture healing than having IMNs with different distances between interlocking screws.

Chapter 4 of this dissertation focused on finding a potential alternative to ICBG for facture repair by investigating whether Ca-polyP could sufficiently induce bone formation in a murine PLF model. As mentioned in the previous paragraph, delayed fracture repair or nonunion can occur if the fracture is not exposed to proper IFS or if a patient's biological healing capacity is inadequate, and this chapter was focused on addressing the second of these causes. The PLF model was chosen, because spinal fusion procedures are becoming increasingly common, and the incidence of pseudoarthrosis remains high. Amorphous Ca-polyP nanoparticles were chosen as the synthetic bone graft alternative for this study, because they are relatively easy to fabricate, they are readily resorbed, and they promote more robust bone growth than other calcium phosphate-based ceramics. We hypothesized that the Ca-polyP nanoparticles would perform as well as ICBG at engendering spinal fusion, and, 42 d post-surgery, the Ca-polyP nanoparticles induced significantly more fusion than the sham treatment and non-significantly induced more fusion than ICBG. However, the mean percentage of fused vertebrae did not exceed 25% for any of the treatment groups, because this stringent model does not use fixation devices to control the movement between the vertebrae. The Ca-polyP nanoparticles also induced significantly more bone growth, quantified as new bone volume by μCT, than the sham treatment and non-significantly induced more bone growth than ICBG. Interestingly, the new bone BV/TV was significantly lower in the Ca-polyP nanoparticle group than in the sham and ICBG groups, which suggests that the Ca-polyP nanoparticles may have migrated further away from vertebrae than the ICBG. Nevertheless, there being no significant difference in bone morphometric properties between the newly formed bone and the trabecular bone in the vertebral arch signified the formation of high-quality mature bone in all treatment groups. Altogether, these findings indicate that Ca-polyP nanoparticles can be used to extend or replace ICBG in murine PLF surgeries, but

additional studies are required to determine whether Ca-polyP nanoparticles have the potential to induce spinal fusion, at a similar rate as ICBG, in large animals or humans. Additional research is also required to identify whether Ca-polyP nanoparticles can augment or replace ICBG in other surgical applications.

Finally, **Chapter 5** of this dissertation focused on developing a 3D *in vitro* humanized model of TIBD. This chapter was motivated by how bone metastases induce bone destruction, resulting in decreased quality of life and increased mortality, and how the 2D *in vitro* models and the 3D *in vivo* models currently used to study bone metastases do not recapitulate the human bone-tumor microenvironment enough to properly study tumor progression and therapeutic strategies. This model was developed by dynamically culturing human osteoblast, osteoclast, and metastatic cancer cells within resorbable tissue-engineered bone constructs, visualizing cell fate and ECM production by SEM, confocal microscopy, and µCT, and quantifying cell-mediated resorption by change in mass. Imaging revealed that cells were distributed across the entire scaffold surface after seeding and that there were regions of ECM deposition and scaffold resorption throughout the scaffold after the dynamic culture period. Additionally, gravimetric analysis revealed that the tri-culture scaffolds exhibited significant mass loss while the co-culture scaffolds and no-cell controls exhibited no mass loss. Finally, TRAP staining of cells remaining in multi-well tissue culture plates revealed significantly more TRAP+ multi-nucleated cells in the tri-culture wells than in the co-culture wells. Collectively, these data suggest that the metastatic cancer cells promoted osteoclastogenesis and osteoclast-mediated resorption. This model could be used to study the impact of bone metastases and potential drug therapies, but it also can be used to evaluate the relative cell-mediated resorption of scaffolds and cements that are designed to reduce the risk of delayed fracture repair or nonunion by improving mechanical stability at the fracture and promoting vascularization and bone growth.

CHAPTER 7: FUTURE DIRECTIONS

While this dissertation presents the development of models and materials for studying novel bone graft materials and the biomechanics of fracture repair, additional work is required before these learnings and materials can be implemented clinically. This section will propose studies focused on improving and applying the models and materials discussed in the previous chapters and will introduce other relevant models that can potentially be used to study how synthetic bone graft materials perform under weight-bearing conditions.

7.1   Creating and evaluating weight-bearing fracture healing models for studying synthetic bone grafts

In **Chapter 3**, FE modeling was used to study how different IMN design parameters, including nail material, distance between interlocking screws, and clearance between the nail and endosteal surface, impact IFS in a mid-diaphyseal femoral osteotomy in mice, and these simulations predicted that a compliant nail (e.g. PEEK) could be used to complement the commercially available SS nail when studying the biomechanics of fracture repair. Our industry collaborators claimed that it would be easier to fabricate a IMN from a compliant polymer than it would be to change the distance between the interlocking screws, because no changes to the guiding tool would need to be made. However, they have not made an IMN this small before, so additional manufacturing challenges may arise. From an implantation standpoint, it is unclear whether a compliant nail can be used as a one-for-one replacement of the commercially available SS IMN. Potential challenges include inserting the compliant nail into the femur and securing it in place, creating the osteotomy without damaging the nail, and inserting the interlocking screws into the compliant nail. To continue advancing this work, prototype IMNs should be fabricated and trialed before future *in vivo* studies are planned.

While intramedullary nailing can engender healing in otherwise healthy patients, bone grafting may be required in patients exhibiting poor fracture healing biology. A synthetic weight-bearing bone graft, that can be paired with IMNs, could protect the fracture and fixation device while guiding repair. To fill this

clinical need, the Ca-polyP nanoparticles, from **Chapter 4**, were incorporated into resorbable poly(thioketal urethane) (PTKUR) scaffolds, similar to those used in **Chapter 5**. These Ca-polyP-PTKUR scaffolds were implanted in the muscle adjacent to the femoral mid-diaphysis in mice, and bone ingrowth, as visualized by x-ray and μCT, was compared against that induced by nHA-PTKUR scaffolds after 6 wk. While bone ingrowth wasn't observed in the nHA-PTKUR scaffolds, significant bone ingrowth could be seen within the Ca-polyP-PTKUR scaffolds (**Fig. 7.1**).
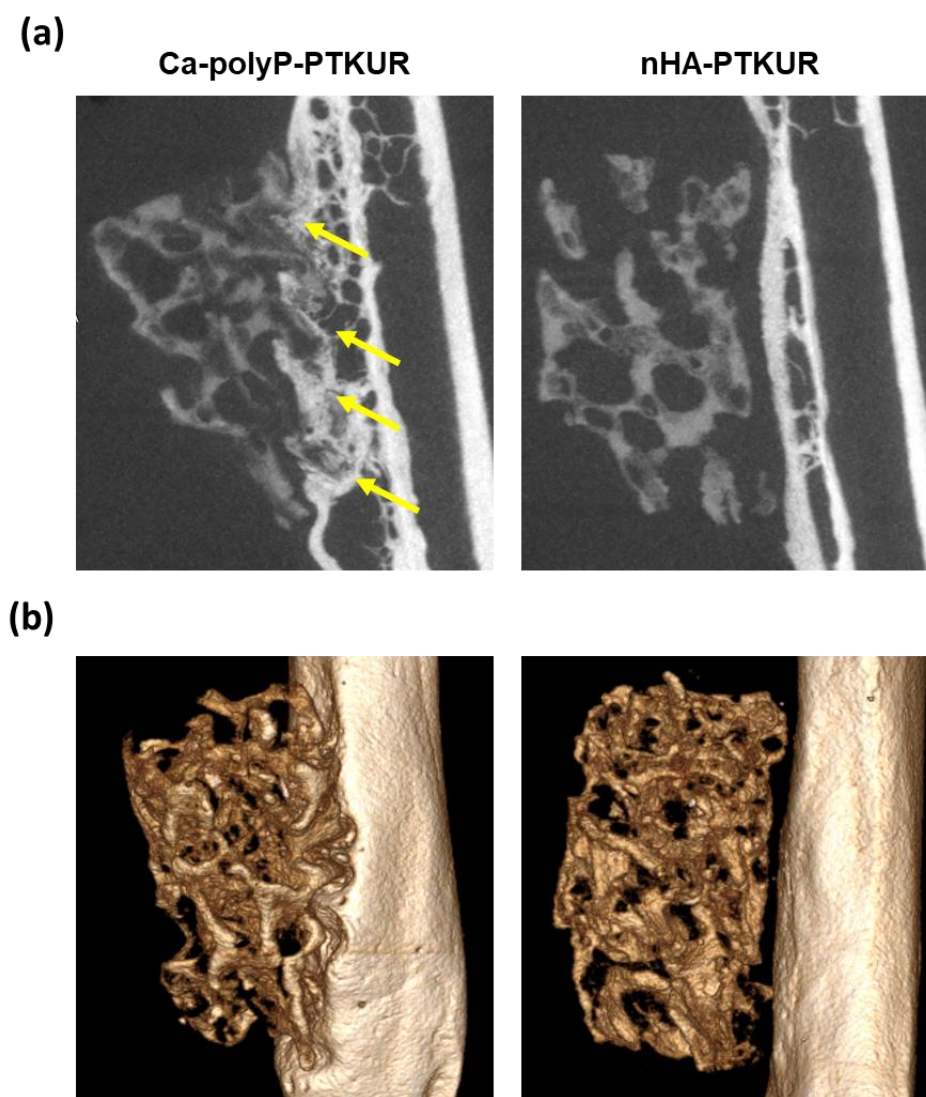
Figure 7.1. Resorbable Ca-polyP-PTKUR scaffolds supported bone ingrowth in a murine femoral muscle model after 42 d. (a) X-ray imaging showed that Ca-polyP-PTKUR scaffolds induced bone ingrowth from the neighboring periosteum while nHA-PTKUR scaffolds didn't (yellow arrows). (b) 3D reconstructions from μCT scans revealed that this bone growth occurred along the entire edge of the Ca-polyP-PTKUR scaffolds. Images used with permission from Satoru Egawa.

This proof-of-concept trial revealed that the Ca-polyP nanoparticles could still induce significant bone growth even when they are incorporated into a resorbable polymer matrix, but it wasn't clear whether this result would continue to hold true in a mid-diaphyseal fracture or osteotomy. To study this, a weight-bearing Ca-polyP-PTKUR scaffold, that could be used with an intramedullary pin or IMN, was designed and a fabricated following the same mold-filling process used in **Chapter 5**. This scaffold, with a solid cylindrical core on the inside and a porous exterior (**Fig. 7.2(a)**), was designed with the goal of inducing a similar outside-in healing response to that seen when the Masquelet technique is implemented [1,2]. An additional benefit to using a resorbable scaffold would be that the normally requisite second surgery to remove the cement cylinder would not be required. We were able to successfully fabricate and implant PTKUR and Ca-polyP-PTKUR scaffolds (**Fig. 7.2 (b-c)**), but bone ingrowth was only observed at the distal and proximal scaffold edges after 42 d (**Fig. 7.3 (d)**). We hypothesize that bone ingrowth may have been hampered by potential damage to the periosteum during surgery, but additional trials are required to determine why robust healing did not occur and whether changes to the scaffold are required.
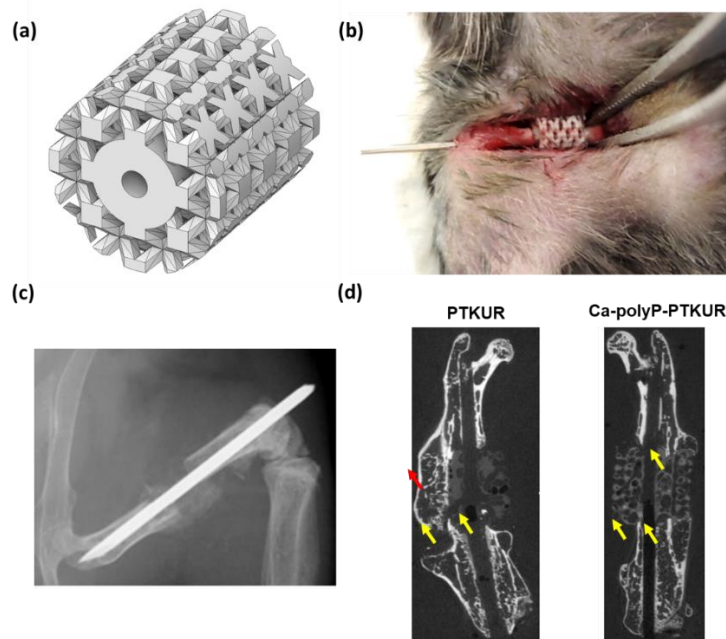
Figure 7.2. Prototype resorbable cylindrical spacers with porous shells supported bone ingrowth in a murine diaphyseal defect model after 42 d. (a) Digital reconstruction of the spacer with porous shell. (b) Representative image of the scaffold position after surgery. (c) Representative x-ray image of scaffold and bone fixed with intramedullary pin. (d) As shown by x-ray, the PTKUR and Ca-polyP-PTKUR scaffolds supported bone ingrowth (yellow arrows). Excess bone formation (red arrow) was hypothesized to have been caused by residual periosteum or tendon.

All of the fracture biomechanics and weight-bearing bone graft research discussed so far has focused on diaphyseal fractures, but metaphyseal fractures, especially in weight-bearing sites, are also plagued by high rates of delayed healing and nonunion [3–5]. Furthermore, metaphyseal fractures often heal differently than diaphyseal fractures in that primary fracture repair is a more prominent process and that little to no callus is formed [6,7]. For these reasons, weight-bearing metaphyseal defect models could be beneficial tools for studying how resorbable bone graft materials respond to the mechanical stresses and strains in these sites.

To take advantage of the murine model benefits described in **Chapter 3**, a weight-bearing metaphyseal defect model was proposed to study how IFS affects bone formation and bone graft resorption in the distal femur of rats. This model would be based on a previously published wedge defect model [8] but would utilize a compliant fixator instead of a rigid metal T-plate. We initially proposed filling this defect filled with resorbable nHA-PEUR, but solid nHA-PEUR would be too stiff [9] to engender appreciable IFS. Therefore, the defect would need to be filled with a porous scaffold that could promote and withstand higher strains. Our lab has previously studied the mechanical properties of various PEUR foams [10–12], and we hypothesized that composite foams would offer similarly high yield strains. Following the procedure outlined in **Chapter 8.4**, nHA-PEUR foams, with 7-42 wt% nHA, were fabricated using 300-900 molecular weight polyols. Quasi-static compression testing revealed that these foams had compressive moduli of 0.2-58 MPa (**Fig. 7.3 (a)**). Incorporating these results into FE models of the metaphyseal wedge defect, that were created using a μCT scan of a rat femur (**Fig. 7.3 (b-c)**) and the material properties listed in **Table 7.1**, revealed that the compliant fixators would need to have elastic moduli of 15 MPa (TPU) and 2500 MPa (Vero) to engender median equivalent strains of 6-11% and 1.5-2.5%, respectively (**Fig. 7.3 (d)**). Prototype fixator plates, fabricated using a Polyjet 3D printer, were purchased from Xometry (Derwood, MD), but funding and group research interests shifted before the fixators could be evaluated *ex vivo*.

Table 7.1. FE Model of Murine Metaphyseal Wedge
Defect - Mechanical Properties

Material	E_s (MPa)	ν
Cortical Bone[13]	8,500	0.30
Trabecular Bone[13]	2,500	0.30
nHA-PEUR Foam	7.0 or 20.9	0.38
TPU	15	0.49
Vero	2500	0.3
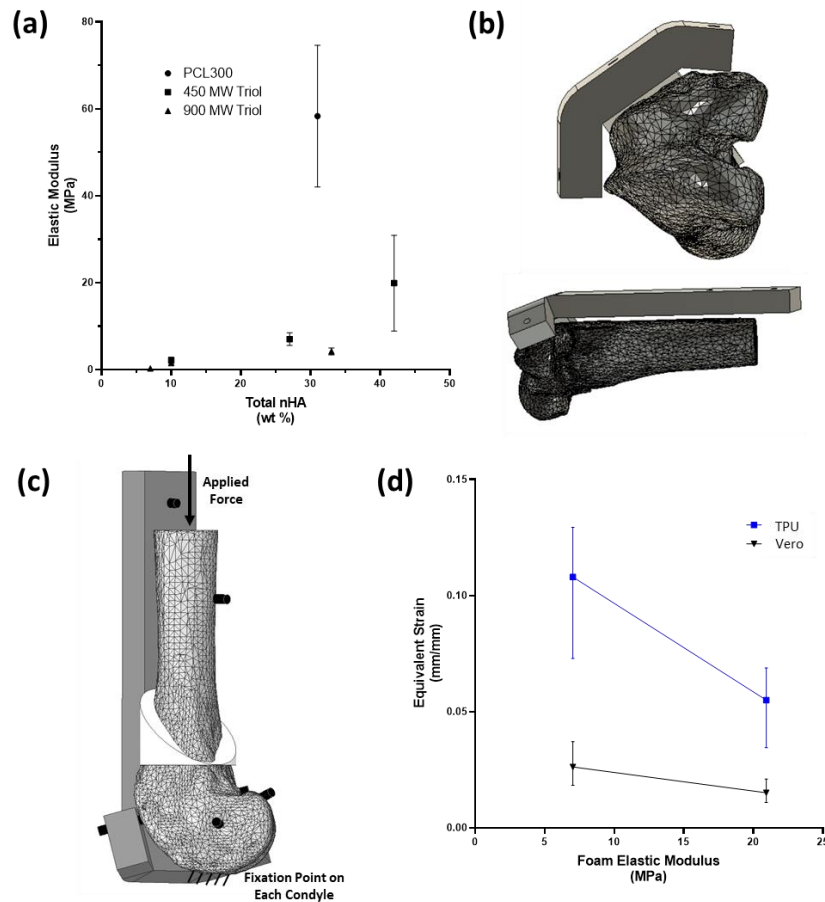
Figure 7.3. Mechanical testing of the nHA-PEUR foams and FE modeling of the weight-bearing metaphyseal defect predicted that median equivalent strains between 1.5-11% could be generated, within the foams, during gait. (a) The elastic moduli of the nanocomposite foams increased with increasing wt% nHA and decreasing polyol molecular weight (mean ± standard deviation). (b) The novel compliant fixation plate was digitally designed to fit a rat femur. (c) FE models of the foam-filled metaphyseal defect were created from a μCT scan of a rat femur. (d) The FE models predicted that the median equivalent strain, within the foam, would range from 1.5% to 11%, depending on the foam and fixator chosen (median ± interquartile range).

Another metaphyseal defect model of interest is the weight-bearing tibial slot defect model that our lab previously utilized to evaluate nHA-PEUR cements doped with slow-resorbing ceramic granules (CG, 85% β-TCP/15% nHA). In this model, the nHA-PEUR-CG cement maintained the tibial slot defect space throughout the trial and was infiltrated with new bone along the interface [14]. However, other groups have shown that CPCs, like Norian® SRS®, can eventually develop cracks throughout the cement when they are used to stabilize this stringent weight-bearing defect [15,16]. We hypothesized that the cause of this cracking was related to the fatigue strength of Norian® being lower than that of nHA-PEUR [17]. To predict the stress distribution within the different cements, an FE model geometry of the tibial slot defect was created from a µCT scan of a sheep tibia, and loading vectors (medial-lateral, anterior-posterior, axial) of (0 N,-30 N, -500 N) for standing and (0 N, -115 N, -2000 N) for gait were split 60:40 between the medial and lateral condyles [18] and applied to the proximal bone surface (**Fig. 7.4 (a)**). The mechanical properties assigned to the bone and cements are listed in **Table 7.2**. These simulations predicted that the Norian® and nHA-PEUR-CG cements would be exposed to median equivalent stresses up to 3.5 MPa and 2.9 MPa, respectively, during standing and gait (**Fig. 7.4 (b-c)**), while the surrounding bone would be exposed to median equivalent stresses up to 13.5 MPa (**Fig. 7.4 (d)**). Like the weight-bearing murine model, funding and group research interests shifted before the fatigue strengths of the CPC and nHA-PEUR-CG could be quantified by cyclic compression and before bones, purchased from a local butcher (Porter Road Butcher; Nashville, TN), could be cut, filled, and mechanically tested *ex vivo*.

Table 7.2. FE Model of Ovine Tibial Slot Defect - Mechanical Properties

Material	E_s (GPa)	ν
Cortical Bone[19]	17.5	0.30
Trabecular Bone[19]	1.4	0.30
nHA-PEUR-CG[14]	1.5	0.38
Norian CPC[20]	0.674	0.38
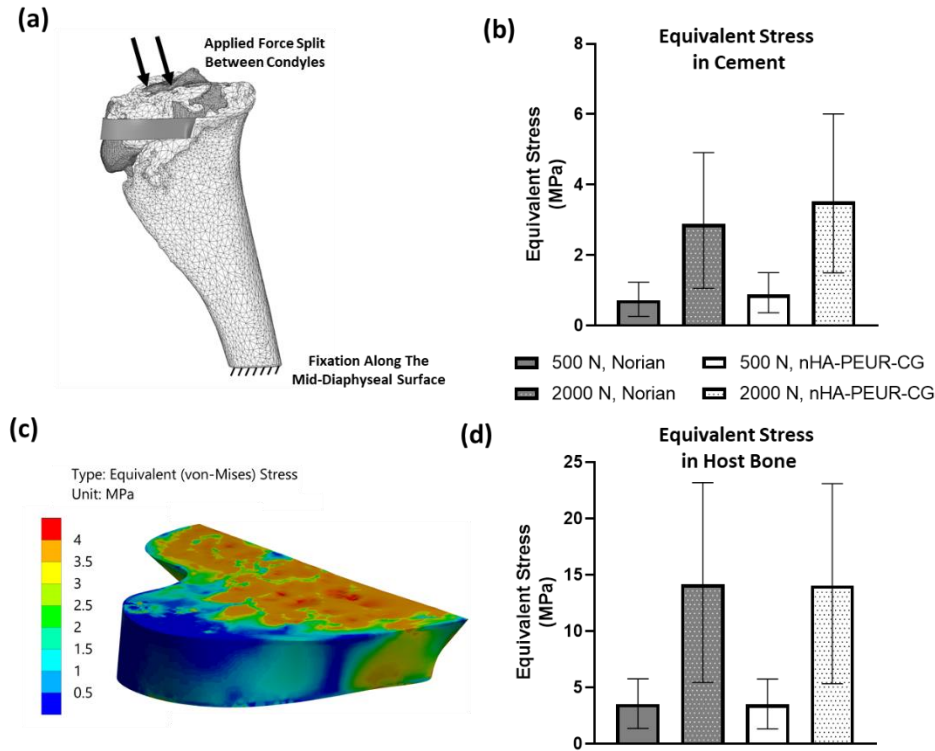
Figure 7.4. FE models of loaded tibial plateau slot defects predicted there being lower equivalent stresses in Norian CPC filled defects than in nHA-PEUR-CG composite grafts. (a) An FE model of the loaded defect was created from a μCT scan of a sheep tibia. (b) The simulations predicted there being higher equivalent stresses in the nHA-PEUR-CG composite than in the Norian CPC (median ± interquartile range) (c) A heat map of equivalent stress within the Norian CPC, under 2000 N load, revealed higher stresses concentrated below the loaded condyles. (d) The simulations predicted that the equivalent stress in the host bone will be minimally impacted by the cement chosen to fill the defect (median ± interquartile range).

7.2 Modifying polyphosphate nanoparticles to optimize bone growth

In **Chapter 4**, Ca-polyP nanoparticles were fabricated, analyzed, and used to induce bone growth and spinal fusion in mice. While these nanoparticles promoted significantly more bone growth and non-significantly more spinal fusion than autograft, efforts have yet to be made towards optimizing the Ca-polyP nanoparticles or towards determining whether polyP nanoparticles fabricated from other Group 2 metal chlorides can improve outcomes further.

In mammals, polyphosphates can be found in bodily fluids, including blood plasma and serum, and in cells, including osteoblasts, PBMCs, and fibroblasts, and these linear polymers range in length from a few phosphate molecules to several thousand residues [21–23]. While one study revealed that amorphous Ca-

polyP nanoparticles, fabricated from Na-polyP with an average chain length of 40 phosphate molecules, have the ability to increase intracellular ATP and stimulate human umbilical vein endothelial cell tube formation while amorphous Ca-polyP nanoparticles, fabricated from Na-polyP with an average chain length of 25 or fewer residues, do not [24], research has yet to be conducted on whether polyphosphate chain length impacts the bone formation induced by these amorphous Ca-polyP nanoparticles or whether there is an ideal Ca-polyP chain length for promoting bone growth or fracture repair.

To study this, Ca-polyP nanoparticles with various chain lengths would need to be fabricated and evaluated. Following the procedure in **Chapter 8.5**, Na-polyP glass was made by heating sodium phosphate monobasic in a furnace and quenching the polymerization reaction using a metal plate. This polydisperse Na-polyP was then fractionated with acetone to isolate Na-polyP salts with average chain lengths ranging from 10.1 to 146.4 residues, as measured by NMR (**Fig. 7.5**) [25]. While these Na-polyP salts were used to successfully fabricate Ca-polyP nanoparticles, the properties and efficacy of these nanoparticles has yet to be investigated. Additionally, both the Na-polyP fabrication and the acetone fractionation processes can likely be optimized to acquire as much Na-polyP, with the desired average chain length, as possible.

(b)

Sample	Average Chain Length (residues)
A	146.4
B	126.7
C	106.6
D	74.0
E	48.6
F	20.0
G	10.1
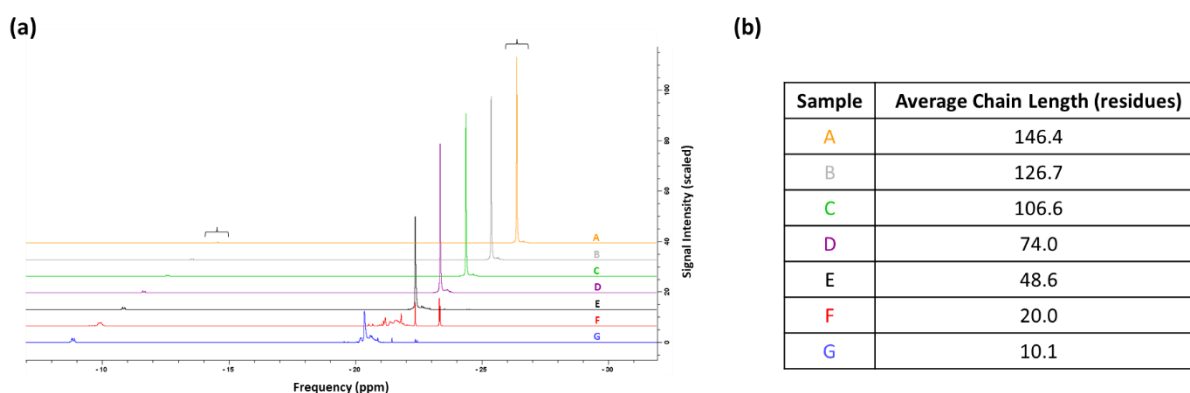
Figure 7.5. ^{31}P-NMR was used to quantify the average chain lengths of the fractionated Na-polyP samples. (a) The external phosphate (integral of peaks below left bracket) to internal phosphate (integral of peak below right bracket) ratio increased with increasing acetone addition (A to G). (b) These spectra were analyzed to reveal that Na-polyP samples with average chain lengths ranging from 10.1 to 146.4 residues can be fabricated in a furnace and isolated by acetone fractionation.

Another polyP nanoparticle property that should be investigated further is the counterion used during the fabrication process. Recent research has shown that amorphous Mg-polyP has the ability to upregulate cartilage associated genes, including collagen types 2A1 and 3A1, SOX9, and aggrecan *in vitro*, and that Mg-polyP can be incorporated into a hyaluronic acid matrix to form an artificial cartilage-like material [26–28]. In contrast, studies have shown that, relative to Ca-polyP, amorphous Sr-polyP nanoparticles can enhance hBM-MSC proliferation and osteosarcoma cell mineralization *in vitro,* and that poly (D,L-lactide-co-glycolide) (PLGA)-encapsulated Sr-polyP induces faster calvarial defect repair in rats than PLGA-encapsulated Ca-polyP and PLGA-encapsulated β-TCP [29]. However, these studies have not investigated whether Mg-polyP, Ca-polyP, Sr-polyP, or a combination would be best for promoting spinal fusion or fracture healing in general. Additional research could provide more clarity on these issues and could potentially lead to the development of personalized therapeutic strategies based on fracture severity, fracture location, and biological healing potential.

7.3 Using a bioreactor system to study the combined effects of ceramic content and compressive strain on hBM-MSC differentiation and ECM deposition

Finally, in **Chapter 5**, a model of TIBD was created using a resorbable bone-like scaffold and a perfusion bioreactor. We showed that this model could potentially be used to study cancer progression or therapeutic strategies, but, due to the modest scaffold resorption observed and group research interests shifting, this specific model was put on hold. An improved bioreactor system, using microfluidic flow chambers and optical analyses [30], spawned from this project, and current lab members are using this system to evaluate scaffold materials and study hematopoietic stem cells. However, while fluid flow can affect MSC differentiation and ECM deposition *in vitro* [31–33], hBM-MSC fate can also be impacted by compressive and tensile forces, and this improved microfluidic system can't be used to apply these mechanical loads or analyze their impact.

hBM-MSCs are mechanosensitive multipotent precursor cells that differentiate into bone forming osteoblasts and cartilage forming chondrocytes during fracture repair [34–36]. While hydrostatic pressure and

shear stress have also been shown to stimulate hBM-MSC differentiation, differentiation correlates most strongly with strain [37]. hBM-MSCs, cultured on electrospun PCL scaffolds in osteogenic medium and exposed to compressive strains up to 20% for up to 28 d, exhibited strain-enhanced chondrogenic differentiation, as measured by increased relative gene expression levels (aggrecan, collagen type II, and SOX-9) and increased glycosaminoglycan deposition (Alcian Blue staining), and strain-reduced osteogenic differentiation, as measured by decreased relative gene expression levels (collagen type I) and decreased mineral deposition (Alizarin Red S staining) [38]. In contrast, HA has been shown to promote osteogenic differentiation [39,40]. The combined effects of ceramic content and compressive strain on hBM-MSC fate have yet to been fully investigated.

To address this knowledge gap, hBM-MSCs were cultured statically or dynamically on 3D tissue-engineered bone constructs (0 - 21 wt% nHA, median yield strain of 5%) for 16 d. nHA significantly promoted mineral deposition, as measured by Alizarin Red S staining (**Fig. 7.6 (a)**), but did not promote significant GAG deposition, as measured by Alcian Blue staining (**Fig. 7.6 (b)**). Mineral and GAG deposition trended higher in the constructs cyclically loaded with an ElectroForce 5200 BioDynamic test system (5% global strain, 1 Hz, 1 h d-1, 14 d) than in the static controls, but the differences were not significant. FE models of the loaded tissue-engineered bone constructs (**Fig. 7.6 (c)**) calculated the median surface strains to be lower than the applied global strains (**Fig. 7.6(d)**), suggesting that the hBM-MSCs were exposed to a median equivalent strain less than 5%. To determine whether differences between the static and compression groups can be observed at higher compressive strains, composite scaffolds (e.g. foams) that can withstand larger cyclic compressive strains must be developed and trialed.
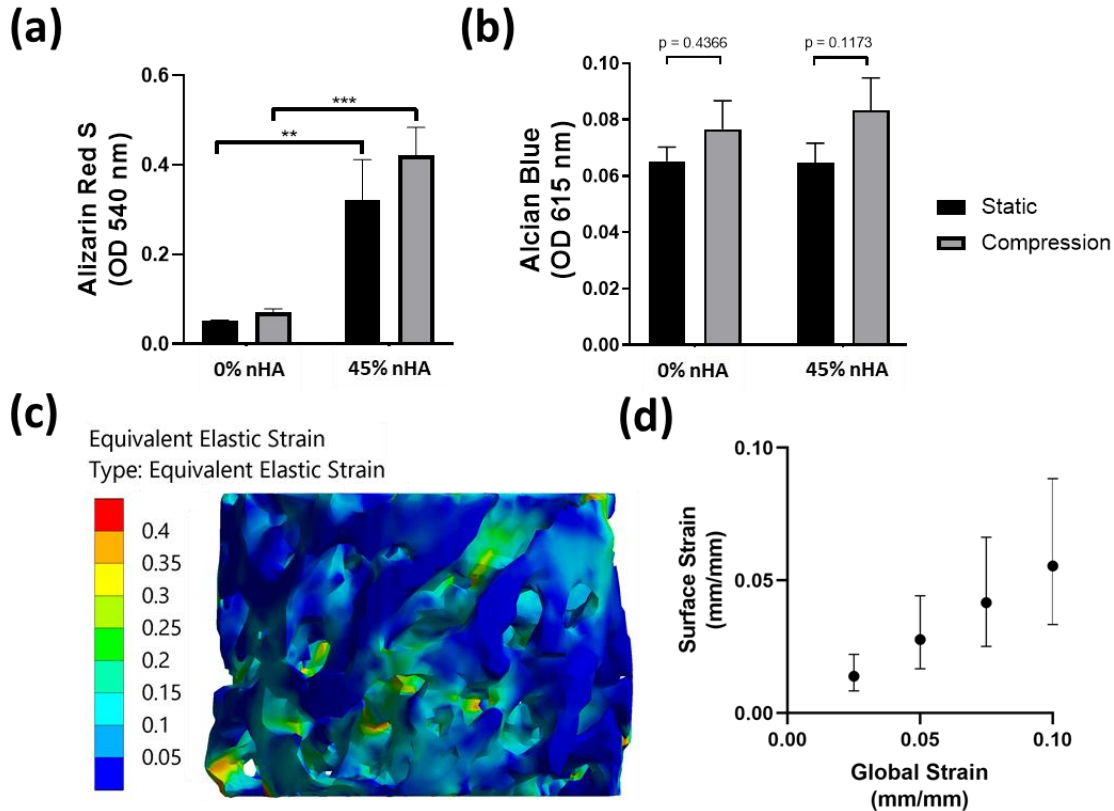
Figure 7.6. wt% nHA in the bone-like scaffolds affected hBM-MSC osteogenesis while compressive strain impacted osteogenesis and chondrogenesis. (a) Alizarin Red S staining was significantly higher in the 21% nHA group than in the 0% nHA group, and compressive loading non-significantly increased staining (mean ± standard deviation). (b) The wt% nHA did not affect Alcian Blue staining, and compressive loading non-significantly increased staining (mean ± standard deviation). (c) A representative heat map of the equivalent strains along the scaffold surface shows pockets of high and low strains throughout the scaffolds (10% global strain). (d) The equivalent strain along the surface of the scaffold is less than the global strain applied to scaffold (median ± interquartile range).

References:

1. Alford, A. I., Nicolaou, D., Hake, M. & McBride-Gagyi, S. Masquelet's induced membrane technique: Review of current concepts and future directions. *J. Orthop. Res.* (2020). doi:10.1002/jor.24978
2. Han, W. *et al.* Induced membrane technique: Advances in the management of bone defects. *Int. J. Surg.* **42**, 110–116 (2017).
3. Ebraheim, N. A., Martin, A., Sochacki, K. R. & Liu, J. Nonunion of distal femoral fractures: a systematic review. *Orthopaedic surgery* **5**, (2013).
4. Goff, T., Kanakaris, N. K. & Giannoudis, P. V. Use of bone graft substitutes in the management of tibial plateau fractures. *Injury* **44**, S86–S94 (2013).
5. Kugelman, D. *et al.* Complications and unplanned outcomes following operative treatment of tibial plateau fractures. *Injury* **48**, 2221–2229 (2017).

6. Claes, L. *et al.* Metaphyseal fracture healing follows similar biomechanical rules as diaphyseal healing. *J. Orthop. Res.* **29**, 425–432 (2011).

7. Uhthoff, H. K. & Rahn, B. A. Healing patterns of metaphyseal fractures. *Clin. Orthop. Relat. Res.* **No. 160**, 295–303 (1981).

8. Thormann, U. *et al.* Bone formation induced by strontium modified calcium phosphate cement in critical-size metaphyseal fracture defects in ovariectomized rats. *Biomaterials* **34**, 8589–8598 (2013).

9. Lu, S. *et al.* Resorbable nanocomposites with bone-like strength and enhanced cellular activity. *J. Mater. Chem. B* **5**, 4198–4206 (2017).

10. Hafeman, A. E. *et al.* Injectable biodegradable polyurethane scaffolds with release of platelet-derived growth factor for tissue repair and regeneration. *Pharm. Res.* **25**, 2387–2399 (2008).

11. Hafeman, A. E. *et al.* Characterization of the degradation mechanisms of lysine-derived aliphatic poly(ester urethane) scaffolds. *Biomaterials* **32**, 419–429 (2011).

12. Martin, J. R. *et al.* A porous tissue engineering scaffold selectively degraded by cell-generated reactive oxygen species. *Biomaterials* **35**, 3766–3776 (2014).

13. Oftadeh, R. *et al.* Hierarchical analysis and multi-scale modelling of rat cortical and trabecular bone. *J. R. Soc. Interface* **12**, 5–7 (2015).

14. Lu, S. *et al.* Settable polymer/ceramic composite bone grafts stabilize weight-bearing tibial plateau slot defects and integrate with host bone in an ovine model. *Biomaterials* **179**, 29–45 (2018).

15. Gisep, A. *et al.* Resorption patterns of calcium-phosphate cements in bone. *J. Biomed. Mater. Res.* **66A**, 532–540 (2003).

16. Gisep, A., Kugler, S., Wahl, D. & Rahn, B. Mechanical characterisation of a bone defect model filled with ceramic cements. *J. Mater. Sci. Mater. Med.* **15**, 1065–1071 (2004).

17. Harmata, A. J., Uppuganti, S., Granke, M., Guelcher, S. A. & Nyman, J. S. Compressive fatigue and fracture toughness behavior of injectable, settable bone cements. *J. Mech. Behav. Biomed. Mater.* **51**, 345–355 (2015).

18. Taylor, W. R. *et al.* The medial-lateral force distribution in the ovine stifle joint during walking. *J. Orthop. Res.* **29**, 567–571 (2011).

19. Novitskaya, E. *et al.* Recent advances on the measurement and calculation of the elastic moduli of cortical and trabecular bone: A review. *Theor. Appl. Mech.* (2011). doi:10.2298/tam1103209n

20. Van Lieshout, E. M. M., Van Kralingen, G. H., El-Massoudi, Y., Weinans, H. & Patka, P. Microstructure and biomechanical characteristics of bone substitutes for trauma and orthopaedic surgery. *BMC Musculoskelet. Disord.* **12**, (2011).

21. Morrissey, J. H., Choi, S. H. & Smith, S. A. Polyphosphate: An ancient molecule that links platelets, coagulation, and inflammation. *Blood* **119**, 5972–5979 (2012).

22. Schröder, H. C., Kurz, L., Müller, W. E. G. & Lorenz, B. Polyphosphate in Bone. *Biochem.* **65**, 296–303 (2000).

23. Wang, Y. *et al.* Progress and Applications of Polyphosphate in Bone and Cartilage Regeneration. *Biomed Res. Int.* **2019**, (2019).

24. Müller, W. E. G. *et al.* Role of ATP during the initiation of microvascularization: Acceleration of an autocrine sensing mechanism facilitating chemotaxis by inorganic polyphosphate. *Biochem. J.* **475**, 3255–3273 (2018).

25. Smith, S. A. *et al.* Polyphosphate exerts differential effects on blood clotting, depending

on polymer size. *Blood* **116**, 4353–4359 (2010).

26. Müller, W. E. G. *et al.* A bio-imitating approach to fabricate an artificial matrix for cartilage tissue engineering using magnesium-polyphosphate and hyaluronic acid. *RSC Adv.* **6**, 88559–88570 (2016).

27. Wang, X. *et al.* Artificial cartilage bio-matrix formed of hyaluronic acid and Mg2+-polyphosphate. *Eur. Cell. Mater.* **32**, 271–283 (2016).

28. Wang, X., Schröder, H. C. & Müller, W. E. G. Amorphous polyphosphate, a smart bioinspired nano-/bio-material for bone and cartilage regeneration: Towards a new paradigm in tissue engineering. *J. Mater. Chem. B* **6**, 2385–2412 (2018).

29. Müller, W. E. G. *et al.* Fabrication of amorphous strontium polyphosphate microparticles that induce mineralization of bone cells in vitro and in vivo. *Acta Biomater.* **50**, 89–101 (2017).

30. O'Grady, B. J. *et al.* Rapid prototyping of cell culture microdevices using parylene-coated 3D prints. *Lab Chip* **21**, 4814–4822 (2021).

31. Chen, G., Xu, R., Zhang, C. & Lv, Y. Responses of MSCs to 3D Scaffold Matrix Mechanical Properties under Oscillatory Perfusion Culture. *ACS Appl. Mater. Interfaces* acsami.6b10745 (2016). doi:10.1021/acsami.6b10745

32. Vetsch, J. R., Betts, D. C., Müller, R. & Hofmann, S. Flow velocity-driven differentiation of human mesenchymal stromal cells in silk fibroin scaffolds: A combined experimental and computational approach. *PLoS One* **12**, 1–17 (2017).

33. Yue, D. *et al.* The rate of fluid shear stress is a potent regulator for the differentiation of mesenchymal stem cells. *J. Cell. Physiol.* 1–8 (2019). doi:10.1002/jcp.28296

34. Lian, J. B. & Stein, G. S. Concepts of Osteoblast Growth and Differentiation: Basis for Modulation of Bone Cell Development and Tissue Formation. *Crit. Rev. Oral Biol. Med.* **3**, 269–305 (1992).

35. Carter, D. R., Beaupré, G. S., Giori, N. J. & Helms, J. A. Mechanobiology of skeletal regeneration. *Clin. Orthop. Relat. Res.* S41-55 (1998).

36. Lacroix, D., Prendergast, P. J., Li, G. & Marsh, D. Biomechanical model to simulate tissue differentiation and bone regeneration: Application to fracture healing. *Med. Biol. Eng. Comput.* **40**, 14–21 (2002).

37. Isaksson, H., Wilson, W., van Donkelaar, C. C., Huiskes, R. & Ito, K. Comparison of biophysical stimuli for mechano-regulation of tissue differentiation during fracture healing. *J. Biomech.* **39**, 1507–1516 (2006).

38. Horner, C. B. *et al.* Magnitude-dependent and inversely-related osteogenic/chondrogenic differentiation of human mesenchymal stem cells under dynamic compressive strain. *J. Tissue Eng. Regen. Med.* **12**, e637–e647 (2018).

39. Rogina, A. *et al.* Human mesenchymal stem cells differentiation regulated by hydroxyapatite content within chitosan-based scaffolds under perfusion conditions. *Polymers (Basel).* **9**, 1–17 (2017).

40. Hu, J., Zhou, Y., Huang, L., Liu, J. & Lu, H. Effect of nano-hydroxyapatite coating on the osteoinductivity of porous biphasic calcium phosphate ceramics. *BMC Musculoskelet. Disord.* **15**, 1–11 (2014).

CHAPTER 8: SUPPLEMENTAL PROCEDURES

This section includes supplemental procedures relevant to the work contained in the previous chapters. These procedures are not official standard operating procedures (SOPs), and changes or improvements to these procedures may be made for future projects. To make these procedures more useful, some specific steps or details were replaced with procedural explanations or suggestions. Text written between brackets or parentheses is commentary and should not be typed into the software packages mentioned.

8.1 Creating FE and CFD models from μCT scans

8.1.1 Purpose
The purpose of is protocol is to outline how μCT scans can be used to create FE or CFD models. FE models may be useful for predicting stress or strain distributions, and CFD simulations may be useful for predicting WSS or fluid velocity distributions.

8.1.2 Materials and equipment
- A computer with Scanco's μCT software (e.g. a computer used to run μCT scans), a Windows computer with Putty and Xming, or a macOS computer with XQuartz is required to access the required software packages for converting the μCT scan into a surface mesh (.stl).
  - Refer to **Supp. Proc. 8.2** for details on how to access and evaluate μCT scans from remote computers
- A computer with MicroCT FTP is required to download the .stl file
- A computer with MeshLab is required to smooth and repair the .stl file
- A computer with MATLAB is required to convert the .stl file into an ACIS solid volume (.sat)
- A computer with Ansys is required to create and run the FE and CFD simulations
  - At least 16GB RAM and 500 GB hard drive space are recommended

8.1.3. Creating a .stl file from a μCT scan
The following sections focus on creating a .stl file directly from a μCT scan. Other parameters will depend on the sample being scanned (fixed bone, dry scaffolds, etc.), but the μCT voxel size should be small enough to resolve the desired bone or scaffold architecture.

8.1.3.1 Segmenting the bone from the μCT scans
1. Open the Scanco μCT evaluation module or type "uct_evaluation" into Putty
2. Contour the sample to include the entire region of interest
3. Threshold the sample, using the built-in BV only script (Script 6), to create a segmented .AIM file (SEG.AIM) that only includes voxels within the defined threshold range
   - Apply an appropriate Gaussian noise filter, if needed
   - Select a lower threshold so that the region of interest is visible in the preview plane and maximize upper threshold

8.1.3.2 Creating the .stl file from the segmented .AIM file
1. Open the DECterm (listed under Applications) or start a new Putty session
2. Input "ipl" into the DECterm input field to access Scanco's Image Processing Language (IPL) script-based analysis tool
    - Input "help" to view common commands
    - Input "help" followed by command name (e.g. "help read") to view input and output details for that command
3. Input "read" to read in the SEG.AIM file generated in **Section 8.1.3.1**
    - Input = the variable name to which the file will be assigned (define this to be "a")
    - Filename = the entire file path of the SEG.AIM file (e.g. "dk0:[microct.data.00019165.00031854]c0028478_seg.aim;11")
4. Input "cl_rank_extract" to separate the sample volume (volume rank 1) from any disconnected objects or debris (volume rank > 1)
    - Input = the variable name defined in Step 3 ("a")
    - Output = the variable name assigned to the extracted volume (define this to be "b")
    - Accept the default options for the remaining fields (continue pressing the enter key)
5. Input "stl" to create the .stl file
    - Input = the variable defined in Step 4 ("b")
    - Output = [Leave default/blank]
    - Stl_output_file = the entire file path for .stl file (e.g. "dk0:[microct.data.00019165.00031854]c0028478_seg_11.stl")
    - Binary_file = [Leave default/blank]
    - Stl_dre_tet_mode = [Leave default/blank]
    - Gobj_filename = [Leave default/blank]
    - Peel_iter = [Leave default/blank]
    - Ip_sigma = [Leave default/blank]
    - Ip_support = [Leave default/blank]
    - Ip_threshold = [Leave default/blank]
    - Nr_ave_iter = [Leave default/blank]
    - T_dir_radius = [Leave default/blank]
    - Epsilon = [Leave default/blank]
    - Size_image = [Leave default/blank]
    - Scale_image = "1"
    - Edges = [Leave default/blank]
    - Nr views = [Leave default/blank]

    - Depending on the size of the scan, creating the .stl file can take up to a few hours, and the DECterm window must remain open throughout
    - Immediately after the command is issued, the .stl file will appear in the folder listed in the file path, but the file will be incomplete (the file size will be small)
    - Once this process if finished, the DECterm will display a line of code stating that the file was successfully created.

8.1.4. Converting the .stl surface mesh into a .sat solid volume
    The following steps are included in this procedure, because Ansys SpaceClaim intermittently has issues importing and converting .stl files into the solid bodies required for the simulations. Importing the .stl file can be prohibitively slow or the software can incorrectly scale the geometry. Converting the .stl surface mesh into a .sat solid volume circumvents these problems.

1. Open MicroCT FTP and log onto the CT server
   - You will need the server's IP address, username, and password
2. Download the .stl file from the folder defined during the .stl file creation step
3. Open MeshLab and import the .stl file
   - Allow vertices to be unified (default option)
4. Remove isolated pieces (wrt diameter)
   - Repeat and adjust diameter % until only 1 component remains
5. Remove faces from non-manifold edges
6. Remove duplicate faces
7. Remove zero area faces
8. Close holes
   - Accept the default size
9. Reconstruct the mesh, using the Screened Poisson Surface Reconstruction tool, to smooth the surface and close any remaining holes
   - Initially try the default settings.
   - Change the Reconstruction Depth if too much detail is lost or if face reduction using the Quadric Edge Collapse Decimation tool (Step 11) creates a poorly formed mesh (jagged edges, skinny triangles, etc.). Depth >8 results in more faces and more detail while depth <8 results in fewer faces and less detail.
   - If the mesh can't be reconstructed due to the presence of null or non-manifold edges, repeat Steps 5-9. These Steps may need to be repeated a few times before the mesh can be repaired and smoothed.
10. Remove isolated pieces (wrt diameter) a second time to remove any disconnected bodies that may have formed during the reconstruction step.
11. Halve the number of faces using the Simplification: Quadric Edge Collapse Decimation tool
    - Set quality threshold = 0.5
    - Preserve boundary of the mesh
    - Preserve normal
    - Preserve topology
12. Repeat Steps 10 and 11 until the final surface mesh has 25-50 K faces
    - Ansys may communicate errors if there are more than 50 K faces
    - Repeat the Screened Poisson Surface Reconstruction if the final surface mesh doesn't mimic the original surface mesh very well
13. Select the final .stl file from the layer dialog on the right and export it from MeshLab
    - Save the file as a .stl file (not .ply)
14. Move the .stl file into the folder typically used for MATLAB or change the file directory
15. Download the STL to ACIS SAT conversion script (see references)
16. Run the script following the instructions in the Read Me file
    - If a .sat file can't be generated, there is a problem with the mesh (non-manifold faces, holes, etc.). Repair the mesh following Steps 3-8.
    - Once this process if finished, the MATLAB window will display a line of code stating that the file was successfully created.

8.1.5. Creating the FE and CFD model geometries in Ansys SpaceClaim

SpaceClaim is Ansys's built-in computer-aided design (CAD) module, and it can be used to create the system geometry system required for the simulations. Excellent tutorials are available on the SpaceClaim website or on YouTube, and, in the following steps, I will highlight some of the tools I found most useful.

1. Open SpaceClaim and import the .sat file by opening the file

- Importing the file may take a few minutes
- SpaceClaim can also be opened from Ansys Workbench, but it may be easier to keep geometry files (.scdoc) organized if the files are created first and then linked to the Workbench project.

2. Using the Move tool, move and rotate the solid body so that it is positioned at the global origin (x = 0, y = 0, z = 0) and aligned with one of the axes.
    - It may be beneficial to repeat this step after the final geometry is created
    - The Move tool can also be used to create evenly spaced serial copies of a feature
3. If required, import additional solid bodies (Assembly → Part → File)
    - Incorporating multiple objects into one assembly helps keep the system organized
4. Use the Split Body tool (Design → Intersect → Split Body) to remove any geometric features that should not be included in the final simulation
    - Edges can be used as the cutting object or you can create and use a plane
    - Use the Measure tool, as needed, to measure the distances between different geometric features (edges, vertices, and faces), bodies, or planes
5. Use the Combine tool (Design → Intersect → Combine) to merge multiple solid bodies or to use one solid body as a cutter for splitting apart a second solid body (similar to Split Body)
    - If you get the "Unable to intersect bodies" error, move one of the solid bodies, slightly, until the cuts can be made
6. Use the Fill tool to fill any unwanted holes or to fill a 2D sketch (circles, squares, etc.)
7. Use the Pull tool to extrude any features or to turn 2D shapes into 3D bodies
    - The Pull tool can also be used to cut into a solid body or merge solid bodies
    - Chamfered or rounded edges can also be created using the Pull tool.
8. If needed (e.g. for CFD models), create a fluid volume using the Volume Extract tool
    - Select the inlet/outlet faces to enclose/cap the region
    - Select an internal face as the seed face
    - The volume extract process can take a few minutes if there are complex geometries
    - The resulting fluid volume will appear purple. To confirm that the Volume Extract was successful, hide all other bodies and view the volume as a wireframe
    - Create named sections ("inlet", "outlet", "walls", etc.), because Fluent will automatically recognize these names (**Section 8.1.7**)
9. Name any geometric features by selecting them in the Structure pane and renaming them
    - Naming a selection of faces, edges, or vertices can be done by creating and naming a Group (Groups pane → Create Group) and selecting the desired features
10. Delete any unwanted bodies by selecting them in the Structure pane or design window and deleting them
    - If you want to keep objects in the geometry file but prevent them from being included in the simulations, they can be suppressed by right-clicking the object in the Structure pane and selecting the "Suppress for Physics" option
11. Save the .scdoc file

8.1.6. Creating and running Static Structural simulations

1. Open Ansys Workbench
2. Double click Static Structural from the Toolbox
3. Double click Engineering Data and add material properties, if needed
4. Right click Geometry to import the SpaceClaim geometry from **Section 8.1.5**
5. Double click Model to open up Ansys Mechanical
    - It may take a few minutes for the geometry to import and for automatic connections to form

- The software may act as non-responsive, especially if you are replacing the geometry from a previous simulation, but Mechanical will eventually allow you to proceed
6. Expand the Geometry section and assign materials to each part
7. If needed, change the connections tolerance values to define which bodies contact each other
    - Right click Connections and select Create Automatic Connections after changing these tolerance values
    - You should see all potential interactions between bodies. These bodies do not need to be touching at time = 0, but the software will check to see if the contact pairs are touching at every iteration.
8. Change contact pairs from bonded to fictional, if needed
    - Higher Normal Stiffness may be required for compliant bodies contacting hard bodies, because the solid bodies may intersect if contact stiffness is too low
    - Change Pinball Region, if needed, to make sure that the software checks whether geometric bodies are in contact with each other throughout the simulation
9. Update the mesh properties and methods, as needed
    - Change global mesh properties to Quadratic, if needed. Quadratic elements are thought to be better for FE compression simulations.
    - Add Hex Dominant mesh methods for simpler geometries. Patch Independent tetrahedral mesh methods may be needed for more complicated geometries, but hexahedral elements are thought to be best for FE compression simulations.
    - Set body and contact sizing, if needed
10. Add the force and fixed support (right click Static Structural)
    - Change Scoping Method to Named Selection if you named groups in SpaceClaim
    - Force can be defined by x, y, and z components
11. Change solver settings to Direct, if needed
    - You may not need to do this, but the Iterative Solver may not be as efficient or may have issues solving the simulation
    - The Direct solver requires more RAM and hard drive space
12. Right click Mesh and select Update
    - This can take 30+ minutes
    - If the mesh exhibits an error (not a warning), try to right click Mesh and select Update again
    - If the mesh still doesn't form try changing mesh parameters (refinement, size, etc.)
    - If the mesh still doesn't form, you may need to modify the Geometry (**Section 8.1.5**)
13. Once the geometry has meshed, right click Solution and select Solve
    - If the solver quits, search the Solution Output for "error." The ENORM error signals that mesh parameters will need to be changed and that remeshing is required. Other errors may signal that there isn't enough RAM or hard drive space.
    - Once the "Solving the mathematic model" and "Overall Progress…" bars begin cycling, the simulation will attempt to converge. Convergence can be tracked by changing the Solution Output to Force Convergence and watching the Force Convergence and Force Criterion lines
14. Once the simulation has solved, add results by right clicking Solution and choosing Insert
    - We looked at equivalent strain, maximum principal strain, minimum principal strain, and max shear strain, but you can select other built-in results or add user defined results
    - You can edit the legend vales between the maximum and minimum values, if needed
15. Export result .txt files by right clicking the evaluated result
    - You may want to change export options to include node locations (Tools → Options → Mechanical → Export → Include Node Location)

16. Save videos by selecting the save video icon in the graph/animation pane at the bottom
    - 20 frames for 4 seconds is probably OK
    - The video will replicate what is in the main frame, so zoom in/out accordingly
17. Save images by selecting the Image to File… option

8.1.7. Creating and running Fluent simulations
1. Open Ansys Workbench
2. Double click Fluid Flow (Fluent) from the Toolbox
3. Right click Geometry to import the SpaceClaim geometry from Section **8.1.5**
4. Double click Mesh to open the meshing module
    - It may take a few minutes for the geometry to import (progress bar lower left)
    - The software may act non-responsive, especially if you are replacing the geometry from a previous simulation
    - The only Geometry should be the fluid volume
5. Right click Mesh and add a new tetrahedral method, if needed
    - Linear tetrahedral elements are OK for fluid flow
    - A Patch Independent method may be better for complicated geometries
6. Right click Mesh and select Update or Generate Mesh (may not matter)
    - If the meshing fails, try changing mesh parameters (refinement, size, etc.)
    - Depending on the complexity of the fluid volume, meshing can take a long time to complete
7. Close/X-out of the Mesh module and double-click Setup to open Fluent
    - Double-click items in Fluent to enter values, materials, etc.
8. Change the fluid material by opening Materials→Fluid→(Whatever is Listed).
    - If adding a common fluid, click on Fluent Database, and select the desired fluid (e.g. water-liquid (h2o<l>)
    - To create your own fluid, change the listed properties (density and viscosity), change the name, and choose Change/Create
9. Assign the fluid material to the fluid volume by opening Cell Zone Conditions → Fluid → volume_volume
10. Change the inlet velocity by opening Boundary Conditions→Inlet→inlet (velocity-inlet)
11. Keep the outlet Gauge Pressure = 0, if true for your system
12. Keep walls stationary and no slip
13. Change the convergence criteria to 0.00001 for all residuals by clicking Solution → Monitors → Residual.
    - Even if the simulation doesn't "converge", it needs to plateau. Increase the number of iterations, if needed.
14. Run the simulation by opening Solution→Calculation Activities→Run Calculation
15. Once it solves, close/X-out of Solution and double-click the Results module
    - The results module is where you can make figures and/or export data
    - Contours are best for wall shear stress or pressure
    - Streamlines are best for fluid velocity
    - To save an image, fit the image to the screen and click on the camera icon. To change the background, right click on the View window and select Viewer Options)

8.1.8. References
1. Kirana, K: Reconstructing Solid Model from 2D Scanned Images of Biological Organs for Finite Element Simulation
    - https://knolskiranakumarap.wordpress.com/2011/07/03/reconstructing-solid-model-from-2d-3rc2kfwq179j2-5/

- I moved away from many of these steps, but I wanted to give credit to this document for motivating and guiding my initial trials
2. Kumara, K. P. Extracting three dimensional surface model of human kidney from the Visible Human Data Set using free software. *Leonardo Electron. J. Pract. Technol.* **11**, 115–126 (2012).
    - The published version of the above document, but some details are slightly different
3. Adam, A. STL to ACIS SAT conversion, MATLAB Central File Exchange. (2020).
    - https://www.mathworks.com/matlabcentral/fileexchange/27174-stl-to-acis-sat-conversion
    - This is the MATLAB script that can be used to convert .stl files to .sat files

---

8.2   Accessing µCT scans from remote computers and evaluating bone morphometric properties
    8.2.1 Purpose
    The purpose of is protocol is to outline how to access µCT scans from remote computers and how to evaluate the bone morphometric properties from these scans. This protocol is only applicable to Scanco scanners. If you can find a manual for your scanner, there will likely be other useful commands listed.

    8.2.2 Definitions
- .RSQ is the raw scan data
- .ISQ is the entire image stack
    - This file can be reconstructed from a .RSQ file using the uct_reconstruction command
- .AIM is the image stack of the contoured region of interest
    - This file is not thresholded and remains in grayscale
- SEG.AIM is the thresholded image stack of the contoured region of interest
    - This file is binary (black and while), not grayscale
- .GOBJ is the set of contour loops

    8.2.3 Materials and equipment
- Windows computer with Pulse Secure, Xming, Putty, and MicroCT FTP
    - Pulse Secure is a virtual private network (VPN) tool that may be needed to access the CT server
        - Pulse Secure pairs with Duo Mobile on your phone. The secondary password "push" will trigger a notification on your phone for you to accept.
    - Xming is needed to open and view a local session (DECterm)
        - https://sourceforge.net/projects/xming/
        - Putty will not function without Xming running (Xming may create the windows on the screen)
    - Putty is needed to access the CT server
        - https://www.chiark.greenend.org.uk/~sgtatham/putty/
        - You will need the server's IP address, username, and password
        - Multiple Putty windows/sessions can be running at the same time
    - MicroCT FTP can be used download or upload files off/on the CT server, if needed
        - The .txt evaluation files should be in the same directory as the other scan files (.ISQ, .AIM, etc.)
        - Files can be uploaded to the server (under "Options", check "Enable Uploads")

- MacOS computer with Pulse Secure, Xquartz, and Fetch
  - Pulse Secure is a virtual private network (VPN) tool that may be needed to access the CT server
    - Pulse Secure pairs with Duo Mobile on your phone. The secondary password "push" will trigger a notification on your phone for you to accept.
  - Xquartz is needed to open and view a local session (DECterm)
    - https://www.xquartz.org/
    - Terminal will be used to access the CT server, but it can't be used without Xquartz running
  - Fetch can be used to download or upload files off/on the CT server, if needed
    - https://fetchsoftworks.com/
    - Click on the arrow showing additional information to get into the folder where the actual data is stored.

- Good Wi-Fi or an ethernet cable connected to your router
  - Pulse Secure may not be very stable

8.2.4.A. Setting up and opening Putty (Windows)
1. Open Xming
   - It will appear in the lower right-hand corner of your taskbar (no windows will open)
2. Open Putty and Enable X11 forwarding (Category: Connection → SSH → X11).
3. Fill in the Category: Session fields
   - Host Name (or IP address)
   - Port is 22
   - Connection type is SSH
   - If you want to save the Host Name/IP address, name it under Saved Sessions) and press the Save button. This allows you to press load next time you open Putty.
4. Press Open at the bottom of the window
   - You will get the error "Network error: Network error: Connection timed out" if you aren't running Pulse Secure or if something else is wrong with the connection
   - It will take some time (feels long), but a window saying "PuTTY Security Alert… Do you want to continue with this connection?" will appear. Click on the Yes button. If you don't press Yes fast enough, you will get a "PuTTY Fatal Error…" Repeat Step 4 if this happens but select Yes more quickly.
5. When it prompts for "login as:", input the username and hit the enter key
6. When it prompts for the password, input the password followed by the enter key
   - The text will not appear in the window when you type, but Putty will register it

8.2.4.B. Setting up and opening Terminal (macOS)
1. When it prompts for "login as:", input the username and hit the enter key
2. Open Xquartz
   - It will appear in your taskbar, but a window will not open up
3. Open Terminal
4. Write in/ copy & paste:
   - ssh -oKexAlgorithms=+diffie-hellman-group1-sha1 -oHostKeyAlgorithms=+ssh-dss [*****************] Y
     - [*****************] is the scanner name @ the IP adress (e.g. microCT50@IP Address)
   - Maintain proper spacing or else you will get an error
5. When it prompts for the password, input the password followed by the enter key

- The text will not appear in the window when you type, but Putty will register it

8.2.5 Evaluating bone morphometric properties
1. Input "uct_evaluation" into Putty or Terminal
    - You may need to adjust the sizes and positions of the windows to view all the options/tabs (if you see unusual white space). I recommend shrinking the size of the window(s) until you have vertical and horizontal scroll bars. You can also adjust your monitor's Display Settings (100% text/app scaling works best)
2. Find your sample's .ISQ file by typing the sample name or number in the filter field.
    - Click on the .ISQ and press OK.
    - The .ISQ can be selected using the .ISQ dot in the bottom left of the window or by using the All Files dot.
    - You will get a Mu_scaling error if you open a SEG.AIM file instead.
3. If the scan has already been contoured, load the GOBJ (File → Load .GOBJ) and go to Step 6
4. If you need any scan parameters (e.g. voxel size, intensity, etc.), view the Header Information (File → Header Information)
5. Contour the sample using the drawing tool
    - The program will not let you contour if CapsLk is on
    - Counterclockwise includes the region enclosed within the drawn shape
    - Contour slices at various intervals within your region of interest to utilize built-in segmentation tools (morph, iterate forward, etc.)
6. Select the Contour (C…) tab to morph, iterate forward, etc.
7. Select the Threshold (T…) tab to apply thresholds and execute the evaluation script
    - The built-in BV/Density only Bone Eval. script (Script 6) will provide BV, TV, and BV/TV while the built-in BV/TV. The Bone Trab. Morphometry script (Script 5) will provide everything.
    - Click on the "Default VOI" button to make sure the white box encompasses all of the green contours
    - Select a lower threshold used previously (e.g. a previously published value, value that shows the entire bone architecture) and toggle between Preview and Grayscale to confirm
8. Select Start Evaluation
    - The speed of the evaluation is dependent on the server and on the number of evaluations being run at the same time
    - You can run multiple evaluations at once if you are evaluating different samples/scans
    - The program will prompt you to save the .GOBJ. You can also save a .GOBJ by selecting File → Save .GOBJ (it will save it as a new version)

8.2.6 Other useful Putty/Terminal tools
- Input "vue" into Putty or Terminal to view files in the Session Manager
    - Navigate directories to find files of interest
    - View → Show:All Versions to view all analysis and SEG.AIM files
    - Directories can be created (Utilities → Create Directory)
- Input "uct_3d" into Putty or Terminal to view .ISQ or .AIM files in the 3D Viewer
    - 2D cut-planes can be created using the "Subdim" menu

8.3 Creating μCT scan overlays using Scanco's IPL

8.3.1 Purpose

The purpose of is protocol is to outline how to overlay μCT scans using Scanco's IPL This protocol applies to overlaying SEG.AIM files and may be helpful for visualizing samples before and after trials (like **Chapter 5**).

8.3.2 Materials and equipment

- A computer with Scanco's μCT software (e.g. a computer used to run μCT scans), a Windows computer with Pulse Secure, Putty and Xming, or a macOS computer with Pulse Secure and XQuartz is required to access and use Scanco's software.

8.3.3 Opening IPL

1. Find the Session Manager window or create one by typing "vue" in a remote DECterm (Putty window).
2. Click on View → MicroCT:Data to view all of the scan directories
3. Open a second DECterm window or start a second remote access session (to create a second Putty window)
4. Type "IPL" into the DECterm

8.3.4 Preparing scans for overlay

1. Input "read" to read in the SEG.AIM file generated
   - Input = the variable name to which the file will be assigned (define this to be "a")
   - Filename = the entire file path of the SEG.AIM file (e.g. "dk0:[microct.data.00019165.00031854]c0028478_seg.aim;11")
2. Input "cl_rank_extract" to separate the sample volume (volume rank 1) from any disconnected objects or debris (volume rank > 1)
   - Input = the variable name defined in Step 1 ("a")
   - Output = the variable name assigned to the extracted volume (define this to be "b")
   - Accept the default options for the remaining fields (continue pressing enter key)
3. Input "bounding_box" to remove the empty space around the sample and reduce the file size
   - The input is the variable defined in Step 2 ("b")
   - The output is a new variable (define this to be "c")
4. Input "write c [Name of New File name, e.g. Segmented AIM File Name_CL_BB.AIM]" to save the edited SEG.AIM to the server
5. Repeat Steps 1-4 for the before and after scans

8.3.5 Create the orientation alteration command file (TMAT.DAT file)

1. Open the 3D viewer twice and put the two windows next to each other on the screen
   - You can also input "uct_3d" into Putty or Terminal
2. Select the desired Sample Number, view all the associated files (not just the original segmented AIM files), and open the before and after scan's bounding box SEG.AIM files
3. Elevate both scaffolds +/- 90° to view the top or bottom
   - It may be easier to manually line up the scans from this viewpoint
4. Rotate the after scan until its orientation is very similar to the before scan
5. Elevate both scaffolds back to 0°
   - The before scan should now have 0° Rotation, Elevation, and Roll and the after scan should have X° Rotation
6. Elevate and Roll the after scan until its orientation is similar to the before scan
7. Record the after scan's Rotation, Elevation, and Roll

8. Convert the after scan's Rotation, Elevation, and Roll into radians
9. In IPL, input "register" to create the orientation alteration command file (can take hours)
   - in 1 = The file name of the before scan SEG.AIM (after bounding box)
   - gobj...1 = [Leave default/blank]
   - in 2 = The file name of the after scan SEG.AIM (after bounding box)
   - gobj...2 = [Leave default/blank]
   - tmat_file_name = "[******]_TMAT.DAT" where ****** is the file name of the after scan SEG.AIM without the "SEG.AIM"
   - orientation search = 2, if orientations are already close, or 1, if orientations aren't close
   - initial rotation = [Leave default/blank if orientations are close], or input Roll, Elevation, and Rotation from Step 8 (Roll = x, Elevation = y, Rotation = z)
   - initial translation = [Leave default/blank]
   - delta rotation = [Leave default/blank]
   - delta translation = [Leave default/blank]
   - resolution scanning = [Leave default/blank]
   - delta scaling = 1 0.1 0.02 (all separated by a space)
   - weight_gobj... = [Leave default/blank]
   - tolerance = [Leave default/blank]
   - min_corr_coeff = [Leave default/blank]
   - min_method = [Leave default/blank]
   - object_func = [Leave default/blank]
   - mac_nr_iter = [Leave default/blank]
   - output_option = 2

8.3.6 Transform the after scan and create the overlay
1. Input "read" to read in the before scan SEG.AIM file (after bounding box)
   - Define the read in variable as "a"
2. Input "read" to read in the after scan SEG.AIM file (after bounding box)
   - Define the read in variable as "b"
3. Input "transform" to align the after scan with the before scan
   - in = "b"
   - out = "c" [another arbitrary letter]
   - tmat_file_name = TMAT.DAT file from **Section 8.3.5**
   - el_size_min_out = [Leave default/blank]
   - turat_invert = [Leave default/blank]
4. Input "bounding_box" to remove the empty space around the transformed sample
   - The input is the variable defined in Step 3 ("c")
   - The output is a new variable (define this to be "d")
5. Input "set value"
   - The input is the before scan SEG.AIM file ("a")
   - Set the value to 1
   - Accept all other default options
6. Input "set value"
   - The input is the transformed after scan SEG.AIM file ("d")
   - Set the value to 2
   - Accept all other default options
7. Input "concat" to combine/overlay the two scans
   - The first input is the before scan SEG.AIM file ("a")

- The second input is the transformed after scan SEG.AIM file ("d")
- The output is a new variable ("e")
- Accept all other default options
8. Input "bounding_box" to remove the empty space around the concatenated sample
    - The input is the variable defined in Step 7 ("e")
    - The output is a new variable (define this to be "f")
9. Input "write f [Name of New File, e.g. ...._Overlay.AIM]" to write the new AIM file

8.3.7 Threshold the regions that contain before only, after only, or overlapping regions
1. Input "read" to read in the Overlay.AIM file
    - Define the read in variable as "a"
2. Input "threshold"
    - input = "a"
    - output = "b"
    - lower_in_per_aut_al = "1" for the before scan only, "2" for the after scan only, or "3" for the overlapping regions
    - upper_in_perm_aut_al = "1" for the before scan only, "2" for the after scan only, or "3" for the overlapping regions
    - value in range = [Leave default/blank]
    - unit = 5
3. Input "bounding_box" to remove the empty space around the thresholded sample
    - The input is the variable defined in Step 2 ("b")
    - The output is a new variable (define this to be "c")
4. Input "write c [Name of New File, e.g. ...._Before.AIM or ... After.AIM]"
5. If needed, measure the threshold sample's "bone volume" by inputting "vox_scanco_param"
    - The input variable is "c" from Step 4
    - Sample volume is listed as ov in the command output
6. Repeat Steps 2-5, if needed, to create and analyze thresholded AIM files for the before, after, and overlapping regions
7. If needed, view the thresholded AIM files using the 3D viewer
    - The thresholded before, after, and overlay AIM files from **Section 8.3.7** can be viewed separately or at the same time (the Overlay.AIM file from **Section 8.3.6**)

8.4   Fabricating ceramic-poly(ester urethane) foams
    8.4.1 Purpose
    The purpose of is protocol is to outline how to fabricate ceramic-poly(ester urethane) foams. This procedure was used to make the nHA-PEUR foams discussed in **Chapter 7**. This procedure has not been optimized, and additional research is required to determine whether this procedure can be used to make ceramic-PTKUR foams with evenly distributed and open pores.

    8.4.2 Reagents
    - nHA or Ca-polyP
    - lysine triisocyanate (LTI)
    - 300-900 molecular weight (MW) polyol
    - Calcium stearate

- Water
- Tegaoamin® 33
- Turkey Red Oil, if needed
- Iron (iii) acetylacetonate (FeAA) catalyst, if needed

8.4.3 Materials and equipment
- SpeedMixer and polypropylene mixing containers (FlackTek, Inc.; Landrum, SC)
- 80 °C vacuum oven
- 50 °C oven
- 1 mL syringe without the needle
- Syringe needle
- 5 mL LDPE sample vials
- Razor blade

8.4.4 Making ceramic-LTI prepolymer
1. Calculate the ceramic and LTI needed for the prepolymer
    - The prepolymer may be too tacky if > 65 wt% ceramic
2. Dry the ceramic at 80 °C under vacuum for at least 48 hours before use
3. Add the LTI to the mixing cup
    - It is easier to remove excess isocyanate before adding the ceramic
4. Add the ceramic to the mixing cup
5. Mix the prepolymer for 1 min at 3500 RPM
6. Repeat Step 4 10 times (10 min total)
    - To "prevent overheating" (temperature exceeding 60 °C), wait 30-60 s between cycles.
7. Argonize, close, and parafilm the mixing cup
8. Place the prepolymer-filled mixing cup in a 50 °C oven for 3-5 h
9. Store the prepolymer at 4 °C before use, if needed
    - Cold prepolymer may be tacky, so it often best to heat the prepolymer to room temperature before use.

8.4.5 Making ceramic-PEUR foams
Turkey Red Oil and FeAA catalyst were not used to make ceramic-PEUR foams, but they may be needed to stabilize other ceramic-polymer foams. The pore structure can be visualized by SEM or μCT.

1. Quantify the %NCO of the prepolymer by titration
    - The %NCO can also be estimated by assuming a 50% P-OH conversion
2. Calculate how much of each reagent is needed
    - Recommended batch size = 1 g
    - Index = 115
    - PPHP calcium stearate = 6
    - PPHP water = 0.65
    - PPHP Tegaoamin® 33 = 1.5
    - PPHP Turkey Red Oil = 1.5 (or 0, if it isn't needed)
    - FeAA catalyst = 0.001 g or less (or 0 g, if it isn't needed)
3. Add all the components to a mixing container
    - Add the FeAA catalyst and calcium stearate last
4. Mix at 3500 RPM for 30 s
5. Using a syringe needle, poke a few holes in the bottom of a LDPE sample vial to allow bubbles to escape
6. Using a 1 mL syringe, without the needle, transfer the mixture to the LDPE sample vial
7. Allow the sample to foam and gel overnight at room temperature

8. Using a razor blade, carefully cut the foam from the sample vial
   o If needed, biopsy punches can be used to cut the foam into cylinders

8.4.7 References
1. Guelcher, S. A. *et al.* Synthesis and In Vitro Biocompatibility of Injectable Polyurethane Foam Scaffolds. *Tissue Eng.* **12**, 1247–1259 (2006).
2. Hafeman, A. E. *et al.* Injectable biodegradable polyurethane scaffolds with release of platelet-derived growth factor for tissue repair and regeneration. *Pharm. Res.* **25**, 2387–2399 (2008).
3. Hafeman, A. E. *et al.* Characterization of the degradation mechanisms of lysine-derived aliphatic poly(ester urethane) scaffolds. *Biomaterials* **32**, 419–429 (2011).

8.5   Synthesizing and fractionating Na-polyP glass
8.5.1 Purpose
The purpose of is protocol is to outline how to synthesize and fractionate Na-polyP and how to quantify the average Na-polyP chain length by NMR. The fractionated Na-polyP was used to fabricate Ca-polyP nanoparticles with different chain lengths (**Chapter 7**).

8.5.2 Reagents
- Sodium phosphate monobasic
- Milli-Q water
- Acetone
- D_2O

8.5.3 Materials and equipment
- Furnace that can heat to 700 ºC
- Porcelain crucible
- Copper plate for quenching
- Stainless-steel bin/tray for secondary containment
- Heat resistant gloves
- Crucible tongs
- Face shield
- Beaker or Pyrex bottle and stir bar
- Stir plate
- Pipette controller and serological pipette tips
- 50 mL conical vials
- Centrifuge
- Lyophilizer
- 5 mm NMR tube with cap
- NMR scanner

8.5.4 Making Na-polyP glass using a furnace
While this protocol allowed us to successfully make Na-polyP glass, changing heating parameters, including ramp rate, hold temperature, and duration, may allow you to synthesize and isolate more Na-polyP within a desired range of chain lengths.

1. Add sodium phosphate monobasic to the porcelain crucible
   - Account for some sticking to the crucible when cooling
   - Leave enough space to grab the upper lip of the crucible with the crucible tongs

2. Place the crucible in the furnace
3. Power on the furnace and set the temperature to 700 ℃
4. Allow furnace to heat to 700 ℃
    - We could not control the heating rate of our furnace, but it was approximately 28 ℃ min^{-1}
5. Maintain the furnace temperature for 2 hr
6. While the crucible is still in the furnace, place the copper plate in the stainless-steel bin/tray
7. Wearing heat resistant gloves, open the furnace, gently lift the crucible with the crucible tongs, and pour the Na-polyP from the crucible onto the copper plate
    - Pour as quickly as possible
    - Pour over a large area to keep the Na-polyP glass thin
    - Pour out as much as possible
8. Let the Na-polyP glass cool to room temperature
    - It may crack while it cools
9. Wearing the face shield, break the Na-polyP glass by hand
    - Gently use the copper plate or something else heavy, if needed
    - The Na-polyP will crack/shatter, and it can be difficult to prevent shards from flying out of the stainless-steel bin/tray
    - The Na-polyP pieces should be as small as possible
10. Weigh and transfer the smaller pieces of Na-polyP glass to a beaker or bottle
    - Larger pieces of Na-polyP will stick to the bottom of the beaker or bottle and can interfere with the stir bar
11. Add Milli-Q water to the beaker or bottle and dissolve the Na-polyP overnight using a stir plate
    - If fractioning the Na-polyP, dissolve at 10% wt/v Na-polyP/water or less. A more concentrated Na-polyP solution did not fractionate as well for us, but the impact of Na-polyP wt% on fractionation requires more investigation.
12. Store the dissolved Na-polyP at 4 ℃ until it can be fractionated (**Section 8.5.5**) or until its chain length can be quantified by NMR (**Section 8.5.6**)
    - Na-polyP may not hydrolytically stable, but more investigation is needed to confirm

8.5.5 Fractionating dissolved Na-polyP

Samples only need to be fractioned if you are interested in a specific range of chain lengths. Otherwise, it is recommended the average chain length of the entire Na-polyP batch be quantified by NMR (**Section 8.5.6**).

1. While stirring the dissolved Na-polyP, add acetone until the solution remains cloudy for approximately 15 min.
    - Add 1 mL at a time
    - The solution can become less cloudy during the 15 min mixing period
    - Sometimes, the solution will be cloudy for 15 min, but the denser long-chain Na-polyP layer will be very small after centrifugation. It is unclear why this happens, but, if it does, add more acetone and mix for 15 min.
2. After 15 min, transfer the cloudy solution to 50 mL conical vials
3. Centrifuge at 4200 RPM for 5 min
4. Transfer the less viscous top layer back into the beaker or bottle
    - The top layer will contain the acetone and lower chain length Na-polyP
5. Transfer the more viscous bottom layers to another conical vial or storage bottle
6. Repeat Steps 2-5, as needed
7. Store the remaining fractionated and non-fractionated Na-polyP at 4 ℃ until NMR is complete
8. Freeze dry the Na-polyP fractions needed to make Ca-polyP

- Ca-polyP can likely be fabricated from dissolved Na-polyP, but you may not know the exact mass of Na-polyP

8.5.6 Measuring Na-polyP chain length by NMR

We measured the Na-polyP chain length instead of the Ca-polyP chain length, because we were unable to dissolve the Ca-polyP nanoparticles without damaging the polyP chains. This method also only provides the average chain length. Diffusion-ordered spectroscopy (DOSY) would likely be required to determine chain length distribution properties.

1. Dissolve 100 mg Na-polyP in 550 µL water and 50 µL D_2O, or mix 100 µL viscous fraction, from the acetone fractionation (**Section 8.5.5, Step 7**), with 450 µL water and 50 µL D_2O
   - Dissolving the Na-polyP can take up to 1 h
   - 10 mg Na-polyP may be sufficient, but this requires more investigation
2. Transfer the dissolved/mixed sample into a 5 mm NMR tube
3. Cap the sample and bring it to the NMR scanner
4. Scan the sample using a 500 MHz scanner
   - Other scanners would likely work, but we only used a 500 MHz scanner
   - Select the Phosphorus-31 NMR program or experiment

8.5.7 References

1. Momeni, A. & Filiaggi, M. J. Synthesis and characterization of different chain length sodium polyphosphates. *J. Non. Cryst. Solids* **382**, 11–17 (2013).
2. Smith, S. A. *et al.* Polyphosphate exerts differential effects on blood clotting, depending on polymer size. *Blood* **116**, 4353–4359 (2010).